

FINAL TECHNICAL REPORT

PALEOSEISMIC CONSTRAINTS ON THE RUPTURE HISTORY OF THE SOUTHERN
SAN JACINTO FAULT ZONE, SOUTHERN CALIFORNIA: TOWARDS
UNDERSTANDING PREDICTABLE PATTERNS OF RECURRENCE ON STRIKE-SLIP
FAULTS

U.S.G.S GRANT NO. 06-HQ-GR-0016

Tim Middleton
Thomas Rockwell
Department of Geological Sciences
San Diego State University
San Diego, CA 92182

Abstract

The tectonic geomorphology for the southern 55 km of the Clark strand of the San Jacinto fault zone was studied to determine slip in the past 1-2 events, as well as to map larger offsets for future slip rate determinations. In all, 348 offsets were estimated on channel margins, channel thalwegs, ridge noses, and bar crests using field techniques, aerial photography, and new B4 LiDAR imagery. Displacement estimates show that the most recent event (MRE) produced an average of 2.7 m of slip, ranging from a maximum close to 4 m near Anza, California, to less than one meter near the southeast termination of the fault. However, to the north of Anza, no slip information was collected and five rupture scenarios were developed to make accurate estimates of the potential range of earthquake magnitudes that can account for the observed displacements. Magnitude estimates for these scenarios range between $M_w=7.2$ and $M_w=7.5$. Historically, no earthquake has been recorded along the Clark fault that is large enough to have produced the displacement observed along the southern half of the Clark fault, with the exception of the November 22nd, 1800 event. In that earthquake, the San Diego and San Juan Capistrano missions reported extensive damage (MMI VII): the event was initially placed in the offshore, as there were no constraints from inland areas. However, from paleoseismic work at Hog Lake, the most recent event is dated at ca. 1790, which when considering age uncertainties, could be the November 22nd, 1800 earthquake. By relocating this event on Clark fault, as well as assuming slightly lower intensity values from those interpreted for the missions, magnitude calculations range between $M_w=7.2$ and $M_w=7.5$. These estimates are similar to the calculated magnitudes estimated using the slip distribution and various rupture scenarios. Although a more detailed study is required to the north of Anza to complete the measurements of offset features related to the most recent event, from the information collected for this thesis, it is inferred that the displacement recorded on the southern 55 km is associated with the earthquake of November 22nd, 1800.

TABLE OF CONTENTS

	PAGE
ABSTRACT.....	iv
LIST OF TABLES.....	vii
LIST OF FIGURES	viii
ACKNOWLEDGEMENTS.....	xiii
CHAPTER	
1 INTRODUCTION	1
Historical and Prehistorical Earthquakes on the San Jacinto Fault Zone	6
Paleoseismology	8
2 METHODS	11
3 OBSERVATIONS	17
Anza and Burnt Valley.....	18
BV-8.....	20
BV-5.....	24
Horse Canyon and White Wash.....	24
HC-WW-8.....	26
HC-WW-6, 7.....	30
Dry Wash	34
DW-18.....	34
DW-11.....	39
DW-JAR	39

Jackass Ridge	42
JAR-20	44
JAR-11	44
JAR-5	50
Rockhouse Canyon and Rockhouse Ridge	50
RC-5	53
RR-4	56
Lute Ridge	56
LR-16 and 17	59
LR-13	61
LR-10	61
Late Holocene Multi-Event Offsets	64
DW-JAR	64
Rockhouse Ridge	66
Lute Ridge	69
4 DISCUSSION	71
Rupture Length	72
Size of Earthquake	77
Magnitude Calculations	80
Slip Rate	85
5 CONCLUSION	88
REFERENCES	90

LIST OF TABLES

	PAGE
Table 1. Anza-Burnt Valley Displacement Data (BV)	21
Table 2. Horse Canyon and White Wash Displacement Data (HC-WW)	28
Table 3. (a) Dry Wash Displacement Data (DW). (b) Dry Wash-Jackass Ridge Displacement Data (DW-JAR)	36
Table 4. Jackass Ridge Displacement Data (JAR).....	45
Table 5. (a) Rockhouse Canyon (RC). (b) Rockhouse Ridge (RR).....	54
Table 6. Lute Ridge Displacement Data (LR)	60
Table 7. Possible Rupture Patterns and Associated Earthquake Magnitudes	79
Table 8. Estimated Slip Rate Based on Displaced Alluvial Fan Apex of Lute Ridge	87

LIST OF FIGURES

	PAGE
Figure 1. Location of the San Jacinto fault relative to the southern San Andreas fault system highlighting earthquakes ($M \geq 6$) since 1890. Historic surface ruptures delineated in bold.....	2
Figure 2. Reconstruction of the Thomas Mountain Sill in the north and a distinctive post-batholithic zone of cataclastic deformation in the south requires ~24 km of overall slip on the Clark, Coyote Creek, and Thomas Mountain strands of the San Jacinto fault system along with 15 km on the Clark fault, 8 km on the Coyote Creek fault, and ~1 km on the Thomas Mt. fault.	3
Figure 3. Isoseismal maps for (a) the earthquake of December 25 th , 1899 and (b) the earthquake of April 21 st , 1918.	7
Figure 4. Interpreted photo mosaic of the exposure of the San Jacinto fault at Hog Lake. Units 19 and 11 are outlined in green and the San Jacinto fault depicted in red. Note the mismatch in stratigraphy between unit 19 and 11 that occurred from the MRE only. Unit 19 appears to have a right-side down component of slip while Unit 11 appears to be right-side up. This is consistent with substantial displacement from a large strike-slip event for the MRE, dated here at Hog Lake as ca 1790.....	9
Figure 5. Detailed geologic map of the southern Clark fault. The focus area is separated into six sections bounded by structural complexities or young alluvium where offsets are not preserved. Within these six sections I estimated displacement on channel margins, thalwegs, and ridge nose.	12
Figure 6. Overview map showing the location of B4 LiDAR flight lines from 2005. Flight line SJF_04 was used for analysis in this project.	15
Figure 7. Slip distribution graph for the MRE (lower cluster, blue line) and past two events (upper cluster, pink line) from the Anza Valley south to the termination of the Clark fault near Lute Ridge. Data points represent the most reliable and best preserved features to estimate displacement.	19
Figure 8. Annotated LiDAR DEM of the Anza and Burnt Valley section. Graphs display estimated displacement from field work and high resolution LiDAR DEM's. Blue lines connect estimates of displacement in the MRE while the orange circle is inferred as offset from the past two events.....	22

- Figure 9. Annotated topographic map and photograph of BV-8 (UTM Zone 11, 533730 N, 3714456 E) in Anza Valley. The measured field and LiDAR displacements are shown in the table for the channel margins and thalweg. Channel thalwegs are shown as blue lines, channel margins are green lines, and the fault trace is the red line. The numbers on the channel cross-sections represent distances along the profile line, referenced parallel to the fault. All locality figures are annotated similarly from here on.23
- Figure 10. Topographic map and interpreted photograph of BV-5 (UTM zone 11, 536499 E, 3712504 N) near Burnt Valley. Measured displacements from field work and LiDAR DEM's are presented in the table.....25
- Figure 11. Annotated LiDAR DEM of the Horse Canyon-White Wash (HC-WW) section with localities where offsets were estimated. Letters denote where displacement was measured by LiDAR only. Displacements estimated in the field and from LiDAR DEM's are presented in table 2 and shown here. Blue lines connect displacements inferred to be from the MRE. Orange lines roughly connect slip accrued during the past two events.27
- Figure 12. Annotated topographic map and cross-section lines of HC-WW-8 (UTM zone 11, 543279 E, 3706681 N) generated from the LiDAR DEM's. Offset estimates assessed from field work and by LiDAR DEM's are presented in the table.....31
- Figure 13. Interpreted photograph and topographic map of HC-WW-7 (UTM zone 11, 543388 E, 3706531 N). Displacements of the southeast margin and thalweg, both near- and far-field, were measured from LiDAR DEM's and through field observations and showed in the table.32
- Figure 14. Topographic map and cross-section lines of HC-WW-6 (UTM zone 11, 543394 E, 3706519 N) generated by the LiDAR data set. Offsets of both channel margins and the thalweg as measured in the field and by LiDAR DEM's are presented in the table.....33
- Figure 15. Annotated aerial photograph of Dry Wash (DW) section showing measured localities. Slip distribution graphs are presented for displacements measured from field and the LiDAR data. Letters denote where only LiDAR measurements are available. Blue, orange, and purple represent single, double and triple events, respectively.....35
- Figure 16. LiDAR generated topographic map and cross-section profile as well as annotated field photograph of DW-18 (UTM zone 11, 549104 E, 3702763 N). Displacement measured in the field and by LiDAR DEM's of the northwest margin and thalweg, near- and far-field, are shown in the table.....38

Figure 17. Map and interpreted field photograph of offset channel DW-11 (UTM zone 11, 550367 E, 3701892 N) on the west side of Dry Wash. Offset estimated by LiDAR and in the field for both channel margins and the thalweg are presented in the table.....40

Figure 18. Annotated LiDAR DEM of DW-JAR where Dry Wash crosses the fault just north of Jackass Ridge (UTM zone 11, 552123 E, 3700715 N). Displacements assessed in the field and by LiDAR DEM's on five rills and bars, which are displayed in the table. A detailed reconstruction of site five can be seen in Figure 30.....41

Figure 19. Annotated aerial photograph of Jackass Ridge (JAR) with the locations of displaced features shown. Letter labeled sites are where displacements were estimated from the LiDAR DEM's only. Slip distribution graphs are presented for estimates made in the field and by LiDAR/Aerial photographs. Blue and orange lines connect offsets that occurred from the MRE and past two events, respectively.43

Figure 20. Annotated topographic map and field photograph of offset channel JAR-20 (UTM zone 11, 552798 E, 3700271 N) along Jackass Ridge. Displacements of the channel margins and thalweg were estimated in the field and from LiDAR DEM's. The measurements are shown in the table.....48

Figure 21. Interpreted field photograph and LiDAR generated topographic map and cross-sections for offset channel JAR-11 (UTM zone 11, 553133 E, 3700059 N) along Jackass Ridge. The table displays displacements for the three channel features estimated from field observations, LiDAR DEM's and aerial photography.49

Figure 22. Topographic map, channel cross-sections, and interpreted field photograph of offset rill JAR-5 (UTM zone 11, 553375 E, 3699925 N) along Jackass Ridge. Offsets of the southeast margin and thalweg were estimated in the field and subsequently with the LiDAR data and aerial photography. The results are presented in the table.51

Figure 23. LiDAR DEM and slip distribution graphs for Rockhouse Canyon (RC) and Rockhouse Ridge (RR) with offset localities denoted on the DEM's. As before, estimates connected by blue lines are inferred to be slip in the MRE while orange connect slip accrued from the past two events.....52

Figure 24. LiDAR generated topographic map and channel cross-section, as well as annotated field photography of offset drainage RH-5 (UTM zone 11, 557954 E, 3697119 N) in Rockhouse Canyon. As before, cross-section lines were taken parallel to the fault trace. Displacements of the thalweg, in the near- and far-field, and the southeast margin are shown in the table.....55

- Figure 25. Topographic map and channel cross-section generated from the LiDAR DEM's of offset rill RR-4 (UTM zone 11, 559754 E, 3696113 N) along Rockhouse Ridge. Displacement was estimated from the LiDAR DEM's and in the field for the thalweg only and displayed in the table.....57
- Figure 26. Annotated LiDAR DEM of Lute Ridge (LR) with offset channel sites. Slip distribution graphs are presented for offsets estimated from the LiDAR data and in the field. Blue and orange lines connect displacement estimates from the MRE and past two events, respectively.58
- Figure 27. Interpreted field photograph and topographic map of offset rills LR-16 and LR-17 (UTM zone 11, 573905 E, 3686536 N). LR-16 expresses roughly half the displacement of LR-17, suggesting that the smaller rill, LR-16, was only displaced in the most recent event, whereas the larger rill, LR-17, was displaced during the past two events. Displacements of both rills are shown in the table.....62
- Figure 28. LiDAR topographic map and channel cross-sections of a displaced rill at LR-13 (UTM zone 11, 574258 E, 3686332 N). The southeast margin and thalweg are displaced similarly and interpreted to be the result of the MRE.....63
- Figure 30. Detailed topographic map of displaced bars and swales where dry wash crosses the trace of the Clark fault (UTM zone 11, 552086 E, 3700723 N). Lines represent bar crests on either side of the fault with north to the top left of the figures. (a) Present day; (b) A 17 m reconstruction realigns the southern bar on the southwest side of the fault with the bar crest on the northern side, as well as the ridge nose to the north; (c) A 28 m reconstruction realigns the northern bar crest on the southwest side with the bar crest on the north side of the fault. This reconstruction causes the ridge nose to protrude into the channel.....65
- Figure 31. Interpreted oblique LiDAR DEM of south Rockhouse Canyon and north Rockhouse Ridge. Beheaded channels (1 and 2) are laterally displaced about 540 m and 150 m, respectively, from the active channel (I). Offsets were estimated based on reconstructions to the source location assuming some bending and warping has occurred since beheading (Figures 32a and b).....67
- Figure 32. Large scale reconstruction of Rockhouse Ridge. (a) 1 km reconstruction that realigns source drainages II, III, and IV with offset drainages 1, 2, and 4, respectively. Some source drainages (II and III) appear fairly young and this reconstruction may not be correct. (b) 540 km reconstruction realigning source drainages I, II, II, and IV with offset drainages 1, 3, 4, and 6. This reconstruction seems more reasonable since the initiation of the drainages; however, more work is needed to resolve the exact reconstruction.68

- Figure 33. Interpreted topographic map of Lute Ridge in Clark Valley. The projection of the fan apex can be reconstructed too three prominent source drainages (A, B, and C). The farthest reconstruction (C), although not out of the question, is the most unlikely. A more likely scenario realigns the offset fan of Lute Ridge to both drainage A and B requiring between 400 to 980 m of displacement.70
- Figure 34. (a) Slip distribution graph for the Imperial Valley earthquakes of 1940 and 1979. The earthquake of 1979 ruptured only the northern 30 km with similar displacement to the earthquake of 1940. (b) Proposed ‘patch’ model for the Imperial Valley fault where slip accumulates from smaller earthquakes to equal the amount of displacement caused by one event in an adjacent stronger part of the fault (Sieh, 1996).74
- Figure 35. Surface rupture scenarios for the Clark fault. (a) Surface rupture only extends to the northern extent of the Anza gap. (b) Surface rupture extends the entire length of the Clark and Casa Loma fault, but with offsets about a meter for the northern 40 km of the Clark fault. (c) Surface rupture propagates through the Hemet step-over breaking the Claremont, Casa Loma, and Clark fault. (d) Similar to scenario C, surface rupture extends the entire Casa Loma and Clark fault, however slip distribution is symmetrical with maximum slip occurring in the Anza gap. E.) Surface rupture only extends for the 55 km of the Clark fault in which I have recorded slip for the MRE. This is used as an absolute minimum.76
- Figure 36. Isoseismal maps of (a) the earthquake of February 9th, 1890 and (b) the earthquake of May 28th, 1892. Both earthquakes are assessed to be $M_w=6.3$ or less..82
- Figure 37. Isoseismal maps of the November 22nd, 1800 earthquake interpreted from two observations at San Diego and San Juan Capistrano missions. (a) First estimates suggest MMI VII damage at both missions. If the epicenter is placed on the Clark fault this would result in a $M_w=7.8$. (b) Reinterpreting the intensity damage for the missions I suggest a lesser MMI value for the missions. Placing them in the MMI VI range rather than VII I estimate $M_w=7.2$ to $M_w=7.6$, consistent with estimates assessed from the slip distribution.84

CHAPTER 1

INTRODUCTION

The San Jacinto fault zone is one of the major branches of the San Andreas fault system in southern California, extending from a complex zone of strike-slip faults northwest of San Bernardino southeastward into the Salton Trough (Figure 1; Sharp, 1967; Matti et al., 1992; Morton and Matti, 1993). A likely continuation of the fault extends the zone southward across the international border and probably connects with the Cerro Prieto fault in northern Baja California (Magistrale, 2002). Altogether, the San Jacinto zone is as much as 350 km in length, although the fault is clearly separable into several segments, the longest of which is the Clark-Casa Loma fault zone that extends from near Hemet southeastward 120 km to the San Felipe Hills.

The San Andreas and San Jacinto fault zones accommodate the majority of the 49-50 mm/yr of relative motion between the Pacific-North American plate boundary, as estimated by NUVEL-1A and GPS data (DeMets, 1995; Bennett et al., 1996; Fialko, 2006). Sharp (1967) has inferred at least 21-26 km of total slip on the San Jacinto fault system since about 1.0-2.5 Ma (Morton and Matti, 1993) based on distinctive post batholithic zones of cataclastic deformation near Clark and Borrego valleys (Figure 2). In this area, however, the slip is partitioned between the two major strands, the Clark and Coyote Creek faults, with about 15 km and 8 km of slip on each, respectively. Near Anza where slip is localized in a narrow zone, Sharp (1967) mapped a distinctive body of foliated biotite adamellite with a core of olivine hornblende norite and gabbro that he named the Thomas Mountain Sill.

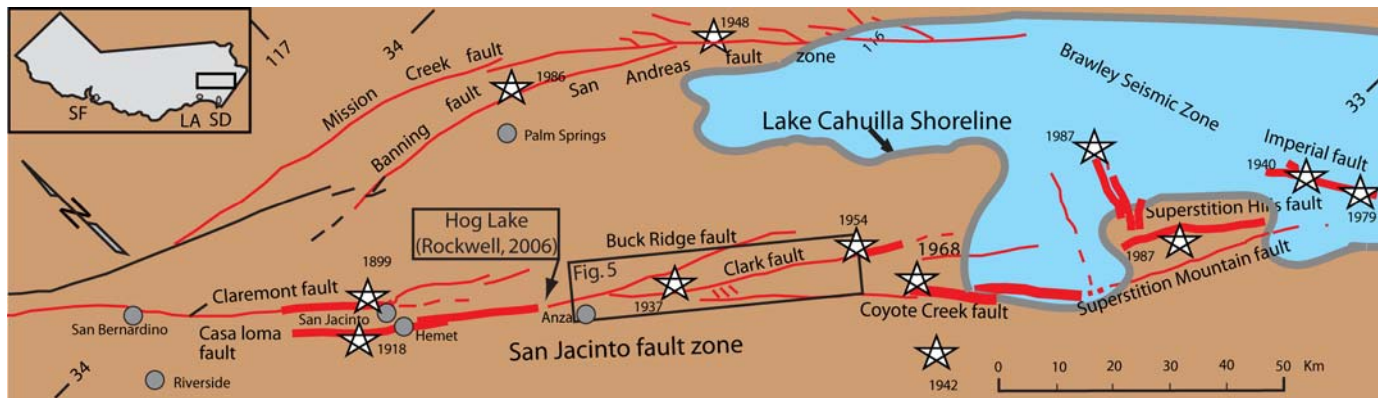


Figure 1. Location of the San Jacinto fault relative to the southern San Andreas fault system highlighting earthquakes ($M \geq 6$) since 1890. Historic surface ruptures delineated in bold.

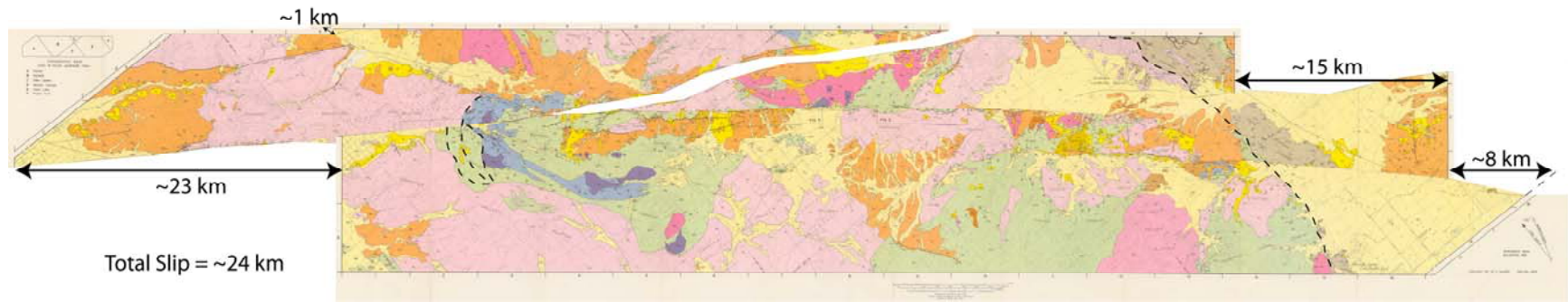


Figure 2. Reconstruction of the Thomas Mountain Sill in the north and a distinctive post-batholithic zone of cataclastic deformation in the south requires ~24 km of overall slip on the Clark, Coyote Creek, and Thomas Mountain strands of the San Jacinto fault system along with 15 km on the Clark fault, 8 km on the Coyote Creek fault, and ~1 km on the Thomas Mt. fault. (Modified from Sharp, 1967)

This rock body is present across all elements of the fault zone, and reconstruction of it suggests a similar total displacement of about 24 km, of which most (23 km) is accommodated by the Clark fault (Figure 2). Minor drag of the bedrock units used as piercing lines, along with uncertainties as to the exact location of key contacts due to burial by alluvium, allows for no more than another 1-2 km of possible slip, placing the maximum total slip on the central and southern San Jacinto fault zone at about 26 km. In contrast, the San Andreas has about 310 km of post late Miocene slip (Powell, 1993) and has acted as the primary plate boundary for most of the Pliocene and Quaternary.

There is substantial uncertainty regarding the slip rate of the San Jacinto fault, with reported rates ranging from 6 to 30 mm/yr. Much of the uncertainty on these estimates is a function of the methods utilized to resolve the slip rate as well as the location of slip along the fault. Hanks et al. (1975) used the sum of seismic moments from historical earthquakes larger than magnitude six ($M6$) along the entire San Jacinto fault system to estimate a slip rate of about 10 mm/yr. Estimates from geodetically-measured strain accumulation across the fault zone range from 9 ± 2 mm/yr to 17 ± 5 mm/yr; however, the higher rate likely includes some strain accumulation from the San Andreas fault (Bennett et al., 1996; Savage et al., 1981).

Through geologic mapping of a monolithic alluvial fan near Anza, California, Sharp (1981) measured a minimum of 5.7-8.6 km of dextral offset between the fan and the location of its original source. The offset alluvial fan overlies a series of lacustrine deposits that contain the 730 ka Bishop Tuff and provides a minimum slip rate of 8-12 mm/yr from the middle Pleistocene to the present. Rockwell et al. (1990) also estimated the slip rate near Anza to be 7-19 mm/yr, based on displacement of several offset channels incised into alluvial

fans that were dated using ^{14}C data and soil chronology. Similarly, Merrifield et al. (1991) studied offset incised channels combined with ^{14}C data near Anza to propose a minimum Holocene slip rate of about 12 mm/yr. To the north, in the San Timoteo Badlands, based on geologic and stratigraphic relationships, Kendrick et al. (2002) inferred a slip rate of greater than 20 mm/yr with an upper boundary of 30 mm/yr, while Morton and Matti (1993) suggest a slightly lower rate of 17 mm/yr with an upper limit of 23 mm/yr.

The timing of slip initiation on the San Jacinto fault is somewhat controversial, although it is clear that the San Jacinto fault is younger than the San Andreas fault. If a total offset of 24 km is assumed, as estimated by Sharp (1967) and as shown in Figure 2, and combine that with an inferred slip rate of about 10 mm/yr, the estimated age of initiation for the San Jacinto fault is about 2.4 Ma. However, Morton and Matti (1993) suggest the inception to be much younger, between ca. 1.0 and 1.5 Ma based on geological and stratigraphic relationships near San Bernardino to the north. This, in turn, implies a higher slip rate of between ~16 and 24 mm/yr (Dorsey, 2002). In the San Felipe Hills, south of the mapped termination of the Clark fault (Sharp, 1967), Janecke et al. (2004) infer a similar age for the major change in fault geometry at ~ 1.1 Ma. This assumption is based on an angular unconformity between the Ocotillo Formation and its finer grained equivalent, the Brawley Formation, and the bedrock-cored San Felipe anticline. Janecke et al. (2004) interpret the San Felipe anticline to be a wrench fold within the ancestral San Jacinto fault zone, and the unconformity at ~1.1 Ma to be either the initiation of, or the major reorganization of the fault zone.

Regardless, the total amount of slip over the past 1-2.4 Ma requires that the San

Jacinto fault accommodate 20-50 % of the total Pacific-North American plate motion for this period.

HISTORICAL AND PREHISTORICAL EARTHQUAKES ON THE SAN JACINTO FAULT ZONE

Historically, the San Jacinto fault zone is the most seismically active fault in southern California, with at least 10 earthquakes greater than $M6$ along its length since 1890 (Sanders and Kanamori, 1984). As many as four of the ten large earthquakes (1899, 1918, 1937, and 1954) are believed to have occurred on the Clark strand of the San Jacinto fault zone, although the 1937 ($M5.9$) event was probably actually on a cross-fault between the Clark and Coyote Creek faults (Doser, 1990). Two more early earthquakes (1890 and 1892) are also potentially placed on the Clark fault by Topozada et al. (1981), but these are so poorly located that they could have been anywhere in the southern San Andreas fault system (observations of their occurrence are only reported at distant localities such as Yuma, Los Angeles, and San Diego).

Two seismic events (1899, 1918) are inferred to have occurred along the northern Clark-Casa Loma fault near Hemet. The 1899 “Christmas Day” earthquake produced a relatively circular isoseismic pattern, indicating a relatively small source dimension (Figure 3a; Topozada et al., 1981) whereas the 1918 event produced a slightly elongated pattern of damage and felt effects (Figure 3b). Although both events were potentially large enough to have produced ground rupture, and both did produce “cracking”, neither event is known to have ruptured to the surface. For both events, early geologists visited Hog Lake and documented the absence of surface rupture there (Claypole, 1900; Townley, 1918), which is important for interpretation of the paleoseismic record at that location. Of the other

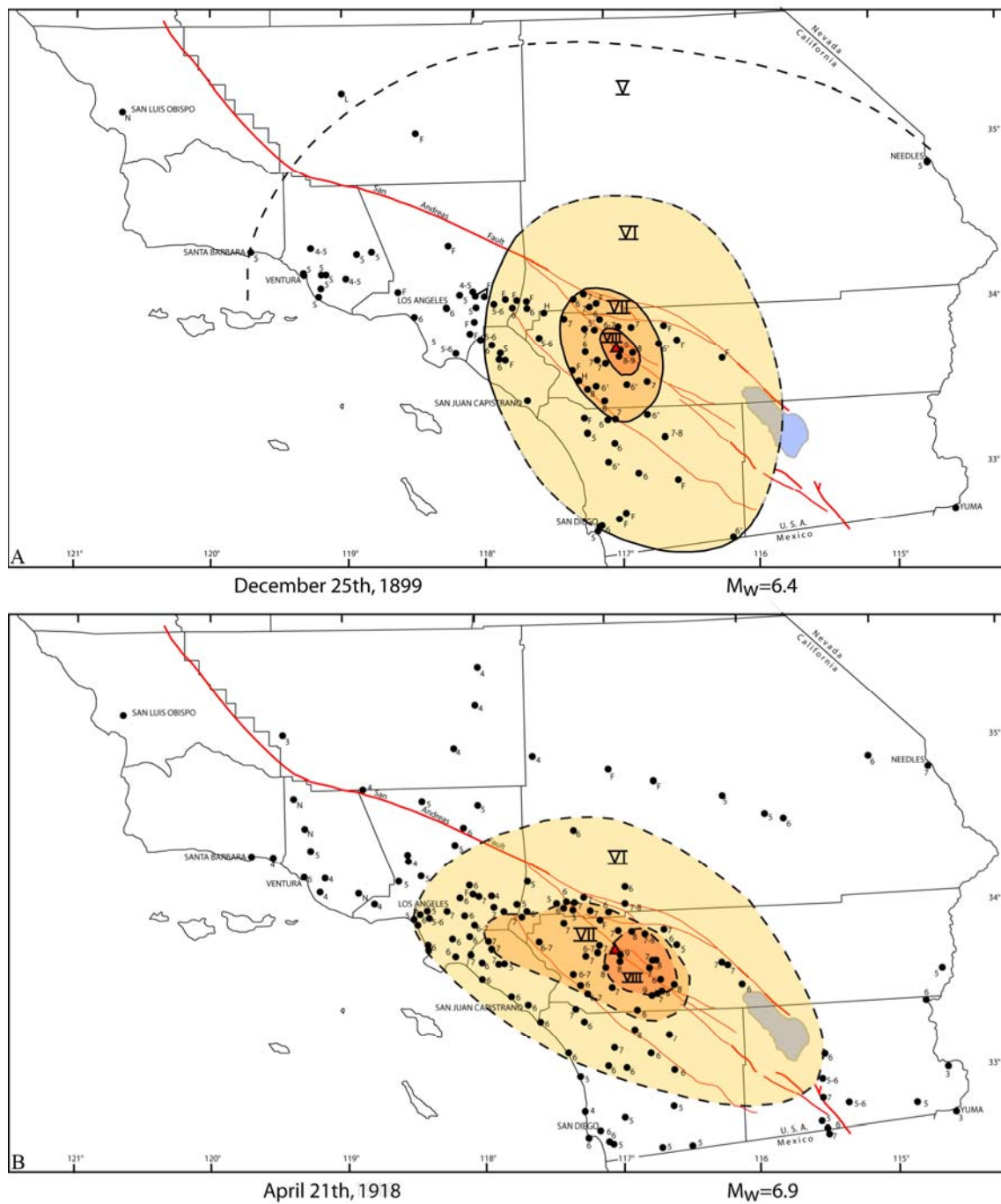


Figure 3. Isoseismal maps for (a) the earthquake of December 25th, 1899 and (b) the earthquake of April 21st, 1918. Modified from Toppozada et al. (1981).

two events that occurred along or near the southern Clark fault, only the 1954 (M6.2) event is likely on the main strand of the Clark fault (Sanders et al., 1986; Doser, 1990). Neither of these events apparently produced surface rupture, which is not surprising considering their relatively small sizes.

A 20-km section of fault, defined by little to no seismic activity, has been deemed the Anza seismicity gap by Sanders and Kanamori (1984). This seismicity gap lies between the known historical earthquakes (1899 and 1918 to the north, and 1937 and 1954 to the south), and no earthquake since at least 1890 has apparently ruptured within this gap. In fact, there are no historical earthquakes, with the exception of a large but poorly located earthquake in November, 1800, that could be attributed to the rupture within the Anza seismicity gap nor along most of the southern Clark fault.

PALEOSEISMOLOGY

Recent paleoseismic work at Hog Lake, 5 km north of Anza, has documented 16 surface ruptures on the central Clark fault over the past ~ 4 ka, with the most recent event (MRE) at ca. 1790 (Rockwell et al., 2006). These observations suggest a recurrence interval of about 250 years for large, surface rupturing events at Hog Lake. However, there is no well-constrained information on slip per event for any of the prehistorical events, although the most recent event is inferred to have been large due to a mismatch in stratigraphy (Figure 4). Nevertheless, the observed average recurrence interval combined with the available slip rate information suggests reasonably large events with 2.5-3.5 m per event. This amount of displacement, in turn, suggests that at least some of the earthquakes were in the magnitude 7 range, or greater.

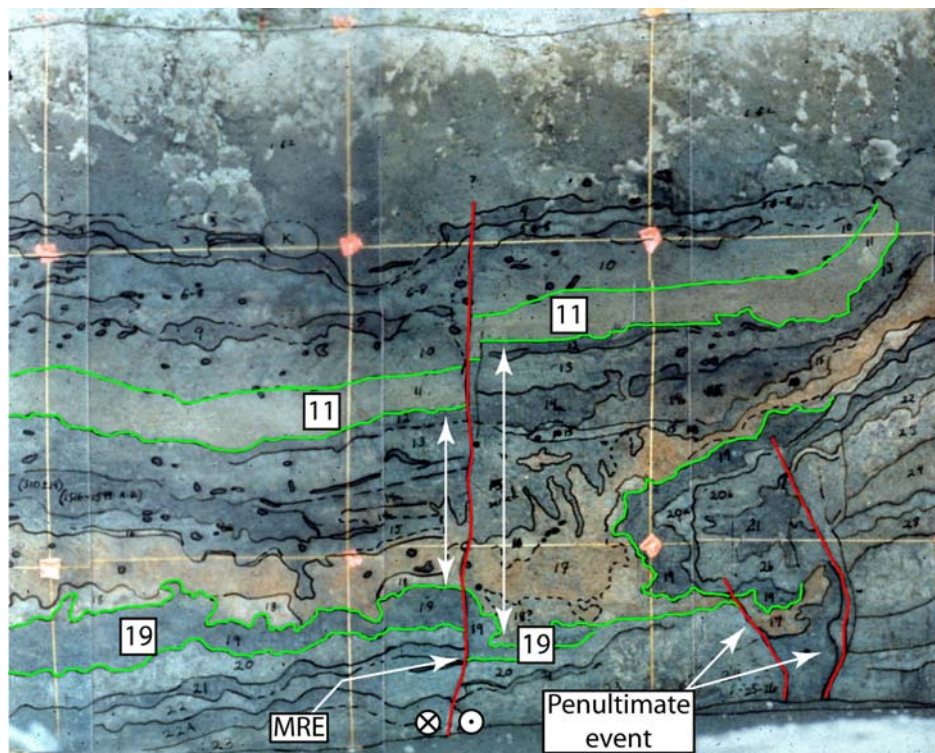


Figure 4. Interpreted photo mosaic of the exposure of the San Jacinto fault at Hog Lake. Units 19 and 11 are outlined in green and the San Jacinto fault depicted in red. Note the mismatch in stratigraphy between unit 19 and 11 that occurred from the MRE only. Unit 19 appears to have a right-side down component of slip while Unit 11 appears to be right-side up. This is consistent with substantial displacement from a large strike-slip event for the MRE, dated here at Hog Lake as ca 1790 (Rockwell et al. 2006).

Dating of the most recent event at Hog Lake potentially places this large earthquake in the historical period. Although not well documented, a relatively large earthquake did occur on November 22, 1800 which resulted in cracked adobe walls (Modified Mercalli Intensity (MMI) VII) at the San Diego and San Juan Capistrano missions. Topozada et al. (1981), estimates this earthquake to be greater than magnitude 6.5 due to the intensity of damage at both missions, located more than 90 km apart. Traditionally this event has been located on one of the several offshore borderland faults, although there are virtually no constraints for its location. However, considering the apparent similarity in age to the most recent event at Hog Lake, it is also plausible to relocate this event inland, placing it on the Clark strand of the San Jacinto fault. If this is the case, then there should still be abundant offsets of small drainages (rills) and other features preserved in the landscape.

Up to now, there has been little information collected on slip in the previous event along the Clark fault. The central focus of this thesis is to map offset rills, channel bars, and other geomorphic features from Anza to the southeast end of fault with the intent of resolving the slip distribution for the most recent event recognized at Hog Lake (Figure 5). I employed field techniques, aerial photographs, and new LiDAR data (B4) to assist in this task. From the slip distribution, I will be able to estimate the seismic moment and magnitude of the most recent event, a critical element in assessing the potential damage from future large seismicity along this major fault.

CHAPTER 2

METHODS

Previous studies by several authors have used geomorphic offsets to determine slip associated with historic and pre-historic earthquakes (Sieh, 1978; Rockwell and Pinault, 1986; Lindvall et al., 1989; McGill and Sieh, 1991; McGill and Rubin, 1999). This study focuses on offset rills, channels, depositional bars and other geomorphic features along much of the 55 km section of the San Jacinto fault between Clark Valley and Anza Valley, with locations for slip measurements determined from mapping on aerial photography and by comparisons to previous mapping efforts in the area (Sharp, 1967; 1972). The 55 km section of the Clark fault that was investigated was split into six different sections where dextral offsets were found to be numerous, separated by structural complexities or areas of very young alluvium (Figure 5).

Slip measurements and their associated uncertainties were estimated in the field using a metric steel tape measure. Offset was determined by matching similar features such as channel margins and thalwegs that intersected and were nearly perpendicular to the fault. On channel features that were deflected or lacking distinctive piercing points, features were projected into the fault zone and measured slip along strike of the fault. Error estimates were based upon two different factors; the overall shape of the measured feature and the overall size (coarseness) of alluvium in the channels. If the channel margins were found to be degraded, were hard to locate, or were very broad, the resulting uncertainty would be relatively large. Similarly, some channels and channel margins contained large boulders, in

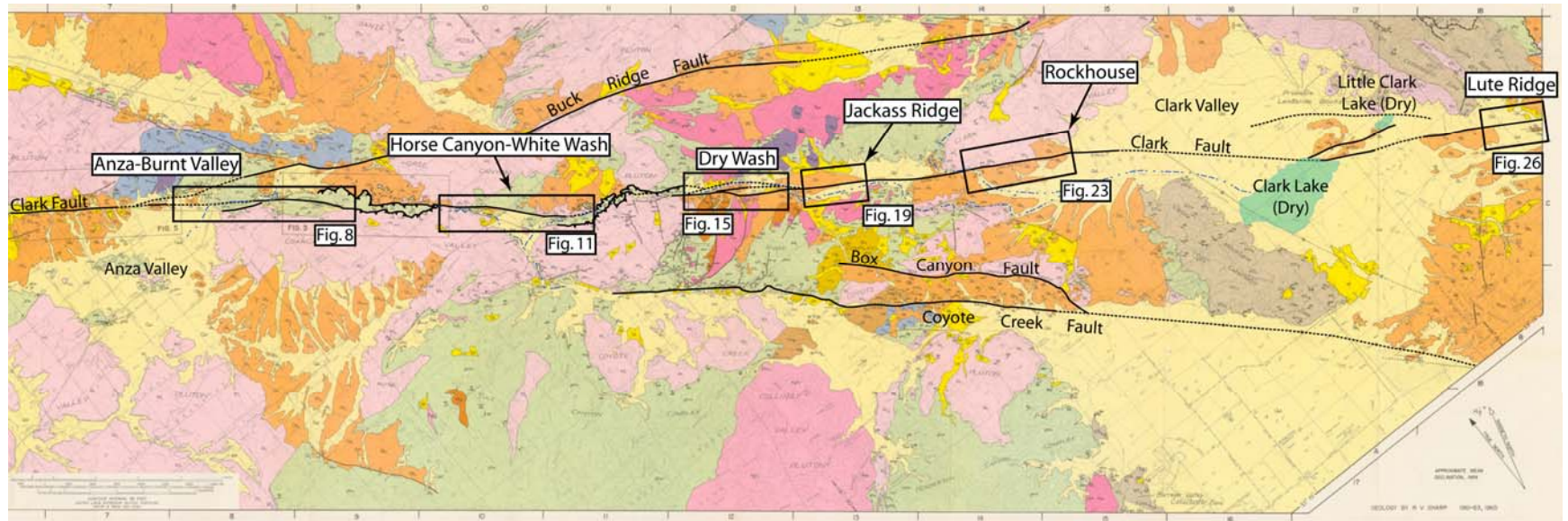


Figure 5. Detailed geologic map of the southern Clark fault (Sharp, 1967). The focus area is separated into six sections bounded by structural complexities or young alluvium where offsets are not preserved. Within these six sections I estimated displacement on channel margins, thalwegs, and ridge nose.

excess of a meter, resulting in uncertainty as to the precise location of the thalweg or actual channel margins, and our estimate of the errors in these cases reflect our uncertainty in locating the displaced features.

The quality of the measurements was estimated in the field and from the LiDAR data based on the confidence of channel features and associated slip measurements. For an excellent quality offset, more than one feature was preserved resulting in multiple measurements, and channel margins were unmistakable in the field. On the other hand, poor quality measurements have hard to distinguish channel features, due either to large boulders or degradation of the channel margins. In the field, I assigned quality estimates that ranged from 1 through 10 for each measured offset based on the sharpness of the channel features and ease of projection of the feature into and across the fault zone. Sieh (1978) uses a quality system of excellent, good, fair, and poor in which I have modified our field numbers into (9-10 = Excellent, 7-8.75= Good, 5.25-6.75= Fair, and 0-5 = Poor).

For the San Diego County part of the field area, I also made estimates of slip from enlarged color aerial photography (1:12,000 original scale). The scale of various portions of the photos was determined from comparison and scaling to topographic maps, and a scale was embedded in the photos prior to their enlargement. For some areas with abundant offset rills, the stereo-pair photos were enlarged by about 700%, which allowed for measurement of displaced features down to the sub-meter size. For these measurements, the scale could be read to better than a half meter, so a 0.5 m error was assessed for all such measurements. After two-thirds of the field work was completed, I received Light Detection And Ranging (LiDAR) data to assist with inferring slip measurements. The LiDAR data were acquired and processed in 50 km increments along the southern San Andreas and San Jacinto fault

systems by the National Center for Airborne Laser Mapping (NCALM) in May 2005 (Figure 6). Kinematics and Rapid Static (KARS) and GPS processing were completed at NCALM and Ohio State, and the resulting data were distributed as 0.5 m resolution DEM's along with the raw point clouds in x, y, z ASCII file format, which consists of UTM coordinates and elevation points. For my study, I utilized the 4th San Jacinto flight line, which traverses from just south of Hog Lake near Anza to the southern tip of the Santa Rosa Mountains near Clark Valley. I reprocessed the raw point clouds into higher resolution DEM's with a sampling size of 0.25 m (compared to off-the-shelf 0.5 m resolution).

Once surface maps were created, QT Modeler was used to make measurements, generate contours, and construct cross-section profiles of the offset geomorphic features. Profiles were taken as close as possible and parallel to the fault to resolve true slip. Two methods assisted in determining slip, the first uses the measurement tool built into the program. This method allows the user to select two points and measure the distance between them. The second method allows the user to create topographic profiles parallel to and on either side of the fault. From these profiles, the channel thalweg and margins are easily decipherable and measurement of these features provided highly accurate estimates of displacement.

Uncertainties arise independently from using each of the methods. The first method chooses points along the surface rather than in free space. As a result, elevation becomes a factor when making slip measurements. For example, an offset channel margin can project into the thalweg on the other side of the fault. Depending on the size of the margin, measurement from the projection can result in over a meter of elevation change, thus skewing the true value. To overcome this problem, multiple measurements (up to 10) are

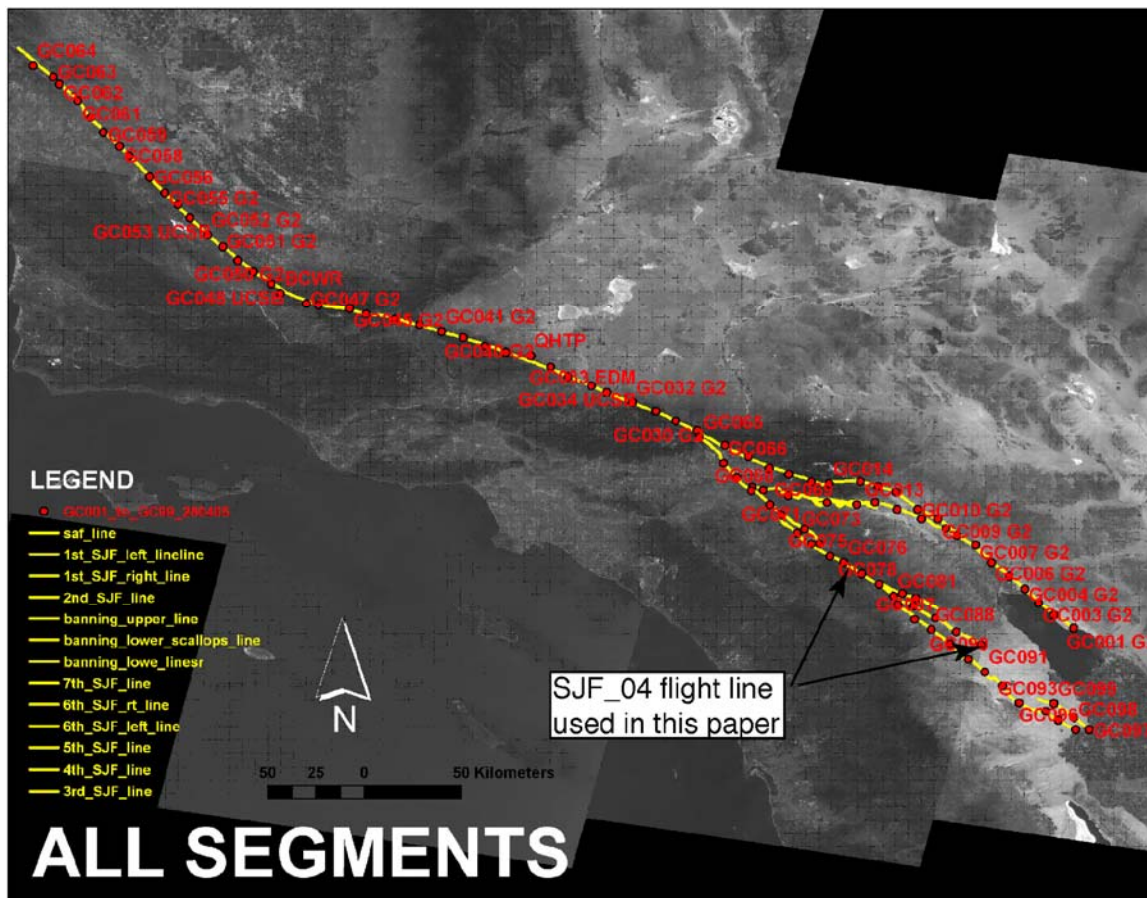


Figure 6. Overview map showing the location of B4 LiDAR flight lines from 2005. Flight line SJF_04 was used for analysis in this project.

made of each individual feature with the average value reported. Errors are determined using the largest variance from the mean (i.e. the average slip value = 2.5, with the largest value reported at 3.1 m, so the uncertainty is 0.6 m).

The second method also can provide large uncertainties when used independently. If the desired feature trends in any direction other than perpendicular to the fault, measurements can result with as much uncertainty as a few meters. To correct for this uncertainty, profile lines are placed as close to the fault trace as possible so the overall trend of the feature does not factor into the measurement value. In some cases, the fault trace is spread out over a zone of shearing up to a few meters in width, resulting in a smaller slip estimate than if the overall deflection is taken into consideration. Independently, both methods offer their own estimates of uncertainty. However, when each estimate is similar, my confidence in the measurement increases.

CHAPTER 3

OBSERVATIONS

Throughout the focus area, the major strand of the Clark fault is generally mapped as a single linear trace with several small *en echelon* splays and two large restraining bends, one between Dry Wash and White Wash and another between White Wash and Burnt-Anza Valley (Figure 5; Sharp, 1967). As the Clark fault enters Clark Valley from the northwest, the strike gradually changes from southeast to east-southeast, causing dip-slip motion and thereby creating the depression for Clark Lake. Although there are several strands mapped within the focus areas (Sharp, 1967; 1972), I was able to locate the active strand in which the majority, if not all, of the recent slip has occurred.

Three hundred and forty-eight individual measurements were made from field investigations, aerial photography, and the new LiDAR data set for the 55 km stretch of the Clark fault from the southeastern termination of the fault in the San Felipe Hills northward to the town of Anza. Vegetation, and consequently precipitation, varies along strike from the densely vegetated Anza Valley near an elevation of 1200 m southward to the sparsely vegetated desert environment, at elevations of about 200-300 m. Annual precipitation for the Anza Valley is about 60 cm which generally falls during the winter months from Pacific storms. The dense vegetation disperses the rainfall energy allowing for the creation of long-lived channels. In the lower elevations, precipitation occurs during the summer from desert thunderstorms in which running water typically occupies the channels during or immediately following rainfall. Occasionally the heavy precipitation from the thunderstorms can form

new rills as the infiltration threshold is breached. However, due to the highly localized nature of the thunderstorms, the fault scarps created in the rills can be preserved for hundreds of years.

In this study, I used primarily the channel margins, thalwegs, and ridge noses to resolve displacement on individual features, and to compile the slip distribution along the Clark fault. I was able to divide the 348 slip estimates into the following three different categories or data clusters: slip during the MRE (cluster 1), double-event offsets (cluster 2), and multi-event offsets (cluster 3) which range anywhere from three-event offsets to cumulative slip since the mid-Holocene. Two hundred and fifty-one of the estimates cluster around ~2.7 m of slip (cluster 1), which is attributed to the average slip displacement in the MRE. Individual slip measurements for the MRE generally decrease to the south, averaging about 3.3 m in the Anza-Burnt Valley section and dwindling to less than a meter near the mapped termination of the fault (Figure 7; Sharp (1967)). The second cluster has offsets that exhibit nearly double the slip that was estimated for the MRE, averaging ~4.9 m for the entire focus area. As with the MRE, slip appears to decrease from NW to SE (Figure 7).

For this section, I discuss the offset measurements by area, starting from the northwest. I also discuss the structural complexities that separate the various study sections, as they relate to the interpretations. For each section, I present the best-preserved offsets, with detailed annotated photographs and LiDAR-generated DEM's.

ANZA AND BURNT VALLEY

The Anza and Burnt Valley section represents the farthest north area that was investigated, with an average elevation of 1200 m and about 60 cm of annual rainfall. The

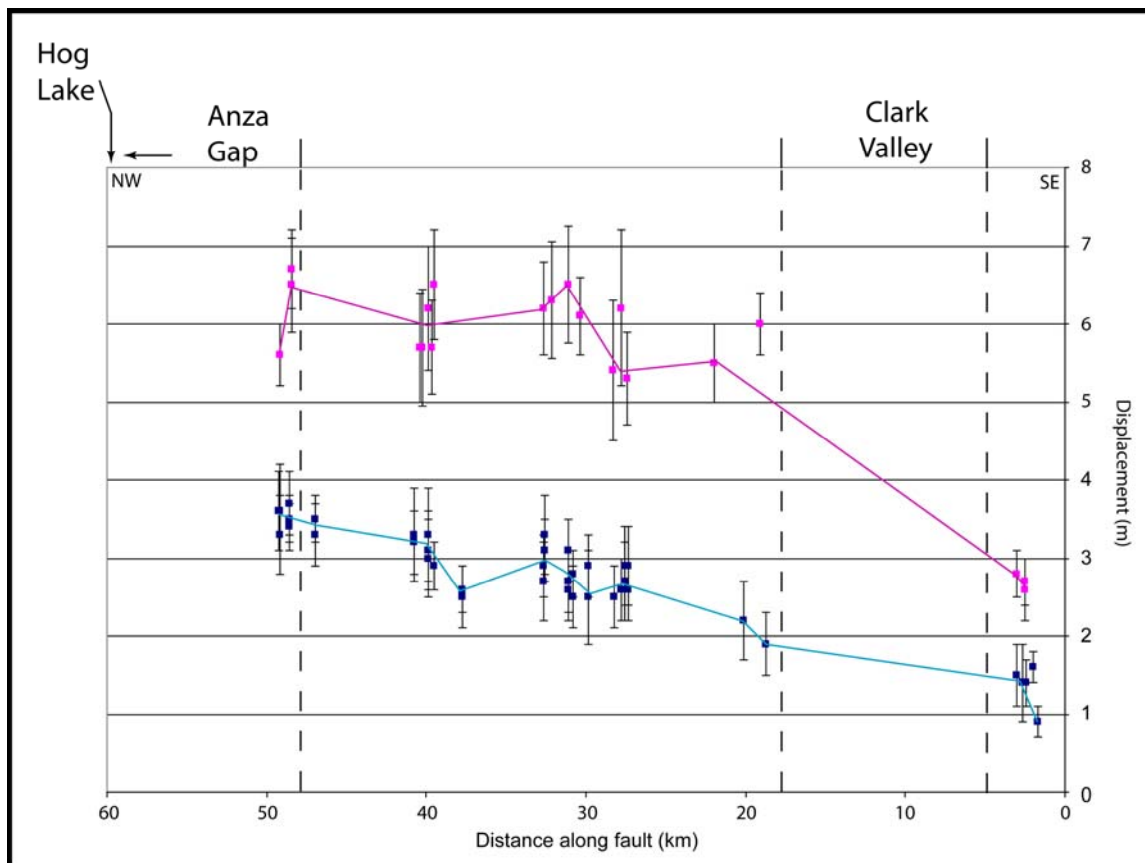


Figure 7. Slip distribution graph for the MRE (lower cluster, blue line) and past two events (upper cluster, pink line) from the Anza Valley south to the termination of the Clark fault near Lute Ridge. Data points represent the most reliable and best preserved features to estimate displacement.

area is defined as a 5-km section between the middle of the Anza Valley to the southern end of Sagebrush Flat (Figure 8). Through this section the fault is mapped as a linear, but locally buried trace with only a few minor splays. However, a few kilometers north of the focus area the Buck Ridge fault splays off from the main fault (Figure 5; Sharp, 1967).

I made 25 measurements at 10 localities along this section using LiDAR and field-based methods, with the results presented in Table 1. In general, the measurements are of good to excellent quality, with only a few fair measurements where slip is distributed over a couple of strands that are about 2-3 m apart. The data form two separate clusters of slip measurements; the lower cluster is assumed to represent slip in the most recent event averaging, 3.3 m (Figure 8). The upper cluster represents larger slip values but contains only four measurements that average about 6 m and interpreted to represent slip from the past two surface ruptures (Figure 8).

BV-8

BV-8 is a small ephemeral channel located in the Anza Valley where the Clark fault produces a small, but prominent, southwest facing scarp (Figure 8; Sharp 1972). The channel drains perpendicular to the scarp, with well developed channel margins. The southeast and northwest channel margins, as well as the thalweg, were recognized to be offset and measured in the field; I subsequently estimated their displacement by LiDAR. From field observations, average slip measurements of the channel features are ~3.0 m for the MRE, 30 cm lower than the overall average for this section (Figure 9). This results, in part, from the measurement of the southeast margin of 2.6 ± 0.4 m being 60 cm lower than the northwest margin and 70 cm lower than the thalweg. Offsets estimated by LiDAR

Table 1. Anza-Burnt Valley Displacement Data (BV)

#	Location	Feature	Longitude	Latitude	Distance along fault	Meters ^a	±	Confidence	Meters ^b	±	Confidence
1	BV-1	TH	537733	3711403	46.92	3.3	0.4	7.5	3.2	0.5	7.5
2		NW				3.5	0.3	7.5			
3	BV-A	TH	536748	3712306	48.24				3	0.3	8
4		NW							3	0.4	7
5		SE							3.2	0.3	7
6	BV-2	TH	536724	3712345	48.28	3.2	0.4	5.5			
7	BV-3	TH	536602	3712424	48.43	3.5	0.5	7.5	3.1	0.3	7
8		SE				3.4	0.4	7.5	3.2	0.4	7
9	BV-B	TH	536581	3712442	48.46				6.5	0.6	7
10		NW	536581						6.7	0.5	7
11	BV-4	TH	536541	3712464	48.50	3.7	0.3	7.75	3.4	0.5	7
12		TH				2.8	0.4	7			
13	BV-5	TH	536499	3712504	48.56	3.5	0.3	9.5	3.8	0.4	8
14		SE				3.7	0.4	9.5	3.9	0.4	8
15		NW				3.4	0.3	9.5	4	0.5	8
16	BV-6	NW	535989	3712877	49.19	3.3	0.5	7.75			
17		TH				3.6	0.6	7.75			
18		TH				5.4	0.6	6.5	5.6	0.4	7
19	BV-7	TH	535958	3712894	49.23	2.4	0.4	7			
20		TH				3.6	0.5	7.75	3.5	0.4	7
21		NW							3.2	0.3	7
22	BV-8	TH	533730	3714456	51.95	3.3	0.3	7.5	3.1	0.3	7.5
23		NW				3.2	0.4	7.5	3.4	0.4	7.5
24		SE				2.6	0.4	7.5	3.3	0.4	6.75

Note: ^a denotes measurements in the field.

^b denotes measurements made by LiDAR.

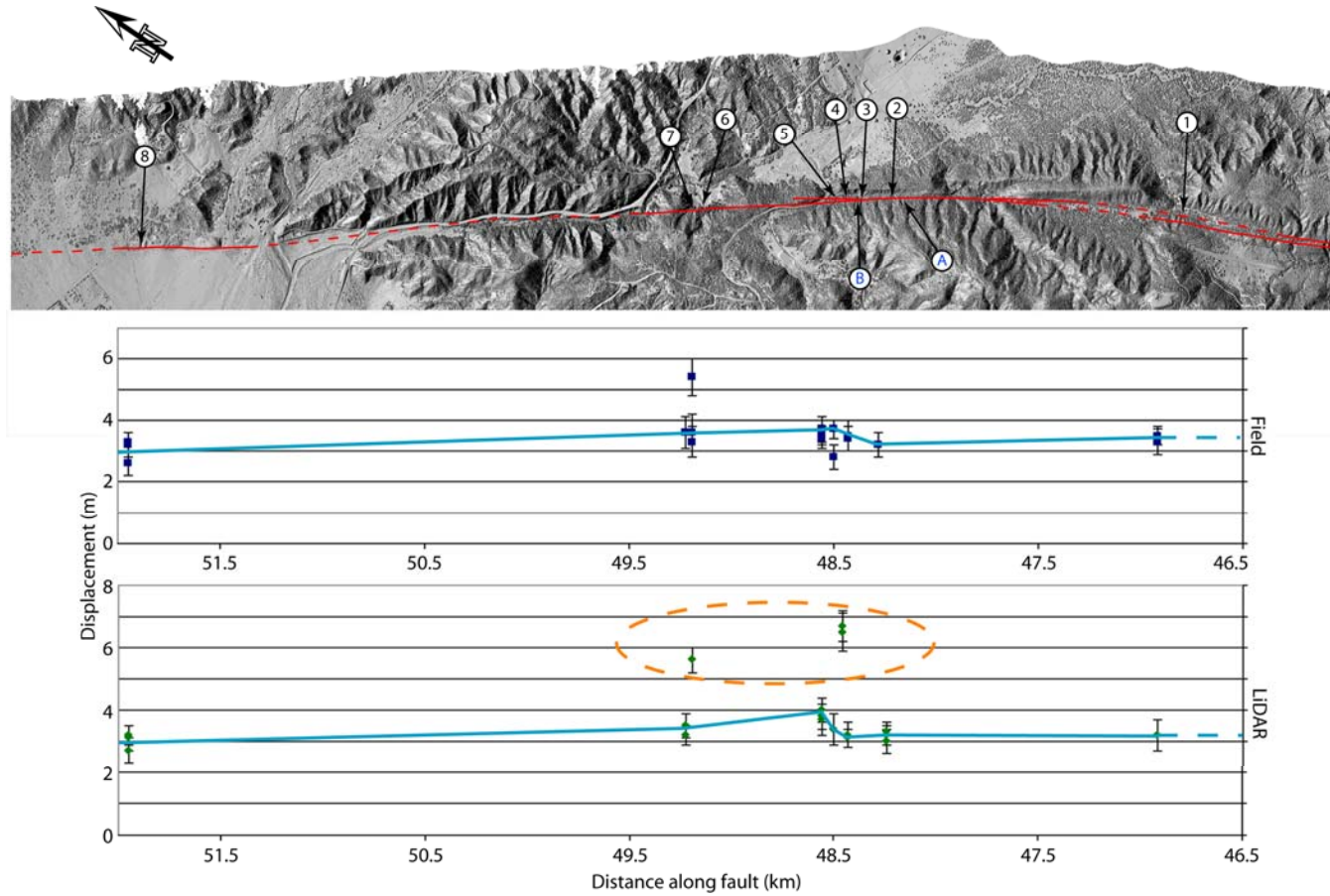


Figure 8. Annotated LiDAR DEM of the Anza and Burnt Valley section. Graphs display estimated displacement from field work and high resolution LiDAR DEM's. Blue lines connect estimates of displacement in the MRE while the orange circle is inferred as offset from the past two events.

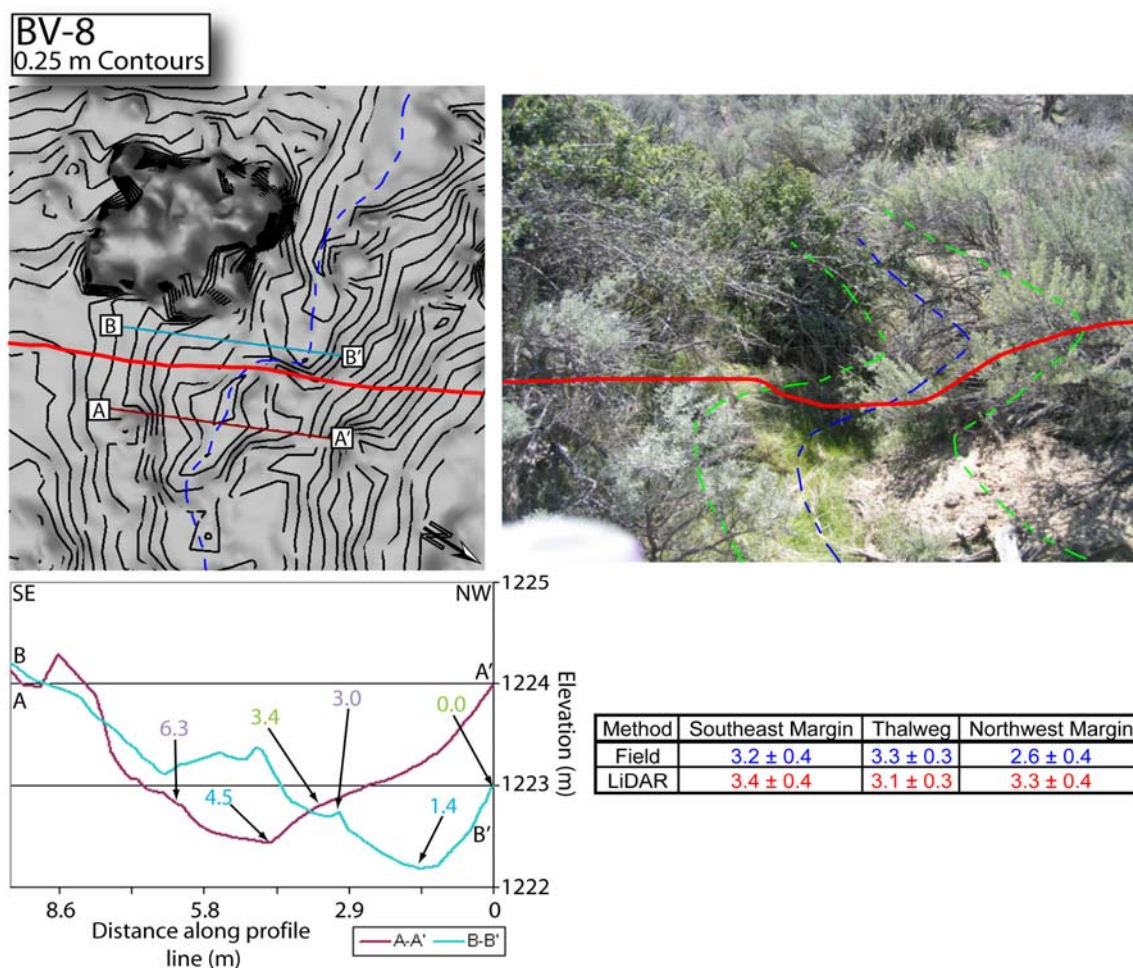


Figure 9. Annotated topographic map and photograph of BV-8 (UTM Zone 11, 533730 N, 3714456 E) in Anza Valley. The measured field and LiDAR displacements are shown in the table for the channel margins and thalweg. Channel thalwegs are shown as blue lines, channel margins are green lines, and the fault trace is the red line. The numbers on the channel cross-sections represent distances along the profile line, referenced parallel to the fault. All locality figures are annotated similarly from here on.

coincide with the section average estimating 3.3 ± 0.4 m of slip for the southeast margin during the MRE. During the field investigation proper projection of the channel features was difficult due to the thick vegetation in the area. I attribute the discrepancy between field measurements and those estimated by LiDAR to be a result of the vegetation. LiDAR was able to estimate the overall trend of the offset feature with more accuracy.

BV-5

This site is located to the west of Burnt Valley, about 500 m southeast of Burnt Valley Road, where previous mapping has located multiple active strands (Figure 5; Sharp 1972). The northeastern strand is inferred to be the active stand for the most recent event based upon the presences of fresh and well preserved offsets; however, it is possible for a portion of slip during the MRE to have also occurred on the southwestern strand so my estimate is a minimum value. This ephemeral rill has well preserved channel morphology, partly due to the dense vegetation of the area dispersing rainfall energy. Offsets from the MRE for the southeast and northwest channel margins were measured in the field, yielding 3.7 ± 0.4 m and 3.4 ± 0.3 m, respectively (Figure 10). For the same offset features, estimated measurements by LiDAR are slightly higher by roughly 30 cm. The same is true for measurements approximated for the thalweg of the channel, where offset in the field was measured at 3.5 ± 0.3 m and 30 cm higher by LiDAR for slip during the MRE.

HORSE CANYON AND WHITE WASH

Southeast of the Anza - Burnt Valley section, the Clark fault makes a small restraining bend before dropping about 300 m into Horse Canyon and White Wash (Figure 5; Sharp, 1967; 1972). Within this section, the fault is fairly continuous for this 4-km stretch

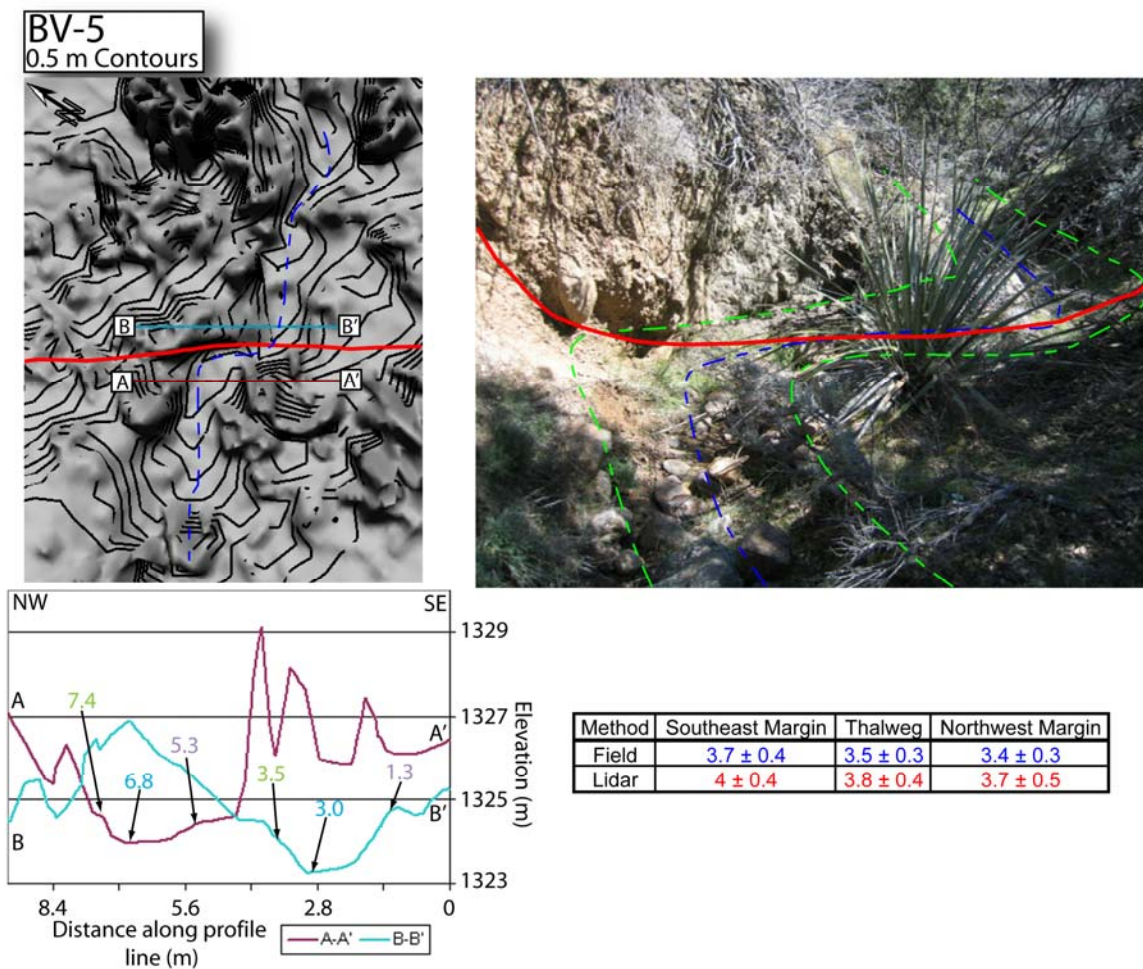


Figure 10. Topographic map and interpreted photograph of BV-5 (UTM zone 11, 536499 E, 3712504 N) near Burnt Valley. Measured displacements from field work and LiDAR DEM's are presented in the table.

before heading up into White Wash (Figure 11). Due to the drop in elevation, and consequent drop in precipitation, the dense brush seen in the previous section gives way to sporadic cactus and yucca plants. However, thick vegetation is still prominent in some areas due to annual springs along the fault. In general, geomorphology along this section is preserved with a few highly dissected benches and offset stream channels.

In total, 49 measurements were made on 18 channel features that ranged from fair to good quality (Table 2). The majority of the field measurements recorded slip during the MRE, while the LiDAR was able to resolve far-field deflection, which probably represents additional slip from the penultimate event. Based on measuring both the near-field abrupt deflection as slip in the MRE, and far-field deflection, I have made estimates for slip for the past two surface rupturing events for many features.

Slip for the MRE is slightly lower than for the preceding section and averages ~ 3 m of offset, while double event offsets record about 5.7 m of slip (Figure 11). The average slip measurement for double event offsets only contains five estimates, a couple of which have relatively low confidence, and may not reflect the true amount of slip.

HC-WW-8

This site is located in an area in which Sharp (1972) has labeled as “moderately dissected benches” along a ridge front where fault location is very good. Due to the marginal vegetation at this site, both channel margins and the thalweg provide good projections into the fault trace for the near-field offset in the field and far-field offset assessed by LiDAR. Estimates for slip in the MRE are similar when the field measurements are compared to those estimated by LiDAR. Both methods estimate about 2.9-3.2 m of slip occurred during the

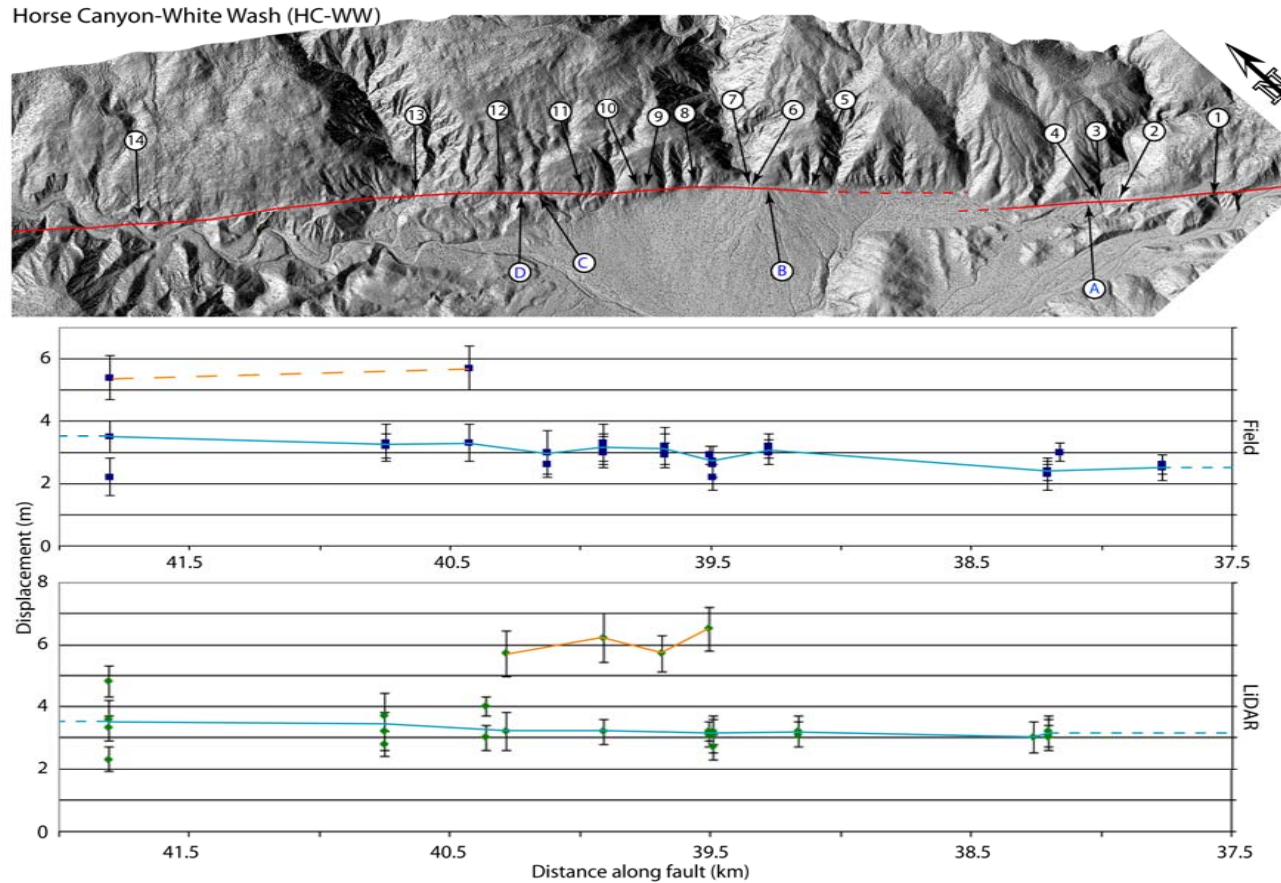


Figure 11. Annotated LiDAR DEM of the Horse Canyon-White Wash (HC-WW) section with localities where offsets were estimated. Letters denote where displacement was measured by LiDAR only. Displacements estimated in the field and from LiDAR DEM's are presented in table 2 and shown here. Blue lines connect displacements inferred to be from the MRE. Orange lines roughly connect slip accrued during the past two events.

Table 2. Horse Canyon and White Wash Displacement Data (HC-WW)

#	Location	Feature	Longitude	Latitude	Distance along fault	Meters ^a	±	Confidence	Meters ^b	±	Confidence
1	WW-1	SE	544649	3705282	37.77	2.6	0.3	6			
2		NW				2.5	0.4	6			
3	WW-2	TH	544334	3705524	38.16	3	0.3	6.5			
4	WW-3	SE	544300	3705554	38.21	2.4	0.3	6.5	3	0.4	7
5		NW				2.3	0.3	6.5	3.1	0.5	7
6		TH							3.2	0.5	7
7	WW-4	B				2.3	0.5	6.5			
8	WW-A	TH	544250	3705583	38.26				3	0.5	6.5
9	WW-5U	NW	543561	3706384	39.28	1.9	0.3	7			
10	L	NW				1.1	0.5	6			
11	T	NW				3	0.4	6.5			
12	U	TH				1.8	0.5	6.5			
13	L	TH				1.3	0.5	6			
14	U	TH				3.1	0.5	6.25			
15	U	SE				2	0.3	7			
16	L	SE				1.2	0.4	6.5			
17	T	SE				3.2	0.4	6.75			
18	WW-B	SE	543634	3706282	39.16				3.2	0.5	7
19		TH							3.1	0.4	7
20	WW-6	TH	543394	3706519	39.49	2.2	0.4	7	2.4	0.6	7
21		NW				2.7	0.5	7	2.6	0.4	7
22		SE				2.6	0.4	7	2.7	0.4	7
23	WW-7	SE	543388	3706531	39.50	2.9	0.3	7.5	3.4	0.3	7.5
24		TH							3.2	0.4	7.5
25		TH							6.5	0.7	7
26	WW-8	TH	543279	3706681	39.68	3.1	0.5	7.5	3.2	0.5	7.5
27		SE				2.9	0.4	7.5	2.9	0.6	7
28		NW				3.2	0.6	7	3.1	0.3	7.5

Table continues

Table 2 (Continued)

#	Location	Feature	Longitude	Latitude	Distance along fault			Confidence	Distance along fault		
					Meters ^a	±	Confidence		Meters ^b	±	Confidence
29		TH	543275	3706694	39.69				5.9	0.6	7
30	WW-9	SE	543112	3706808	39.89	2.1	0.6	5.5			
31	WW-10	TH	543098	3706831	39.91				6.2	0.8	5.5
32		NW				3	0.5	7.5	3.2	0.4	7
33		TH				3.1	0.5	7.5			
34		SE				3.3	0.6	7			
35	WW-11	SE	542932	3706975	40.13	3	0.7	7			
36		TH				2.6	0.4	7			
37	WW-D	TH	542837	3707106	40.28				3.2	0.6	7.5
38		NW							5.7	0.75	7
39	WW-E	TH	542765	3707142	40.36				3	0.4	6.5
40		SE							4	0.3	6.5
41	WW-12	SE	542716	3707188	40.43	5.7	0.7	6.5			
42		TH				3.3	0.6	6			
43	WW-13	TH	542500	3707442	40.75	3.2	0.4	8	3.2	0.6	7
44		B				3.3	0.6	6	2.8	0.4	7
45		SE							3.7	0.7	6
46	WW-14	SE	541645	3708068	41.81	3.5	0.5	7	3.6	0.6	6.5
47		SE				5.4	0.7	7.5	4.8	0.5	7
48		TH							3.3	0.4	6.5
49		NW				2.2	0.6	7	2.3	0.4	7

Note: ^a denotes measurements in the field.

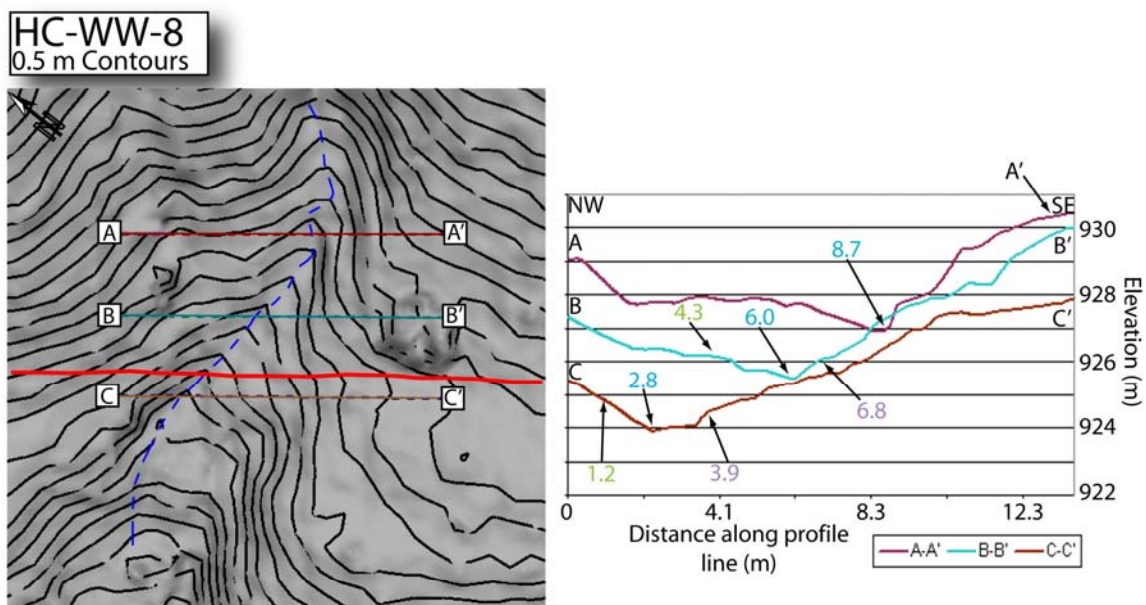
^b denotes measurements made by LiDAR.

MRE, similar to the average amount of slip for the section (Figure 12). Although not recognized in the field, LiDAR imagery was able to see the far-field deflection of the thalweg measuring ~ 5.9 m of slip, which is about double the MRE.

HC-WW-6, 7

HC-WW-6 and 7 are located 5 m from each other on a young alluvial fan surface where previous attempts to locate the active strand failed (Sharp, 1972). After careful investigation, I found a prominent jog in the active channel (HC-WW-7) along strike with the projection of the fault trace. From this, displacement in the MRE and the penultimate event were recorded. The southeast margin is the best preserved feature for estimating offset during the MRE, with 2.9 ± 0.3 m of measured slip in the field and 3.2 ± 0.3 by LiDAR (Figure 13). In the field the channel thalweg was difficult to project and therefore not measured; however, from the LiDAR data, near-field and far-field offsets are estimated at 3.1 ± 0.4 m and 6.5 ± 0.7 m, respectively.

Vegetation in the active channel (HC-WW-7) is light; however, channel HC-WW-6 contains dense vegetation directly on the projected fault trace, which lowers the confidence for both the LiDAR and field measurements. The field measurements are slightly lower than the average for this section, ranging from as low as 2.2 ± 0.4 for the thalweg up to 2.7 ± 0.5 m for the northwest margin (Figure 14). Slip estimates based on the LiDAR DEM's are similar. Estimates from both methods are lower than the section average by 30-70 cm. The lower values are directly attributed to the uncertainties created by the vegetation, which does not allow for proper projection and measurement of the channel features at the fault trace.



Method	Northwest Margin	Thalweg	Southeast Margin	Far-field Thalweg
Field	3.2 ± 0.6	3.1 ± 0.5	2.9 ± 0.4	---
LiDAR	3.1 ± 0.3	3.2 ± 0.5	2.9 ± 0.6	5.9 ± 0.6

Figure 12. Annotated topographic map and cross-section lines of HC-WW-8 (UTM zone 11, 543279 E, 3706681 N) generated from the LiDAR DEM's. Offset estimates assessed from field work and by LiDAR DEM's are presented in the table.

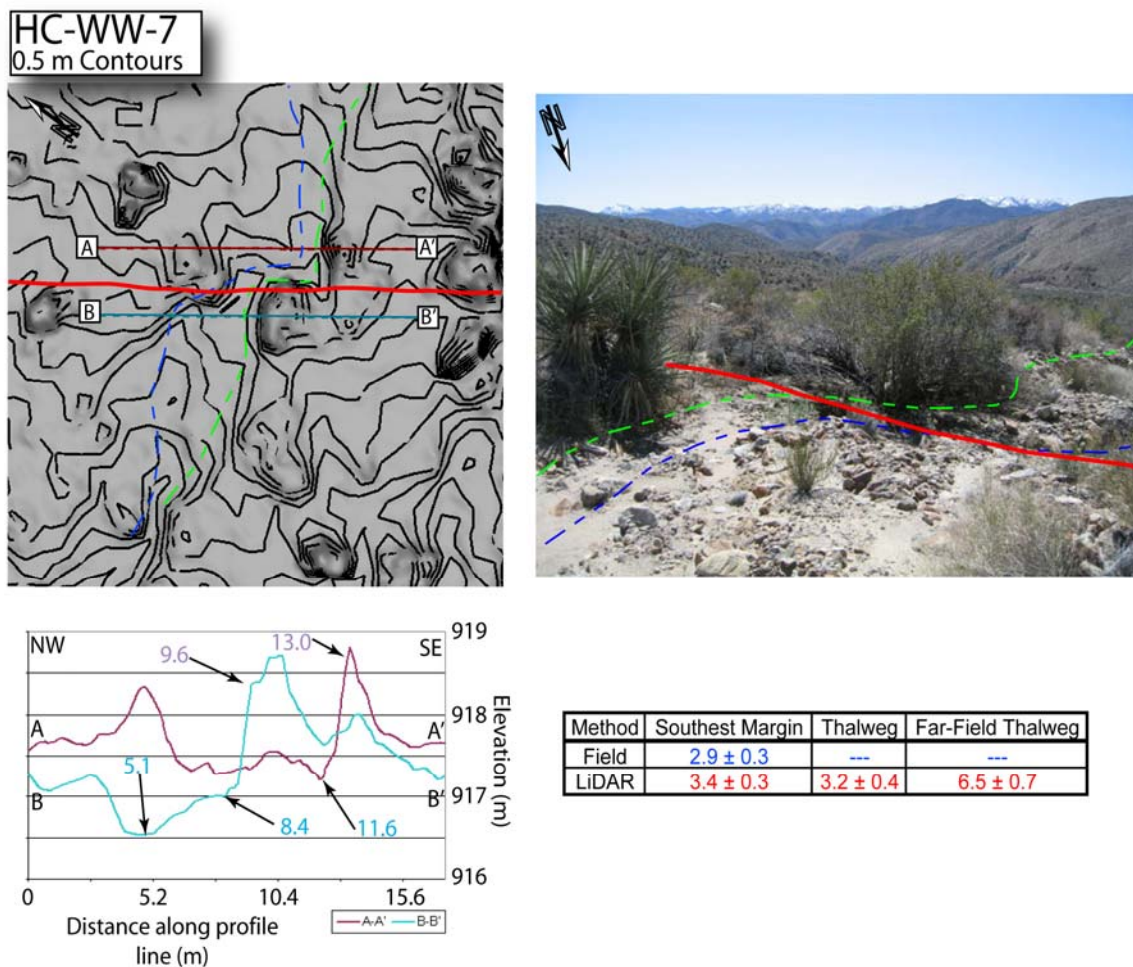


Figure 13. Interpreted photograph and topographic map of HC-WW-7 (UTM zone 11, 543388 E, 3706531 N). Displacements of the southeast margin and thalweg, both near- and far-field, were measured from LiDAR DEM's and through field observations and showed in the table.

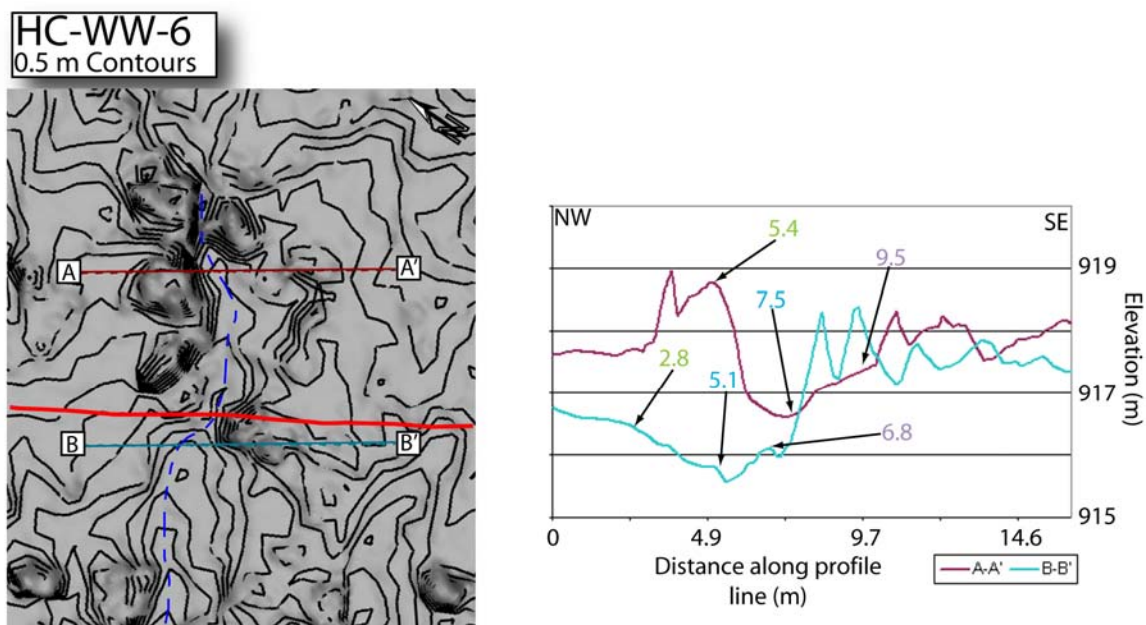


Figure 14. Topographic map and cross-section lines of HC-WW-6 (UTM zone 11, 543394 E, 3706519 N) generated by the LiDAR data set. Offsets of both channel margins and the thalweg as measured in the field and by LiDAR DEM's are presented in the table.

DRY WASH

To the south of White Wash, the Clark fault makes another restraining bend before opening up into the Dry Wash section (Figure 15). In general, the mapped trace is linear and continuous throughout the 4-km Dry Wash section, with well exposed fault geomorphology localized along the southwest side of the valley. Vegetation is no longer a concern for this section, as the annual precipitation and elevation are both considerably lower. However, topography is steep and large boulders in excess of 3 m locally occupy the channel margins and clog the thalwegs. As a result, errors assessed in the field are slightly larger than for the previous two sections.

I located eighteen offset channels and ridges in the field that were deemed suitable to resolve slip, with an additional five measured only from the LiDAR DEM's. These yielded a total of 64 measurements on 44 discrete geomorphic features, which ranged from fair to good quality (Table 3a), with many measured by both LiDAR and field techniques. The data forms tight clusters around three distinct slip values, with the lowest value inferred to be slip during the most recent event. Slip for the MRE averages around 2.8 m, with the next largest cluster of offsets almost doubling the MRE at 5.5 m (Figure 16). Although only constrained by two measurements, the highest slip measurements at about 8.9 m is assumed to be the result of the slip in the past three events. Confidence on this largest estimate is low, and may not accurately reflect the actual amount of slip.

DW-18

DW-18 is the farthest north deflected rill observed in the Dry Wash section, just southeast of where the Clark fault is expressed at the surface as a shallow angle thrust

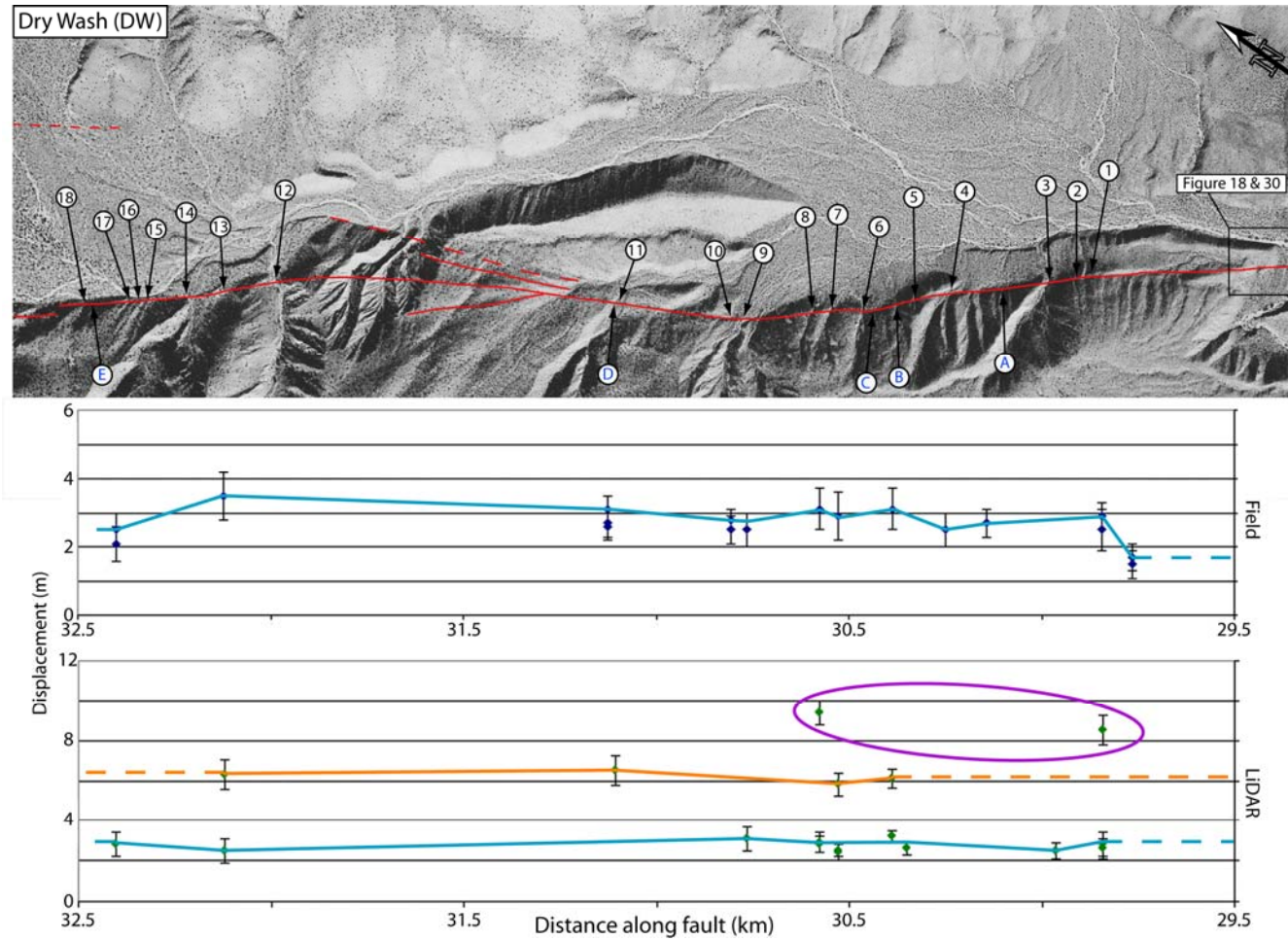


Figure 15. Annotated aerial photograph of Dry Wash (DW) section showing measured localities. Slip distribution graphs are presented for displacements measured from field and the LiDAR data. Letters denote where only LiDAR measurements are available. Blue, orange, and purple represent single, double and triple events, respectively.

Table 3. (a) Dry Wash Displacement Data (DW). (b) Dry Wash-Jackass Ridge Displacement Data (DW-JAR)

Dry Wash Displacement Data											
#	Location	Feature	Longitude	Latitude	Distance along fault	Meters ^a	±	Confidence	Meters ^b	±	Confidence
1	DW-1	TH	551510	3701100	29.73	12.5	1.5	4.5	16	2	4
2	DW-2	SE	551483	3701115	29.77	1.5	0.4	6			
3		TH			29.77	1.7	0.4				
4	DW-3	BC	551418	3701157	29.84	2.9	0.4	8.5	2.8	0.6	7.5
5		TH			29.84	2.5	0.6	7.5	2.6	0.5	7
6		SE							8.5	0.75	7
7	DW-A	TH	551307	3701207	29.96				2.5	0.4	7
8	DW-4	NW	551149	3701297	30.14	2.7	0.4	6.5	2.8	0.5	<5
9	DW-5	NW	551054	3701346	30.25	2.5	0.5	6	3.2	0.6	5
10	DW-B	BW	551013	3701362	30.29				6.5	1	5
11	DW-C	SE	550945	3701359	30.35				2.6	0.3	6.5
12	DW-6	NW	550925	3701399	30.39	3.1	0.6	6.5	3.2	0.3	7.5
13		NW							6.1	0.5	7
14	DW-7	NW	550800	3701463	30.53	2.9	0.7	6	2.4	0.4	7.5
15		NW							5.8	0.6	6
16		TH							2.5	0.3	7.5
17	DW-8	NW	550762	3701494	30.58	3.1	0.6	7	2.8	0.4	7.5
18		NW							9.4	0.6	6.5
19		TH							2.9	0.5	6
20	DW-9	R	550606	3701600	30.76	2.5	0.5	7	3.1	0.6	5.5
21	DW-10	SE	550560	3701606	30.81	2.8	0.3	7			
22		TH			30.81	2.5	0.4	7			
23	DW-11	NW	550367	3701892	31.12	3.1	0.4	7.75	2.8	0.3	
24		TH			31.12	2.6	0.4	7.75	2.6	0.4	
25		SE			31.12	2.7	0.4	7.75	2.6	0.3	
26	DW-D	NW	550382	3701879	31.10				6.5	0.75	6
27	DW-12	NW	549605	3702547	32.12	3.5	0.7	7.5	6.3	0.75	6

Table continues

Table 3 (Continued)

Dry Wash Displacement Data											
#	Location	Feature	Longitude	Latitude	Distance along fault	Meters ^a	±	Confidence	Meters ^b	±	Confidence
28		TH							2.5	0.6	6
29	DW-13	TH	549413	3702580	32.30	4.6	0.4	6.5			
30	DW-14	SE	549312	3702612	32.40	2.1	0.5	6			
31		TH			32.40	2.5	0.5	6.5	2.8	0.6	6.5
32	DW-15	NW	549212	3702662	32.51	4.9	0.6	6	4.3	0.5	6.5
33		B			32.51	3.1	0.5	5.5			
34		TH							3.2	0.4	7
35	DW-16	NW	549179	3702687	32.55	3.3	0.5	7.5	2.6	0.6	7
36		TH			32.55	3.1	0.4	7.5	2.7	0.3	7.5
37	DW-17	NW	549161	3702697	32.57	3.1	0.4	6.5	3.9	0.6	6
38		TH							2.9	0.5	7.5
39	DW-18	TH	549104	3702763	32.66	2.7	0.5	7.5	3.2	0.3	7.5
40		TH							5.9	0.6	6
41		NW				2.9	0.4	7.5	2.9	0.3	7.5
42	DW-E	NW	549062	3702792	32.67				2.7	0.4	7
43		TH			32.67				2.8	0.6	6

Dry Wash-Jackass Ridge Displacement Data (DW-JAR)

#	Location	Feature	Longitude	Latitude	Distance along fault	Meters ^a	±	Confidence	Meters ^b	±	Confidence
68	DW-JAR-1	B	552153	3700704	28.98	2.7	0.5	7.5	2.6	0.4	7
69	DW-JAR-2	TH	552139	3700708	28.99	2.5	0.3	6	2.3	0.4	7
70	DW-JAR-3	SE	552123	3700715	29.01	2.8	0.5	6.5	2.9	0.3	7.5
71		TH				2.5	0.4	7	2.6	0.3	7.5
72	DW-JAR-4	NW	552091	3700734	29.05				2.5	0.4	7.5
73	DW-JAR-5	B							17	1	8

Note: ^a denotes measurements in the field.

^b denotes measurements made by LiDAR.

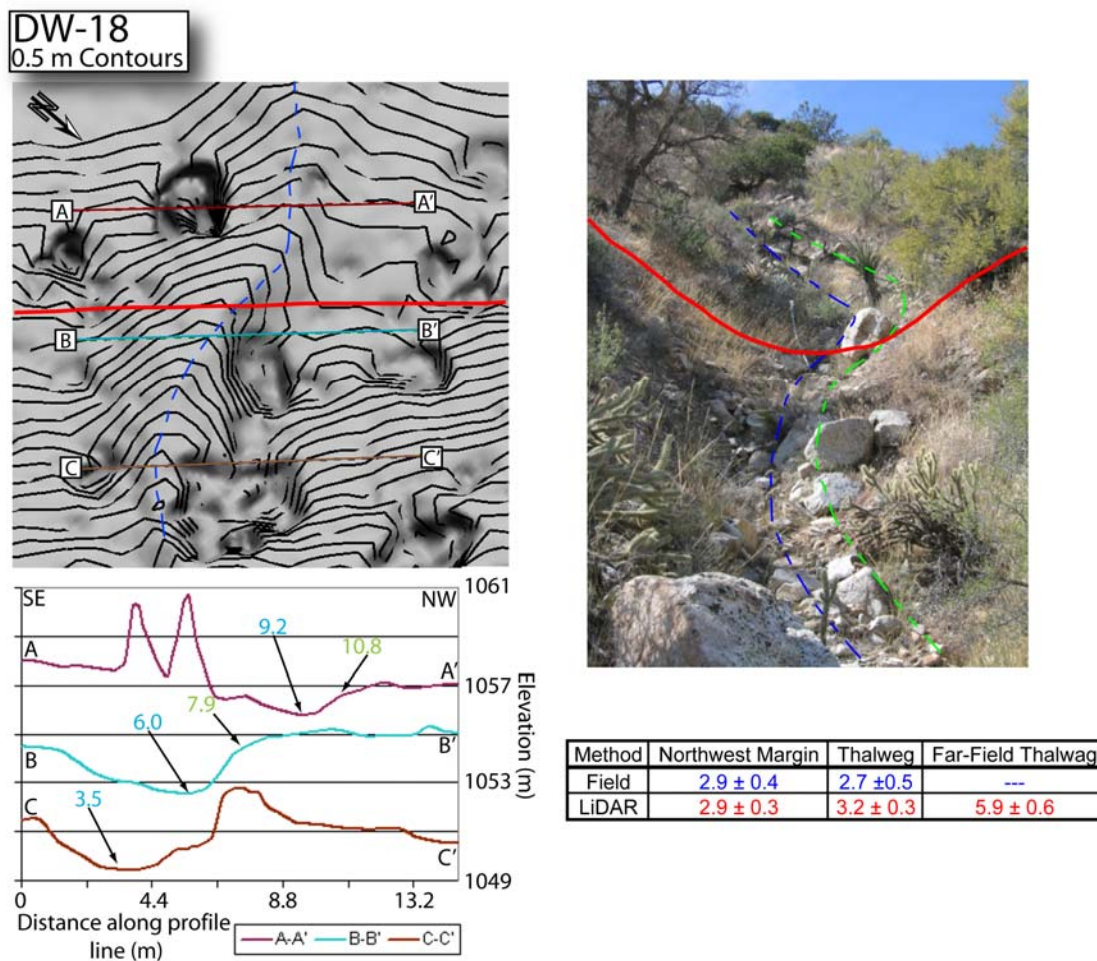


Figure 16. LiDAR generated topographic map and cross-section profile as well as annotated field photograph of DW-18 (UTM zone 11, 549104 E, 3702763 N). Displacement measured in the field and by LiDAR DEM's of the northwest margin and thalweg, near- and far-field, are shown in the table.

(Figure 15; Sharp, 1972). The fault trace is well constrained, with the majority of slip occurring in a narrow zone of deformation. The rill is nearly perpendicular to the fault trace with the near-field offsets appearing fresh in the field. The far-field deflection of the thalweg was observed in the field but only estimated with the use of LiDAR imagery. Measurements of the near-field northwest margin and thalweg are similar to the section average of ~2.8 m, with only a 10-50 cm difference, which is attributed to slip during the MRE (Figure 16). With the LiDAR DEM's, the far-field thalweg deflection was estimated at 5.9 ± 0.6 m, almost double the MRE. This is interpreted to be the result of the past two events, implying that the previous earthquake was as large as the last.

DW-11

A small well developed channel crosses the active fault just north of where the main trace splays into several minor strands (Figure 15; Sharp, 1972). From field investigations, it is inferred that most of the recent slip has occurred on the central strand, and thus offset measurements were estimated there. Nevertheless, these estimates should be considered minimum values. The channel contains large boulders that are up to 2 m across. However, the overall channel morphology is well developed with both channel margins and the thalweg recognizable and well-defined. Estimates from the field and by LiDAR are similar to the section average for the MRE of 2.8 m, ranging from 2.6-3.2 m for all the channel features (Figure 17).

DW-JAR

A system of distinctive bars and swales are clearly offset from their correlatives where Dry Wash crosses the Clark fault (Figures. 15 and 18). Across the wash, the

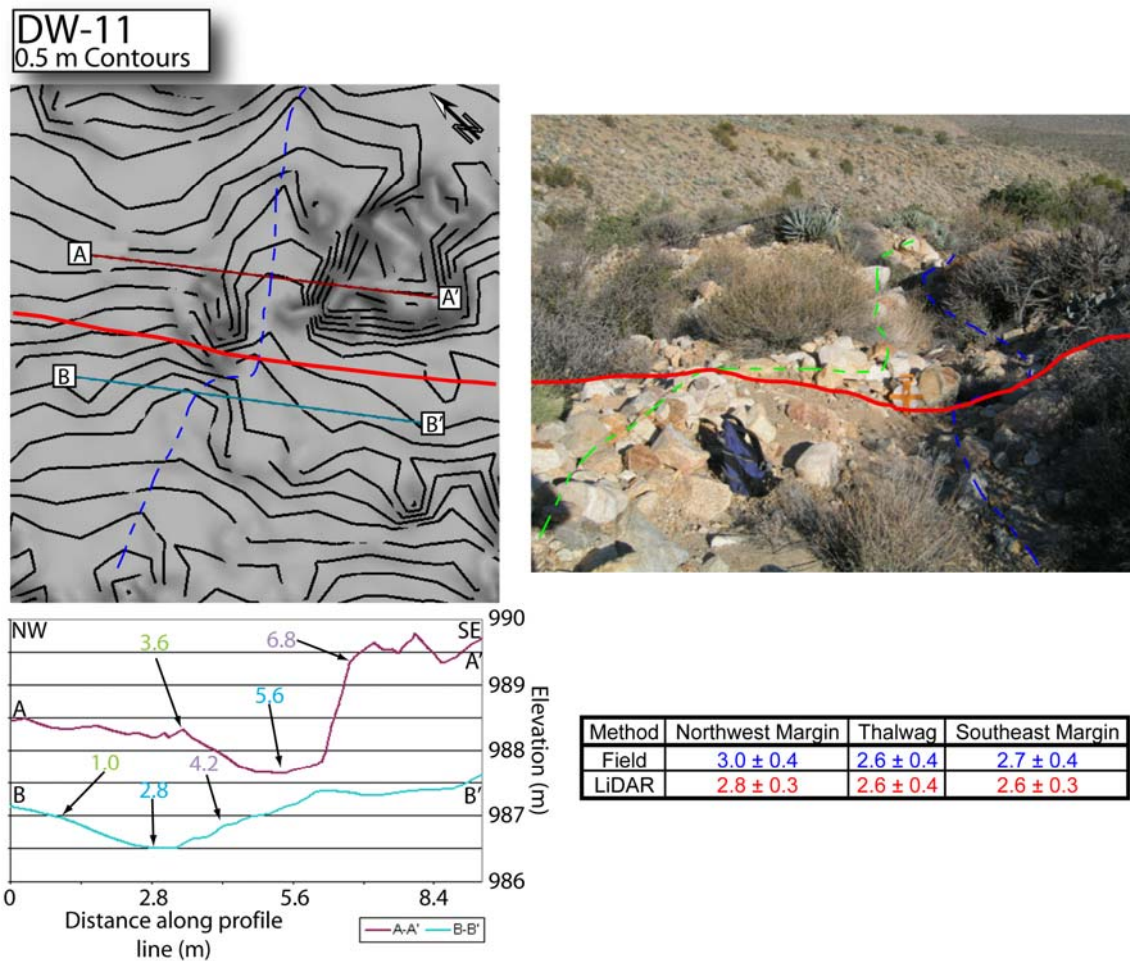
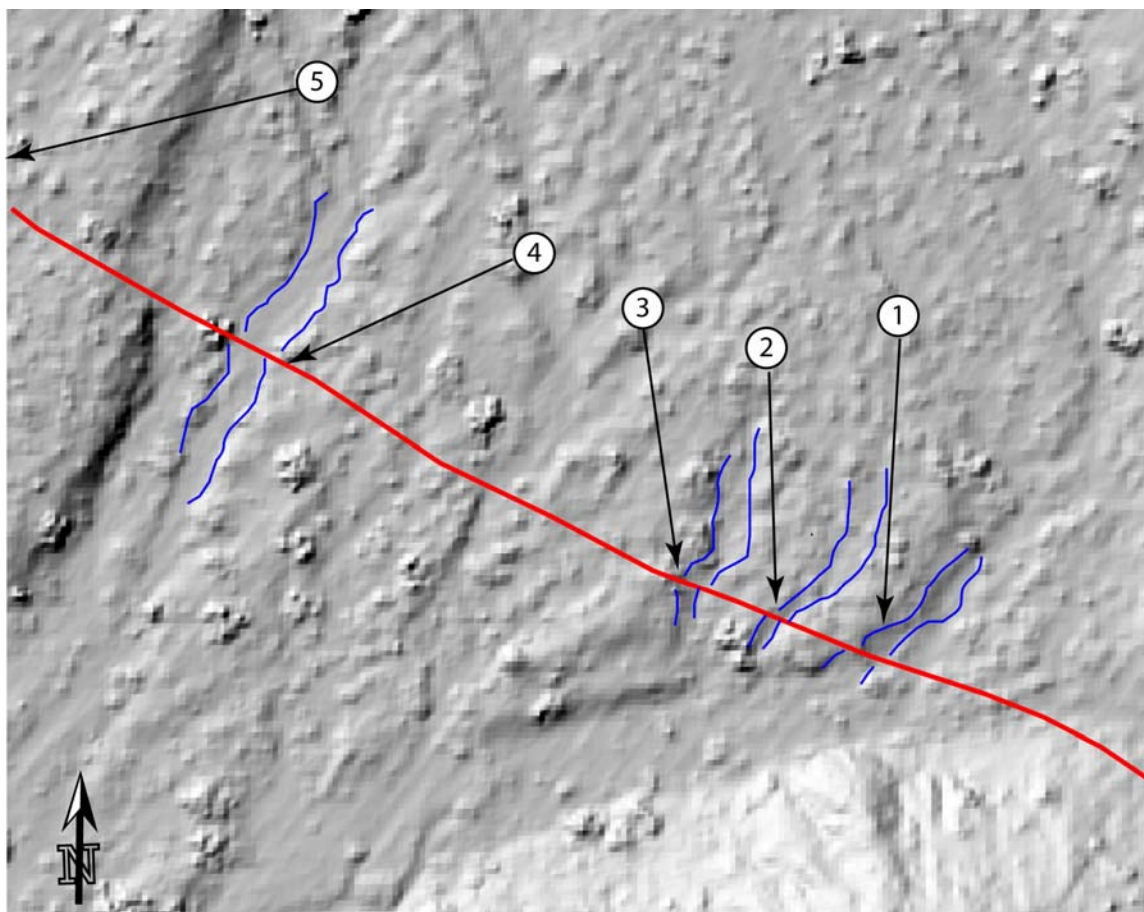


Figure 17. Map and interpreted field photograph of offset channel DW-11 (UTM zone 11, 550367 E, 3701892 N) on the west side of Dry Wash. Offset estimated by LiDAR and in the field for both channel margins and the thalweg are presented in the table.



Method	DW-JAR 1 Bar	DW-JAR 2 Thalweg	DW-JAR 3 Southeast Margin	DW-JAR 4 Thalweg	DW-JAR 4 Northwest Margin	DW-JAR 5 Bar Complex
Field	2.7 ± 0.5	2.5 ± 0.3	2.8 ± 0.5	2.5 ± 0.4	---	---
LiDAR	2.6 ± 0.4	2.3 ± 0.4	2.9 ± 0.3	2.6 ± 0.3	2.5 ± 0.4	17.0 ± 1.0

Figure 18. Annotated LiDAR DEM of DW-JAR where Dry Wash crosses the fault just north of Jackass Ridge (UTM zone 11, 552123 E, 3700715 N). Displacements assessed in the field and by LiDAR DEM's on five rills and bars, which are displayed in the table. A detailed reconstruction of site five can be seen in Figure 30.

expression of the fault is well preserved with slip occurring on one principle strand that was previously unrecognized by Sharp (1972). Two sets of observations can be made here; slip during the last event as well as a multi-event offset. The lesser values, slip during the MRE, are presented here, while the larger offsets will be presented in a following section.

Slip for the MRE was recognized in small abandoned channels within the active wash. Four features were measured on three separate channels, totaling nine separate measurements. The average offset for the MRE is slightly lower than the average for the section. However, they are in close proximity to the next section in which slip estimates for the MRE appear lower. In the MRE an estimated average of 2.6 m of slip occurred within the active wash, with measurements varying by only ± 30 cm (Table 3b).

JACKASS RIDGE

Along Jackass Ridge, the fault trace is very continuous, producing a prominent 2-3 m wide bench across steep topography (Figure 19). Unlike the other sections, the fault juxtaposes sedimentary rock against sedimentary rock of the Bautista Formation. The easily erodeable formation provides the best section for geomorphic studies due to the high density of rills and drainages over a short, 1-km section. Throughout the section, the majority of slip occurs between the front and back edge of the bench, with a few places showing prominent scarps from the MRE, mainly on the front edge. Toward the southern end of the section, the fault is splayed, with one strand extending farther up the ridge. After careful field and aerial investigation, no recent slip has occurred on this branch.

Jackass Ridge is the only section in which slip was estimated by aerial photography along with field and LiDAR techniques. In all, 26 locations were investigated allowing for

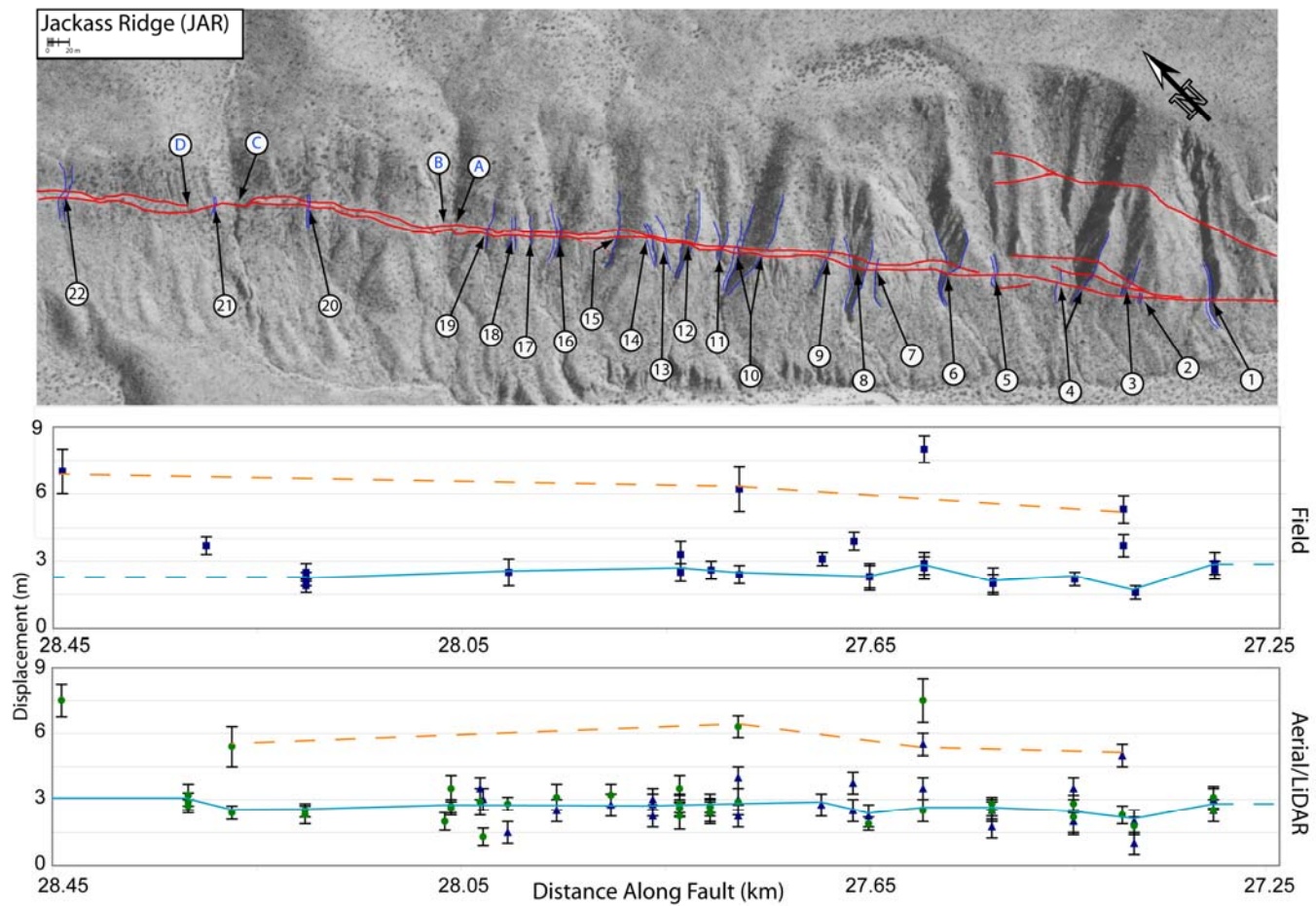


Figure 19. Annotated aerial photograph of Jackass Ridge (JAR) with the locations of displaced features shown. Letter labeled sites are where displacements were estimated from the LiDAR DEM's only. Slip distribution graphs are presented for estimates made in the field and by LiDAR/Aerial photographs. Blue and orange lines connect offsets that occurred from the MRE and past two events, respectively.

121 measurements on 67 distinctive features ranging from poor to excellent quality (Table 4). Uncertainties due to vegetation are minimal in this section; however, the steep topography produces large boulders that clog the thalweg and channel margins, and the scatter in slip estimates is attributed to be the direct result of these features. As before, slip measurements clustered around two distinctive values, 2.5 m and 5.6 m. The lesser value is inferred to be slip caused by the MRE and the higher, about double the slip in the MRE, to be the result of the past two events (Figure 19).

JAR-20

The ephemeral rill at JAR-20 is well developed and deeply incised nearly perpendicular to the prominent fault bench (Figure 20). The scarp is very fresh looking along the southwest edge of the bench and thus assumed to be the main active strand at this location. From field work, slip during the MRE for the southeast and northwest margins is estimated to be 2.5 ± 0.4 and 1.9 ± 0.3 m, respectively, and by LiDAR DEM's, the estimate is 2.3 ± 0.4 m for each feature. Field work resolved 2.2 ± 0.3 m of slip for the thalweg, whereas estimates from the LiDAR data were closer to the section average, at 2.5 ± 0.3 m. The overall average for JAR-20 is 20 cm lower than the section average.

JAR-11

A very well developed thalweg is offset 2.7 ± 0.3 m across a pronounced bench, based on estimates from the LiDAR data (Figure 21). In the field, the fault scarp is very fresh appearing, with minimal erosion and excellent definition of the piercing points, especially for the southeast margin, which recorded 2.6 ± 0.4 m of slip during the MRE. Offset of this same feature was estimated from LiDAR at 2.65 ± 0.4 m. This site is one of

Table 4. Jackass Ridge Displacement Data (JAR)

#	Location	Feature	Longitude	Latitude	Distance along fault	Meters ^a	±	Meters ^b	±	Confidence	Meters ^c	±	Confidence
1	JAR-1	TH	553551	3699798	27.31	2.5	0.5	2.6	0.4	8-9	2.5	0.5	8
2		NW			27.31	3		2.9	0.5	8-9	3.1	0.5	8
3	JAR-2	TH	553491	3699848	27.39	2		1.6	0.3	7.5	1.8	0.4	8
4		NW				1							
5	JAR-3L	SE	553479	3699851	27.40	3.5		3.7	0.5	6.5			
6	U	SE				1.5					2.3	0.4	6.5
7	T	SE				5							
8	L	NW				4		3.4	0.7	5.5			
9	U	NW				1		1.9	0.4	6			
10	T	NW				5		5.3	0.6				
11	JAR-4	SE	553437	3699874	27.45	2		2.2	0.3	6	2.2	0.8	6.5
12		NW				3.5					2.8	0.4	6.5
13	JAR-5	SE	553375	3699925	27.53	2.5		2.1	0.6	9.5	2.8	0.3	8.5
14		NW				1.75		2	0.4		2.5	0.4	8.5
15	JAR-6	SE	553318	3699961	27.60	5.5		8	0.6	7	7.5	1	7
16		SE						2.7	0.5	8.5	2.5	0.5	7
17		NW				3.5		2.9	0.5	8			
18	JAR-7L	NW	553258	3699967	27.65	1.5							
19	U	NW				0.75		2.3	0.6	7	1.9	0.3	7
20	T	NW				2.25		2.3	0.6				
21	L	SE	553245	3699975	27.67	1.75-2		2.3	0.4	7			
22	U	SE				0.5		1.6	0.4	8			
23	T	SE				2.5		3.9	0.4				
24	L	NW				2.75							
25	U	NW				1							
26	T	NW				3.75							
27	JAR-9L	R	553227	3700004	27.70	1.5		1	0.2	7.5			

Table continues

Table 4 (Continued)

#	Location	Feature	Longitude	Latitude	Distance along fault	Meters ^a	±	Meters ^b	±	Confidence	Meters ^c	±	Confidence
28	U	R				1.0-.25		2.1	0.4	7.5			
29	T	R				2.75		3.1	0.3				
30	JAR-10	SE	553160	3700050	27.78	4		6.2	1	6	6.3	0.5	7.5
31		TH				3		2.4	0.4	7.5	2.9	0.6	7.5
32		NW				2.0-.5							
33	JAR-11	SE	553133	3700059	27.81	2.75		2.6	0.4	7.5	2.65	0.4	7.5
34		TH									2.7	0.3	7.5
35		NW				2.5					2.7	0.5	7.5
36	JAR-12	SE	553111	3700080	27.84	2.75		2.5	0.4	6.5	2.6	0.4	6.5
37		R						3.3	0.6	7.5	3.5	0.6	7.5
38		NW				2.75					2.8	0.4	7.5
39	JAR-13	TH	553081	3700082	27.86	3							
40	JAR-14	SE	553081	3700082	27.86	2.25							
41		NW				2.75					2.25	0.6	6
42	JAR-15L	TH	553053	3700114	27.90	2							
43	U	TH				0.75-1							
44	T	TH				2.75					3.2	0.5	7
45	JAR-16	NW	553015	3700153	27.96	2.5		1.8	0.5	<5	3.1	0.6	7
46	JAR-17	TH	552965	3700164	28.00	1.5		2.5	0.6	5	2.8	0.3	7
47	JAR-18U	NW	552942	3700173	28.03	1.5							
48	L	NW				1.5					1.3	0.4	5.5
49	T	NW				3							
50	JAR-19	SE	552942	3700178	28.03	3.5		1.5	0.4		2.9	0.6	6
51	JAR-A	SE	552917	3700192	28.06						3.5	0.6	6
52		TH									2.6	0.3	7.5
53		NW									2.7	0.3	7
54	JAR-B	TH	552911	3700194	28.07						2	0.4	6
55	JAR-20	SE	552798	3700271	28.20			2.5	0.4	9.5	2.3	0.4	8

Table continues

Table 4 (Continued)

#	Location	Feature	Longitude	Latitude	Distance along fault	Meters ^a	±	Meters ^b	±	Confidence	Meters ^c	±	Confidence
56		TH						2.2	0.3	9.5	2.4	0.3	8
57		NW						1.9	0.3	9.5	2.2	0.4	8
58	JAR-21L	SE	552712	3700318	28.30			1.7	0.3	5.5			
59	U	TH						1.5	0.4	5.5			
60	L	TH						2.2	0.4	7			
61	T	TH						3.7	0.4				
62	JAR-C U	SE	552736	3700307	28.27						2.4	0.3	6
63	T	SE									5.4	0.9	5
64	JAR-D	SE	552694	3700321	28.32						2.9	0.4	6.5
65		TH									2.7	0.3	6.5
66		NW									3.2	0.5	5.5
67	JAR 22	SE	552589	3700387	28.44			7	1	6.5	7.5	0.75	6

Note: ^a denotes measurements made from aerial photography.

^b denotes measurements in the field.

^c denotes measurements made by LiDAR.

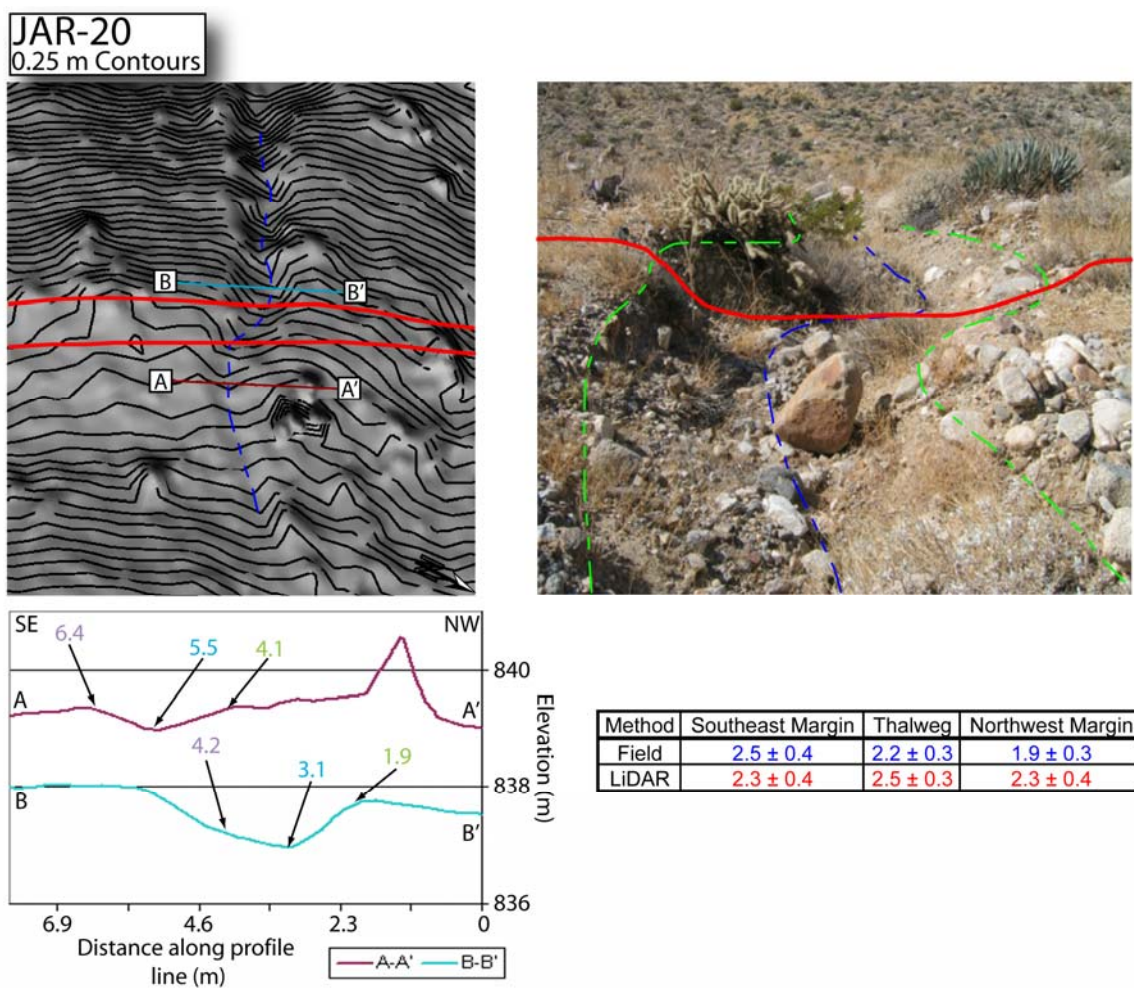


Figure 20. Annotated topographic map and field photograph of offset channel JAR-20 (UTM zone 11, 552798 E, 3700271 N) along Jackass Ridge. Displacements of the channel margins and thalweg were estimated in the field and from LiDAR DEM's. The measurements are shown in the table.

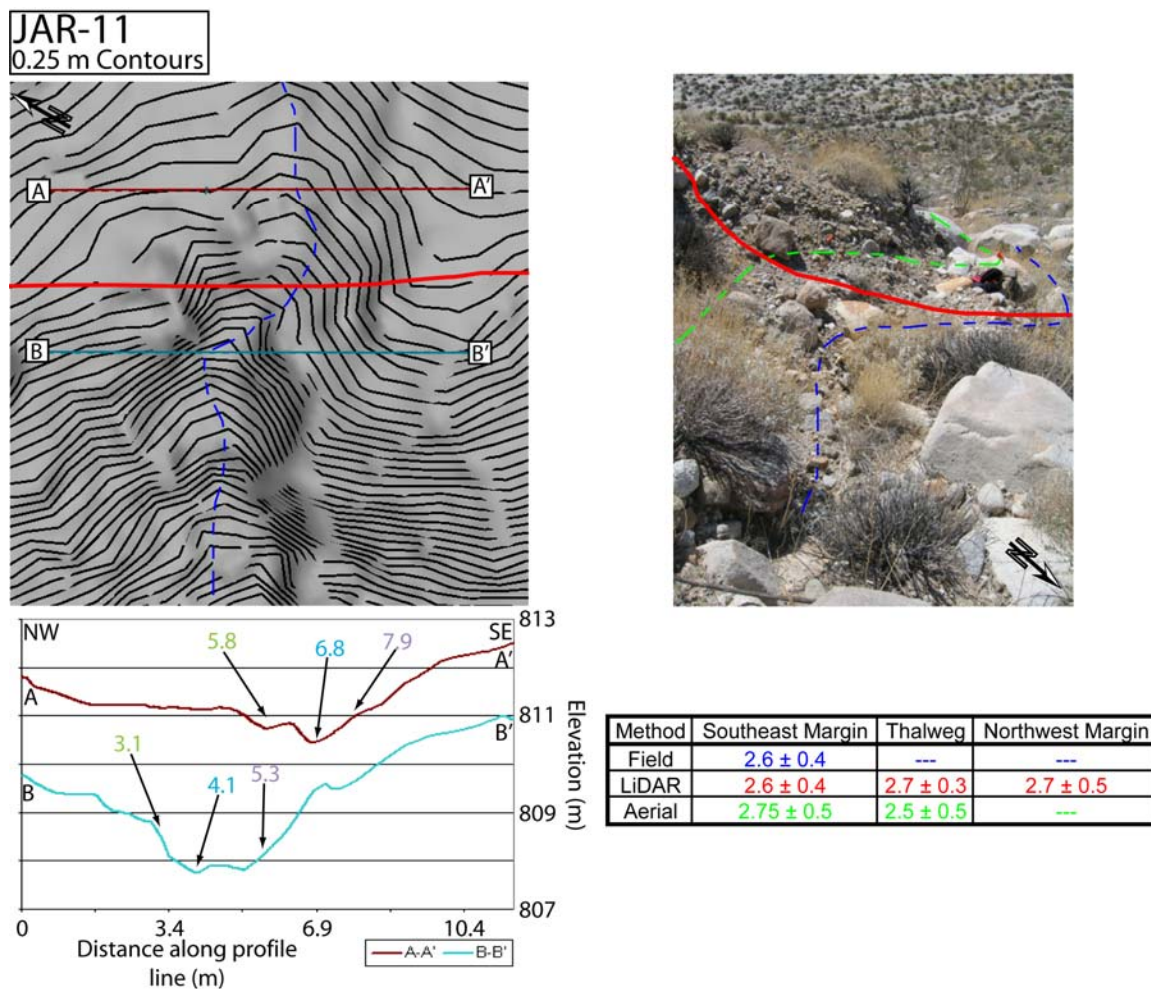


Figure 21. Interpreted field photograph and LiDAR generated topographic map and cross-sections for offset channel JAR-11 (UTM zone 11, 553133 E, 3700059 N) along Jackass Ridge. The table displays displacements for the three channel features estimated from field observations, LiDAR DEM's and aerial photography.

the 15 localities that was also assessed with aerial photography, yielding similar results to those obtained from field investigations - around 2.75 ± 0.5 m of slip for the same margin. The northwest margin was recognized in the field; however it was not measurable due to the size of alluvium that comprises it. With the LiDAR data on the other hand, I was able to estimate slip for the northwest margin of 2.4 ± 0.5 m. Slip estimates at this location are very close to the section average and interpreted to be slip during the MRE.

JAR-5

A nearly perpendicular rill crosses the fault and is offset an average of 2.3 m (Figure 22). Field measurements are substantially lower than LiDAR estimates, with field observations recording about 2 m of slip for the southeast margin and thalweg. LiDAR estimates are 60-80 cm higher at 2.7 ± 0.3 m and 2.8 ± 0.4 m for the same aforementioned features. From aerial photography, the slip estimate for the southeast margin falls between estimates made in the field and by LiDAR data, suggesting about 2.5 m of slip. The scarp is well-preserved; however, some erosion has rounded the corners forcing projection of the channel features to the fault trace, and I attribute the discrepancy between the methods to be from this affect. The estimate made by LiDAR, which is only 20 cm higher than the section average, is inferred to be a reasonable estimate for slip during the MRE at this site.

ROCKHOUSE CANYON AND ROCKHOUSE RIDGE

The Clark fault through Rockhouse Canyon and along Rockhouse Ridge is defined by as a 5-km-long continuous strand with abundant small- and large-scale offset geomorphic features (Figure 23). The surface expression of the fault is very well defined through the young alluvium in southern Rockhouse Canyon and produces a pronounced mole track along

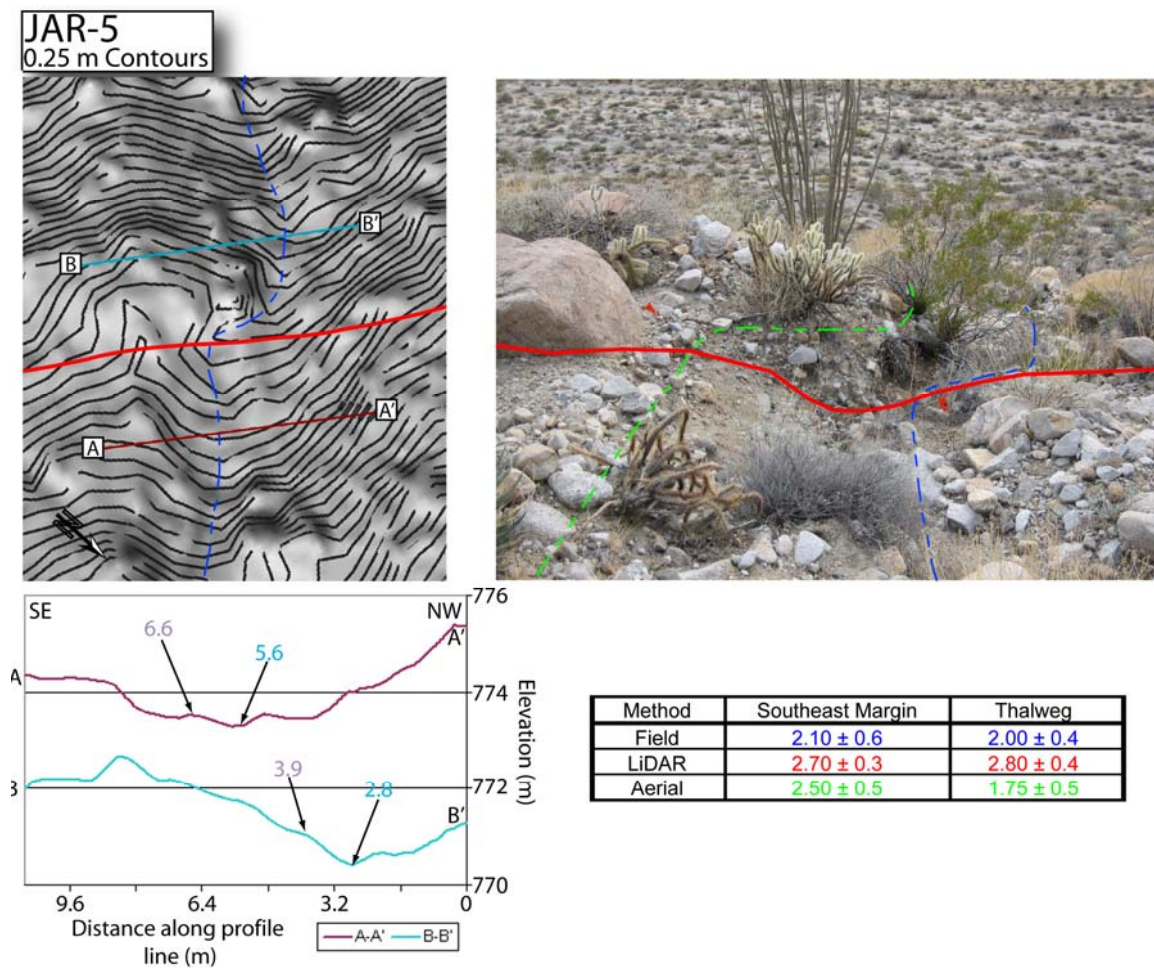


Figure 22. Topographic map, channel cross-sections, and interpreted field photograph of offset rill JAR-5 (UTM zone 11, 553375 E, 3699925 N) along Jackass Ridge. Offsets of the southeast margin and thalweg were estimated in the field and subsequently with the LiDAR data and aerial photography. The results are presented in the table.

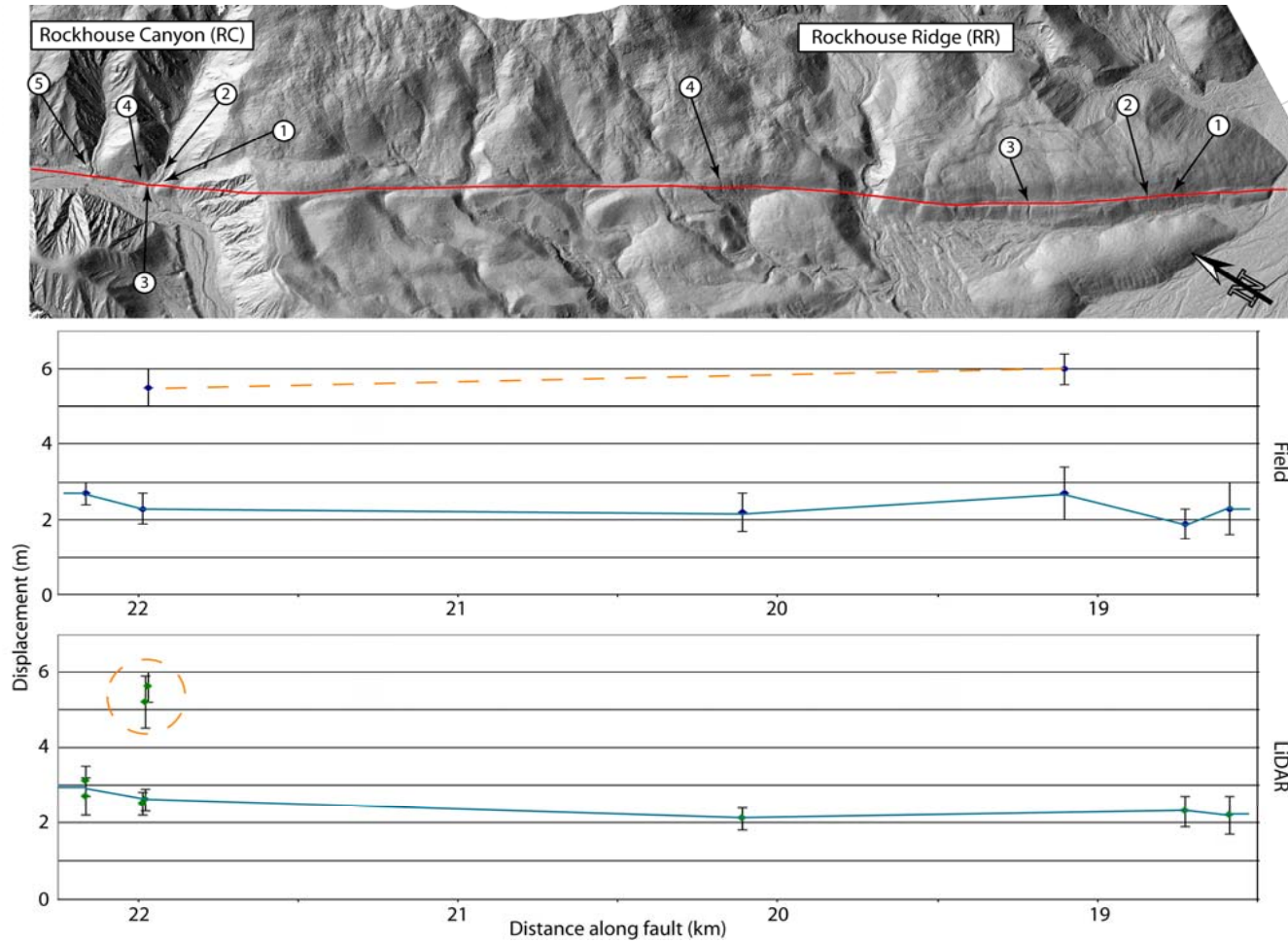


Figure 23. LiDAR DEM and slip distribution graphs for Rockhouse Canyon (RC) and Rockhouse Ridge (RR) with offset localities denoted on the DEM's. As before, estimates connected by blue lines are inferred to be slip in the MRE while orange connect slip accrued from the past two events.

the length of Rockhouse Ridge. Within Rockhouse Canyon, two prominent drainages are present that cross the fault and exhibit displaced bars and channels that are interpreted to represent single and multiple events. Along with slip during the MRE, reconstruction of drainages incised along Rockhouse Ridge suggests that some channels are offset in excess of 1 km.

Along this section, the Clark fault generally juxtaposes Cretaceous tonalite against Quaternary Bautista Formation. As a result along Rockhouse Ridge, rill formation is extremely rare, with the majority of water transportation occurring in large, well developed washes and drainages that incise into the bedrock. Single and double-event offsets are sparse in this section due to this reason, with only 11 measured features at 8 separate sites along the entire 5-km stretch (Tables 5a and 5b). Where available, slip estimates for the MRE dwindle from ~2.7 m in the north to ~1.9 m in the south with an average of about 2.4 m (Figure 24). Although slip measurements are sparse, the qualities range from fair to good, indicating that the estimates can be used with a fair amount of confidence. A higher estimated slip value of ~ 5.3 m measured for one drainage is slightly more than double the MRE and is assumed to be slip from the past two events. Similar to the other sections, this average is based on only a few slip estimates, two with LiDAR data and one from the field observations, and may not accurately represent the true amount of slip. The multi-event offsets, some in excess of 1 km, will be discussed later in this thesis.

RC-5

In southern Rockhouse Canyon, a very coarse alluvium channel containing boulders larger than a few meters across and its associated debris fan are offset 2.7 ± 0.3 m from the

Table 5. (a) Rockhouse Canyon (RC). (b) Rockhouse Ridge (RR)

Rockhouse Canyon (RC)											
#	Location	Feature	Longitude	Latitude	Distance along fault	Meters ^a	±	Confidence	Meters ^b	±	Confidence
1	RH-1	BC	558158	3696972	21.91				22.1	1.5	6.5
2	RH-2	BC	558112	3697001	21.97				21.9	1.6	6.5
3		BC				5.5	0.5	7.5	5.6	0.4	7.5
4	RH-3	TH	558104	3697005	21.98				2.6	0.3	7
5		TH							5.2	0.7	6.5
6	RH-4	BC	558095	3697010	21.99	2.3	0.4	7	2.5	0.3	7
7	RH-5	SE	557954	3697119	22.16	2.7	0.3	7.5	3.1	0.4	7.5
8		TH							2.7	0.5	7.5

Rockhouse Ridge (RR)											
#	Location	Feature	Longitude	Latitude	Distance along fault	Meters ^a	±	Confidence	Meters ^b	±	Confidence
1	RR-1	TH	561085	3695356	18.58	2.3	0.7	5.75	2.2	0.5	5.5
2	RR-2	TH	560961	3695425	18.73	1.9	0.4	6.75	2.3	0.4	6.5
3	RR-3	TH	560613	3695583	19.10	6	0.4	6.25			
4		TH			19.10	2.7	0.7	5.5			
5	RR-4	TH	559754	3696113	20.11	2.2	0.5	7.5	2.1	0.3	7.5

Note: ^a denotes measurements in the field.

^b denotes measurements made by LiDAR.

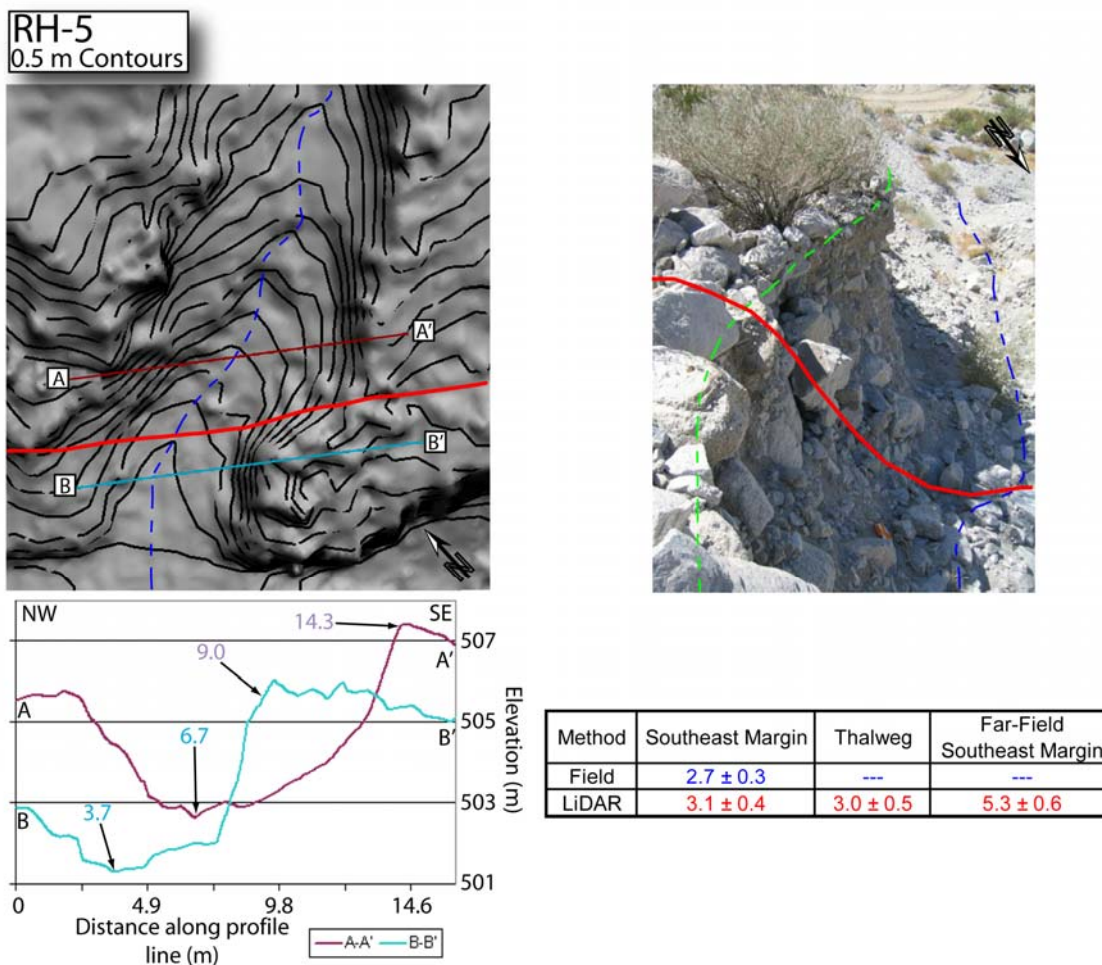


Figure 24. LiDAR generated topographic map and channel cross-section, as well as annotated field photography of offset drainage RH-5 (UTM zone 11, 557954 E, 3697119 N) in Rockhouse Canyon. As before, cross-section lines were taken parallel to the fault trace. Displacements of the thalweg, in the near- and far-field, and the southeast margin are shown in the table.

MRE, as estimated from field measurements (Figure 24). Estimates made by LiDAR are similar to the field measurements with 2.7 ± 0.5 m for the thalweg and 3.1 ± 0.4 m for the southeast margin. The channel is nearly perpendicular to the trace of the fault with deeply incised channel margins; however the scarp is not nearly as sharp as previous sites. This may be due to the unconsolidated nature of the sediment comprising the channel margin distributing slip rather than slip occurring on a single plane or collapse of the channel wall at the fault trace. If either of these are the case, then it is possible to assume that the estimated slip values may be the maximum with true slip likely less than recorded.

RR-4

In general, rill formation is rare along Rockhouse Ridge due to the lithology of the juxtaposed rocks. One exception is RR-4 where a small rill crosses the fault in the colluvium generated by a very prominent mole track/scarp of a beheaded channel. The rill has incised into young coarse grained alluvium, with boulders in excess of 2 m, which makes projection difficult into the fault trace. Both margins were recognized in the field and by LiDAR, but offset was un-measurable due to alluvium size. However, the thalweg was recognized and slip was estimated based on offset on this feature in the field at 2.2 ± 0.5 m, and 2.1 ± 0.3 by LiDAR (Figure 25). These values are similar for the few rills observed in the southern area of this section ranging between 2.3 to 1.9 m, which is attributed to the MRE (Table 5b).

LUTE RIDGE

Lute Ridge is the farthest south section included in this work, and is only 1.7 km from the mapped termination of the Clark fault where the fault splays into the San Felipe Hills (Janecke et al., 2004; Sanders et al., 1986) (Figure 26). The surface trace of the fault is

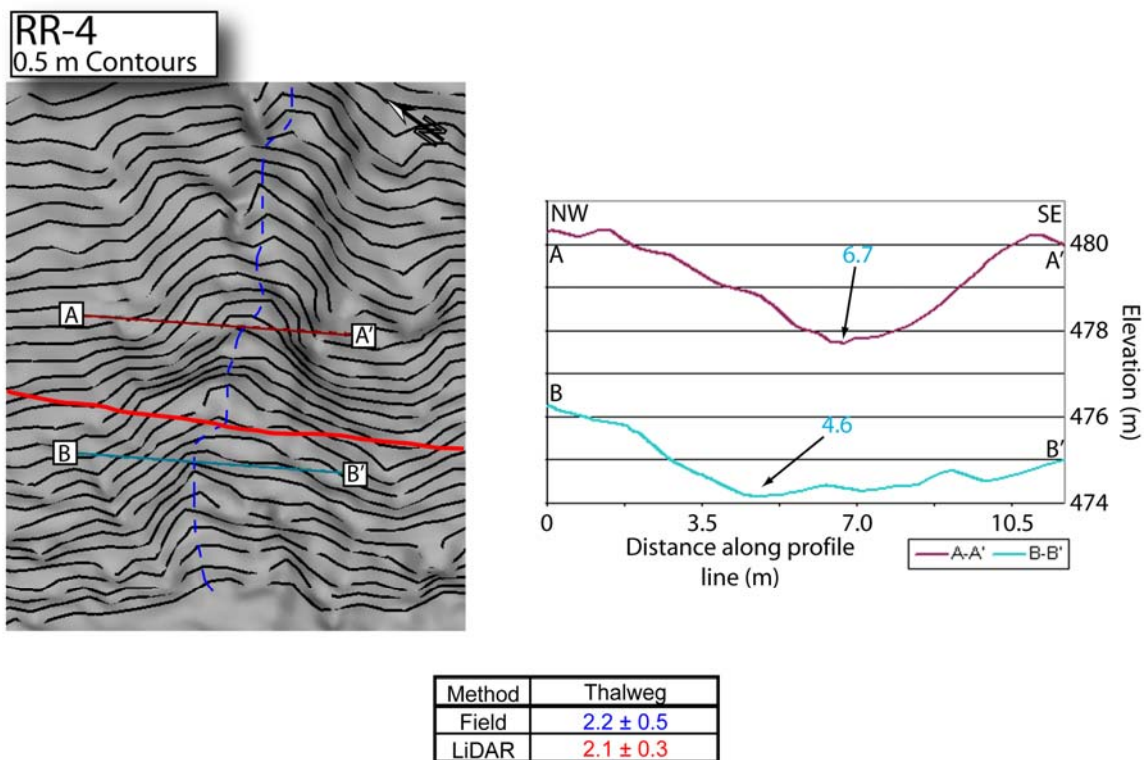


Figure 25. Topographic map and channel cross-section generated from the LiDAR DEM's of offset rill RR-4 (UTM zone 11, 559754 E, 3696113 N) along Rockhouse Ridge. Displacement was estimated from the LiDAR DEM's and in the field for the thalweg only and displayed in the table.

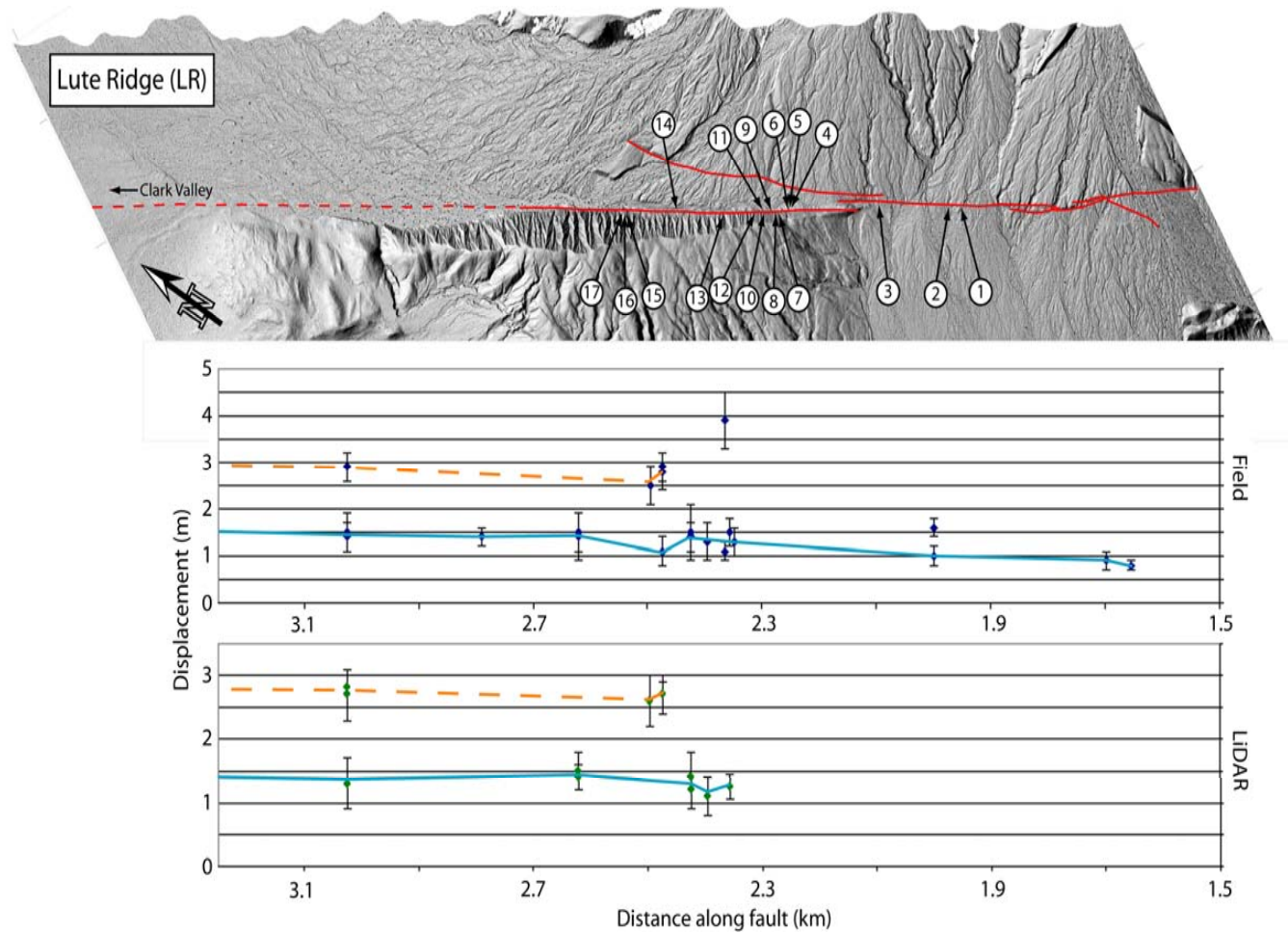


Figure 26. Annotated LiDAR DEM of Lute Ridge (LR) with offset channel sites. Slip distribution graphs are presented for offsets estimated from the LiDAR data and in the field. Blue and orange lines connect displacement estimates from the MRE and past two events, respectively.

discontinuous, with several splays cropping out in the south. Field investigation of these splays shows that they have a component of normal slip. The main strand is mapped at the northeast base of the steep side of Lute Ridge, and where slip was estimated for the last few events. The unconsolidated alluvium of the fan provides an excellent material in which to develop a high drainage density across the fault (many rills). However, due to the loose nature of this fan material, many rills apparently post date the last event and have washed away evidence of that event, showing little to no offset. Slip measurements were estimated on well developed, deeply incised rills that are nearly perpendicular to the fault trace.

In all, 17 offset rills were observed with 23 measured features totaling 35 estimates of slip (Table 6). Distinct clusters are observed around two slip values which are inferred to be slip from the last two events, with the lesser value to be slip during the MRE (Figure 26). Average slip estimates for the MRE are ~ 1.3 m in this area, but range from about 1.5 m in the northwest and decrease to less than a meter toward the mapped southern termination of the fault. On 11 of the 35 estimates, slip is estimated to be almost double the MRE at ~2.7 m, which is attributed to the past two events. Although only one offset was measurement at ~3.9 m, it is attributed to slip from the past three events, assuming each event produces similar amounts of displacement.

LR-16 and 17

Two small rills are generally perpendicular to a prominent fault controlled bench and have been offset during the past two events. LR-16 is a small rill, only about 40 cm wide, with well developed channel morphology. The thalweg was easily recognized, and is offset by about 1.5 ± 0.4 m based on field measurements. In contrast, the LiDAR DEM suggests

Table 6. Lute Ridge Displacement Data (LR)

#	Location	Feature	Longitude	Latitude	Distance along fault	Meters ^a	±	Confidence	Meters ^b	±	Confidence
1	LR-1	TH	575130	3685868	1.65	0.8	0.1	6.5			
2	LR-2	TH	575092	3685891	1.70	0.9	0.2	7			
3	LR-3	TH	574789	3686002	2.00	1	0.2	7			
4	LR-4	TH	574498	3686195	2.35	1.3	0.3	6.75			
5	LR-5	TH	574490	3686201	2.36	1.5	0.3	7	1.25	0.2	6.5
6	LR-6	TH	574486	3686208	2.36	3.9	0.6	6			
7		TH				1.1	0.2	6			
8	LR-7	TH	574456	3686220	2.40	1.3	0.4	6	1.1	0.3	6.5
9	LR-8	TH	574435	3686239	2.42	1.4	0.3	7.25	1.2	0.3	6.5
10	LR-9	TH	574428	3686230	2.42	1.5	0.6		1.4	0.4	7
11	LR-10	TH	574390	3686263	2.47	2.8	0.4	8.5	2.9	0.3	7.5
12		SE				2.9	0.3	8.5	2.7	0.2	7.5
13		NW							2.8	0.3	7.5
14	LR-11	FA	574390	3686263	2.47	1.1	0.3	6.5			
15	LR-12	TH	574368	3686269	2.50	2.5	0.4	7	2.6	0.4	7
16	LR-13	TH	574258	3686332	2.62	1.5	0.4	7.5	1.5	0.2	7.5
17		SE				1.4	0.5	7.5	1.4	0.3	7.5
18	LR-14	TH	574103	3686407	2.79	1.4	0.2	6			
19	LR-15	TH	573905	3686536	3.03	1.4	0.3	6.5			
20	LR-16	TH	573905	3686536	3.03	1.5	0.4	7.5	1.1	0.4	7.5
21	LR-17	TH	573905	3686536	3.03	2.9	0.3	8	2.9	0.3	7.5
22		SE				2.7	0.5	8	2.7	0.4	7.5

Note: ^a denotes measurements in the field.

^b denotes measurements made by LiDAR.

only about 1.1 ± 0.4 m, which is interpreted to be close to the lower limit of what can be measured with LiDAR (Figure 27). LR-17 is a slightly larger, more developed rill which is offset more than just by the MRE. Offsets were estimated in the field and by LiDAR for the southeast channel margin, as well as the thalweg, and indicate 2.7 ± 0.4 m and 2.9 ± 0.3 m of displacement, respectively (Figure 27). These values are close to double the MRE and likely represent slip during the past two surface rupturing events along this strand.

LR-13

A deeply incised rill crosses nearly perpendicular to the fault and is deflected dextrally ~ 1.5 m (Figure 28). The trace of the fault is difficult to locate, but based on adjacent geomorphic features, such as a subtle break in slope a few meters to the north, I am confident with the projection of the fault and this estimate of offset. The fault at this locality is lacking a distinctive fresh scarp, which is observed at other locations along Lute ridge. However, this is attributed to erosion of the loose gravel rather than the result of displacement in an older event. Channel morphology is well preserved within the rocky channel allowing for offset estimates of the southeast margin and the thalweg. Estimates made from LiDAR and in the field yield similar results, with the southeast margin recording ~ 1.4 m of slip and the thalweg recording about 1.5 m.

LR-10

A well developed rill crosses the fault, with offset of channel features averaging ~ 2.8 m of slip. The fault trace is discontinuous along this section; however, after careful field analysis, the main strand was located with confidence. In the field two of the three channel features, the southeast margin and the thalweg, were recognizable and displacement

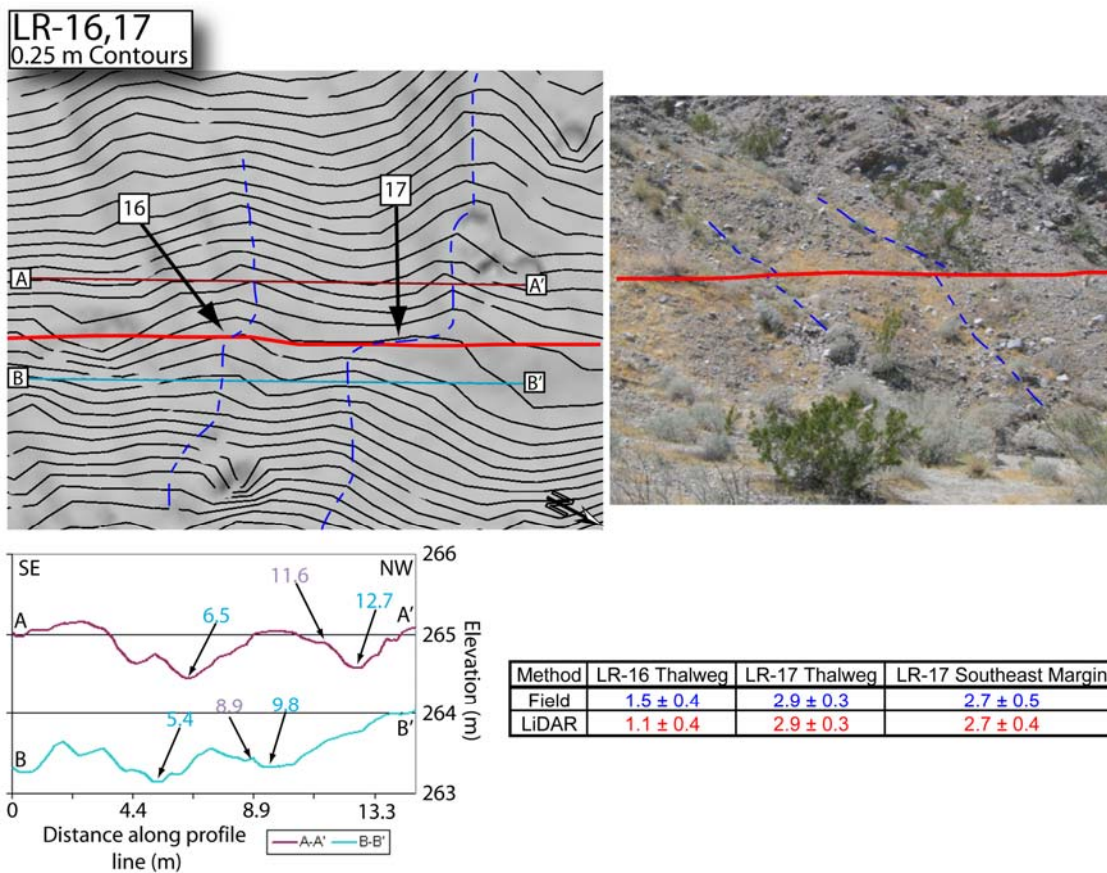


Figure 27. Interpreted field photograph and topographic map of offset rills LR-16 and LR-17 (UTM zone 11, 573905 E, 3686536 N). LR-16 expresses roughly half the displacement of LR-17, suggesting that the smaller rill, LR-16, was only displaced in the most recent event, whereas the larger rill, LR-17, was displaced during the past two events. Displacements of both rills are shown in the table.

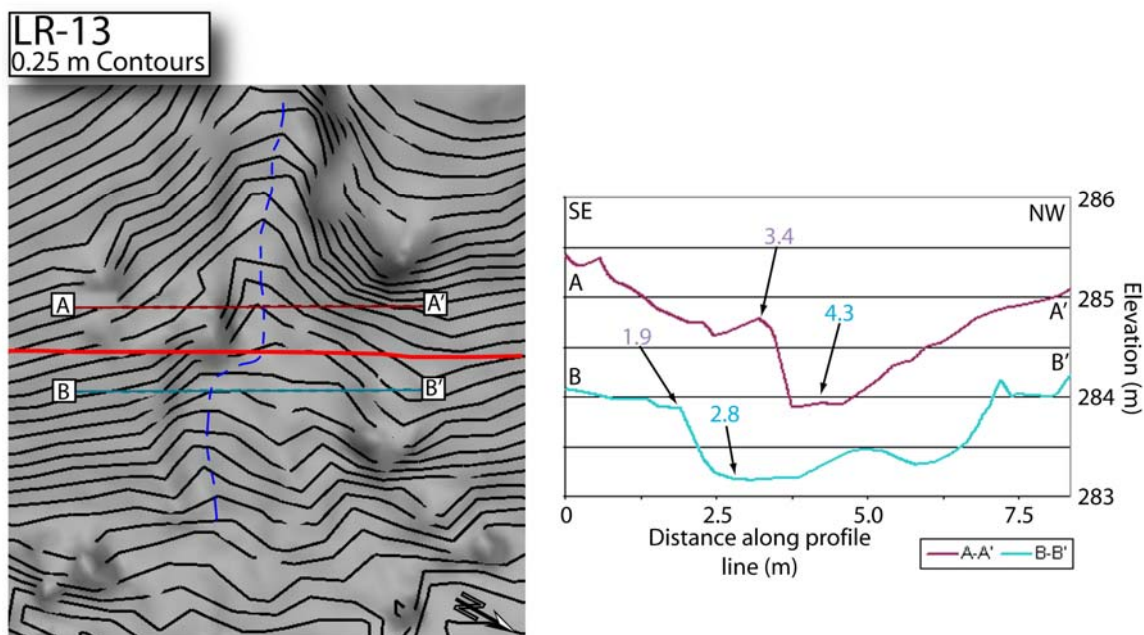


Figure 28. LiDAR topographic map and channel cross-sections of a displaced rill at LR-13 (UTM zone 11, 574258 E, 3686332 N). The southeast margin and thalweg are displaced similarly and interpreted to be the result of the MRE.

measured, recording 2.9 ± 0.3 and 2.8 ± 0.4 m of slip, respectively (Figure 29). Using LiDAR data, similar values were estimated for all three offset features, averaging ~ 2.8 m of slip. At this location, slip in the MRE was not recognized; however, from observations for the rest of this section, this value is believed to record the amount of slip for the past two events.

LATE HOLOCENE MULTI-EVENT OFFSETS

In some locations of the study area there are larger, multi-event offsets recorded in the tectonic geomorphology. These multi-event offsets range from the ten meter scale, like those observed where Dry Wash crosses the fault, up to the kilometer scale for both Rockhouse Ridge and Lute Ridge. These offset measurements, when combined with age estimates, can conceivably resolve the slip rate for the late Pleistocene through Holocene time along this section of fault. In this project, however, I focus and present my estimates of the offsets, which will provide the basis for slip rate determinations in the near future by other students.

DW-JAR

Where Dry Wash crosses the fault is evidence for slip from the MRE as well as for a larger multi-event offset on the northwestern side of the active wash. During field investigations, two bar crests were recognized on the southwestern side of the fault (Figure 30a). Initially the bar crest on the north side of the fault was realign with the most northwestern bar on the southern side, requiring about 28 m of slip. However, using the LiDAR-based imagery, it was noticed that 28 m of reconstruction would result in the ridge nose being juxtaposed into the channel (Figure 30c). On the other hand, reconstructing the

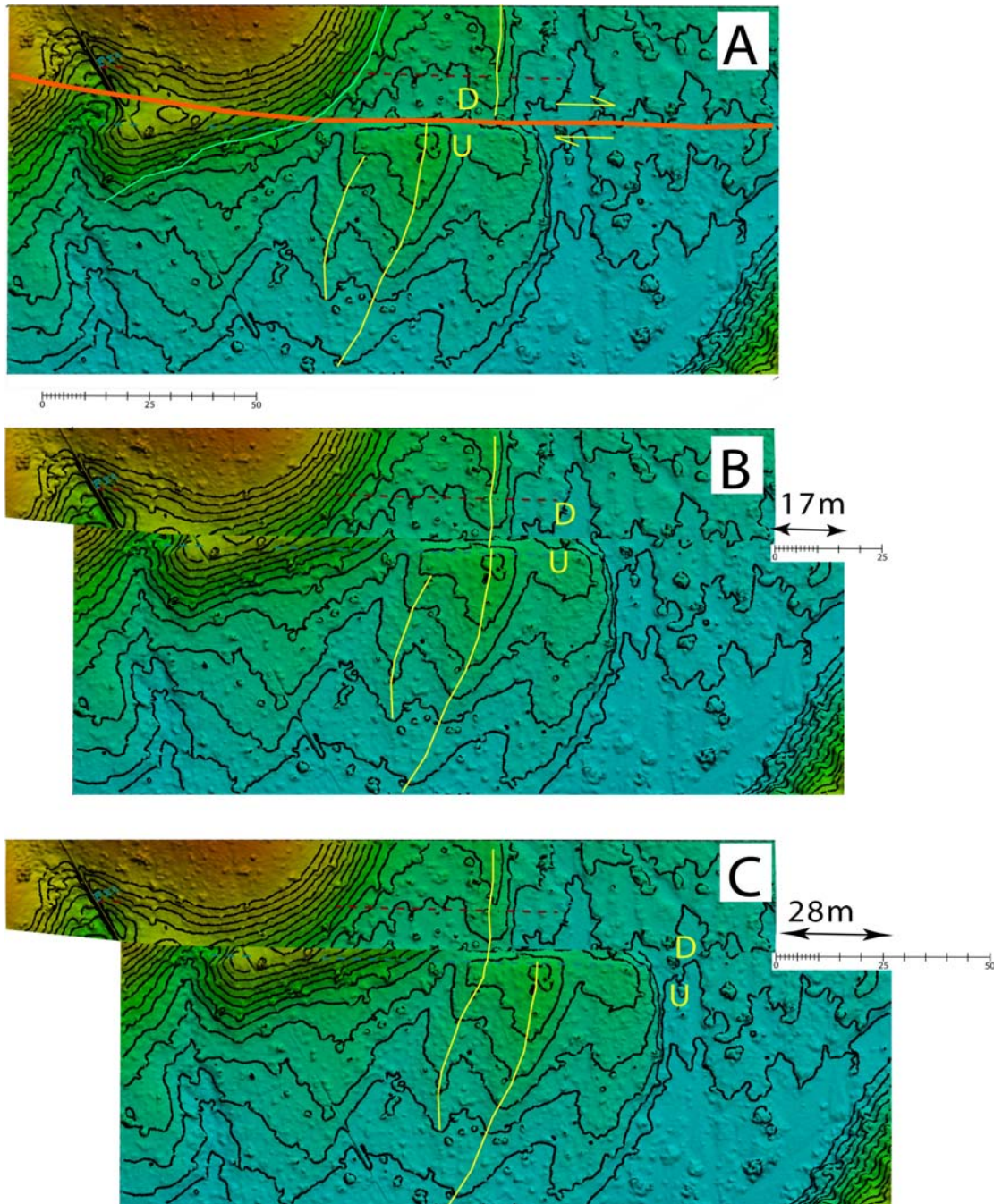


Figure 30. Detailed topographic map of displaced bars and swales where dry wash crosses the trace of the Clark fault (UTM zone 11, 552086 E, 3700723 N). Lines represent bar crests on either side of the fault with north to the top left of the figures. (a) Present day; (b) A 17 m reconstruction realigns the southern bar on the southwest side of the fault with the bar crest on the northern side, as well as the ridge nose to the north; (c) A 28 m reconstruction realigns the northern bar crest on the southwest side with the bar crest on the north side of the fault. This reconstruction causes the ridge nose to protrude into the channel.

bar crest on the north side of the fault with the southeastern bar crest on the south side realigns the hill nose close to its original configuration (Figure 30b). This reconstruction requires ~17 m of slip since the formation of the bar crest, as well as since the margin of the channel was cut. Combined with the inferred slip from the MRE, I suggest that this offset is the result of the last 6-7 events, assuming that the fault ruptures with similar amounts of slip in each event.

Rockhouse Ridge

Along Rockhouse Ridge, is a series of deflected and beheaded channels that are offset from their original source areas. The amounts of displacement are estimated from reconstructing the beheaded channel to the active source channel, taking into account that some channel deflection occurred before channel capture. Based on LiDAR imagery and field investigations, it is estimated that at least 540 m of slip has accrued since the last time beheaded channel 1 was in front of the active drainage (I), and 150 m since beheaded channel 2 was in that position (Figure 31).

In the southern portion of Rockhouse Ridge, from the tectonic geomorphology it can be inferred that the beheaded channels possibly offset from a farther south drainage than the currently active channel (I). Very little evidence is recognizable for a reconstruction as large as 1 km, but rounding and warping of the channel margins suggests that it is possible. A larger reconstruction of beheaded channel 4 could realign that channel with active channel IV (Figure 32a). However, the beheaded channel is small in size compared to the more developed source channels, which is attributed in part to the amount of time since its initial formation. A more likely reconstruction requires only 540 m of offset, realigning the

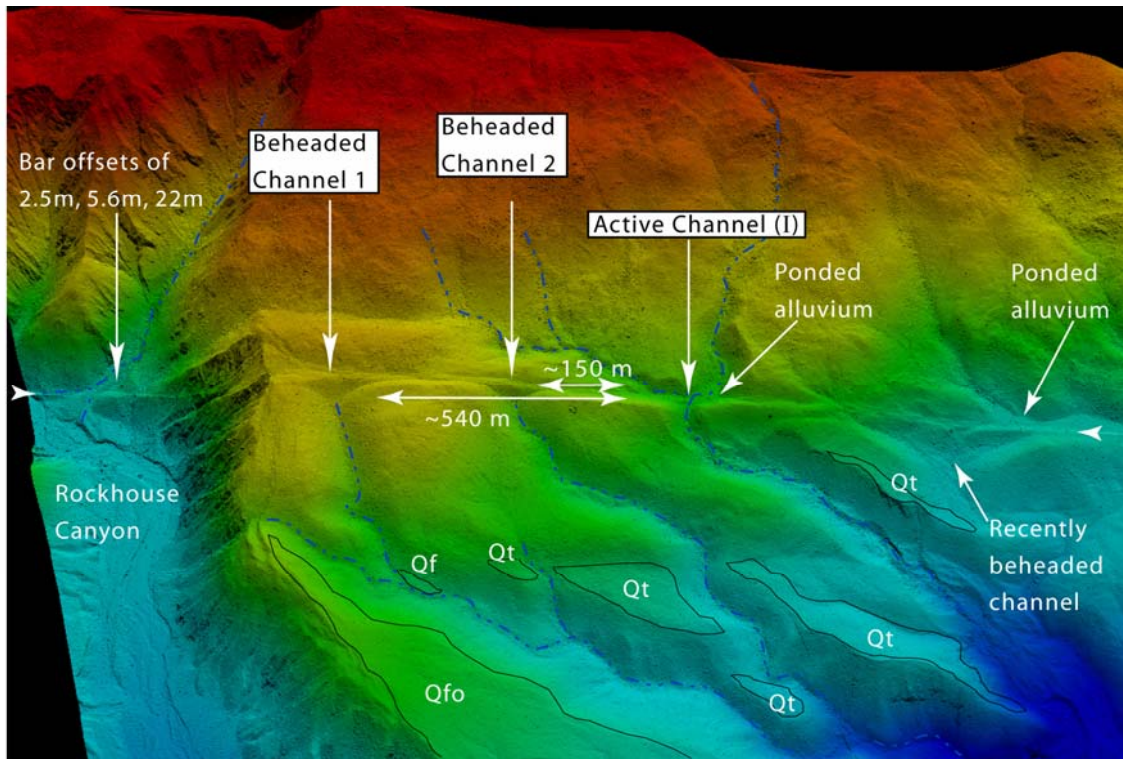


Figure 31. Interpreted oblique LiDAR DEM of south Rockhouse Canyon and north Rockhouse Ridge. Beheaded channels (1 and 2) are laterally displaced about 540 m and 150 m, respectively, from the active channel (I). Offsets were estimated based on reconstructions to the source location assuming some bending and warping has occurred since beheading (Figures 32a and b)

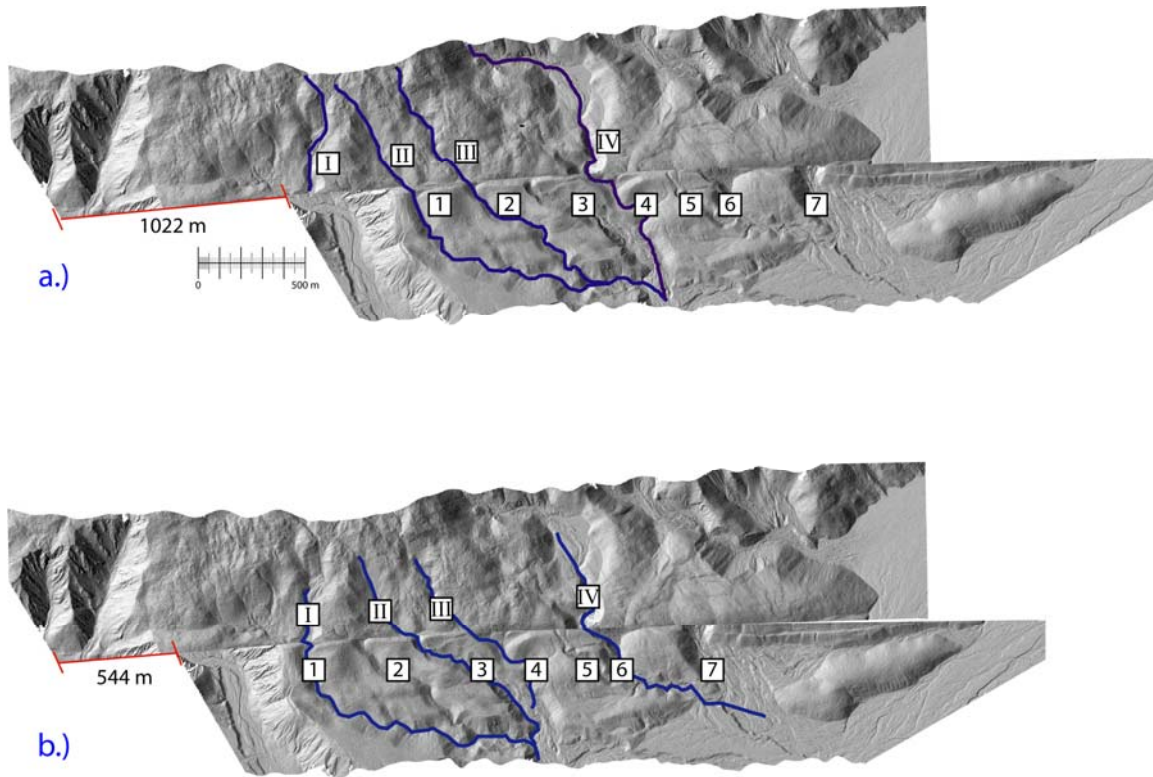


Figure 32. Large scale reconstruction of Rockhouse Ridge. (a) 1 km reconstruction that realigns source drainages II, III, and IV with offset drainages 1, 2, and 4, respectively. Some source drainages (II and III) appear fairly young and this reconstruction may not be correct. (b) 540 km reconstruction realigning source drainages I, II, II, and IV with offset drainages 1, 3, 4, and 6. This reconstruction seems more reasonable since the initiation of the drainages; however, more work is needed to resolve the exact reconstruction.

beheaded channel 4 with active channel 3, also a fairly young channel based on its size (Figure 32b).

Lute Ridge

Lute ridge is inferred to be the offset toe of an offset alluvial fan. However, the location of the source drainage has not been well established. Three large washes drain from the Santa Rosa Mountains to the northeast, with any of them large enough to create an alluvial fan of this size. I assume that little to no deformation has distorted the original fan shape, and based on this, projected the location of the original fan apex by drawing lines perpendicular to the fan contours (Figure 33). Moreover, projection of the fan apex suggest that it may have emanated from any one of three potential drainage sources, drainage A, B, and C. When Lute Ridge is reconstructed in front of these three possible drainage sources, a range of slip values of between 400 m to about 2 km can be resolved. The largest slip reconstruction (2 km) is highly unlikely, although not entirely out of the question. A more likely scenario is to reconstruct the fan about 750 m so that it lies in front of both drainages A and B, with the majority of the material derived from the larger drainage (A). To fully assess the exact reconstruction of the alluvial fan would require a detailed provenance study of the alluvium comprising the alluvial fan, which is beyond the scope of this project.

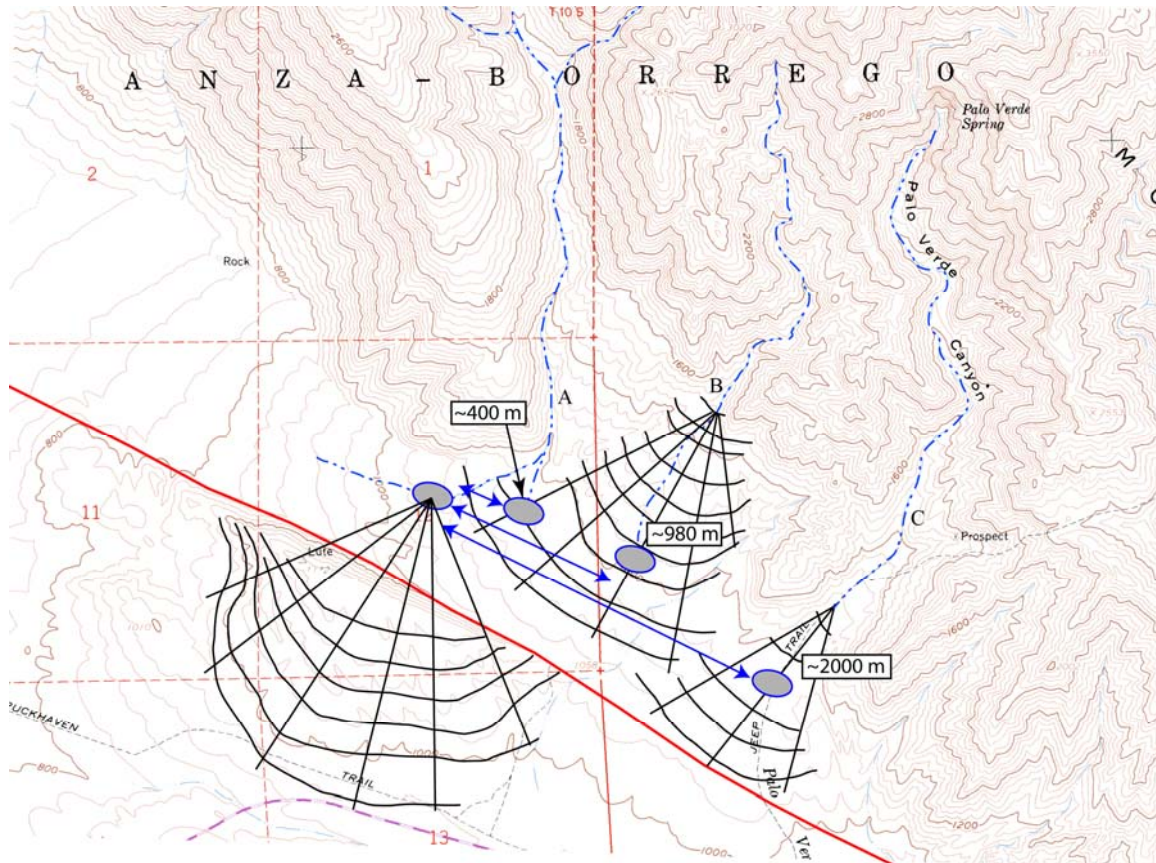


Figure 33. Interpreted topographic map of Lute Ridge in Clark Valley. The projection of the fan apex can be reconstructed too three prominent source drainages (A, B, and C). The farthest reconstruction (C), although not out of the question, is the most unlikely. A more likely scenario realigns the offset fan of Lute Ridge to both drainage A and B requiring between 400 to 980 m of displacement.

CHAPTER 4

DISCUSSION

The studied geomorphic features presented in the previous section suggest that the most recent surface rupturing event to occur along the 55 km section of the Clark fault from Anza Valley to the southern termination in Clark Valley produced an average of ~ 2.7 m of right-lateral slip, with maximum slip reaching close to 4 m near Anza (Figure 7). Although based on fewer estimates, average slip for the past two events was measured to be ~ 4.9 m for the same 55 km section, suggesting that the penultimate event was roughly 75% of the size of the MRE. I also observed consistent variations in the spatial distribution of the displacements as slip decreases from about 4 m at Anza, down to less than a meter near the mapped southern termination of the fault at Lute Ridge. To the north of Anza, the expression of the Clark fault continues for another 60-65 km to the Hemet step-over, although no slip information was collected during this project from that section of fault.

In the following sections, based on the observed slip information discussed above, the seismic moment and magnitude for the most recent event will be estimated, as well as the age of the MRE. However, before proceeding some assumptions are made about the rupture behavior, length, and slip distribution to the north of Anza. The observed slip distribution can also be combined with the recent paleoseismic work at Hog Lake, from which an approximate slip rate can be calculated for the Clark fault.

RUPTURE LENGTH

The Clark strand of the San Jacinto fault system totals about 120 km in length. However, only the southern most 55 km section was studied for slip distribution, leaving slip during the MRE for the northern 65 km unresolved. From the slip distribution in the south, there is a noticeable decrease in slip estimates from Anza Valley to the southern mapped termination of the fault (Figure 7). To the north of Anza Valley, however, the termination of the surface rupture caused by the MRE is not well constrained. Nevertheless, several possible scenarios can still assumed for rupture behavior north of the Anza gap.

In 1899 and 1918, two relatively large earthquakes (M_s 6.4 (Abe, 1988) and M_s 6.9 (Ellsworth, 1990) occurred near the town of San Jacinto and Hemet on the bounding faults of a releasing step-over that created the San Jacinto Valley. Rasmussen (1981) suggests that the earthquake of December 25, 1899, occurred on the southwest bounding fault of the step-over and northern extension of the Clark fault, the Casa Loma fault. Claypole (1900) was the first geologist to investigate this “Christmas Day” earthquake in 1899, from which he observed secondary cracking within the vicinity of San Jacinto. However, no direct evidence for surface rupture was documented farther to the south. On the other hand, paleoseismic work on the Casa Loma fault presents evidence that fractures do break to the present ground surface, suggesting a historic rupture (Rasmussen, 1981; 1982).

The earthquake of April 21, 1918 is believed to have occurred on the northeast bounding fault of the step-over, the Claremont fault (Dozer, 1992). Within weeks after the earthquake, Townley (1918) and Rolfe and Strong (1918) observed cracking parallel to the ridgelines at the entrance to Blackburn Canyon, about 12 km southeast of Hemet. However, after careful examination, these cracks are believed to be from slumping and landslides rather

then any significant surface rupture. They also investigated the possibility for surface rupture farther to the south of Blackburn Canyon at Hog Lake, but only minor cracking was reported (Rolfe and Strong, 1918). From personal communication with the Cahuilla Indians (2005), the cracking observed at Hog Lake was more likely due to liquefaction and a minor landslide than any surface rupture caused by the 1918 earthquake. Furthermore, from recent paleoseismic studies at Hog Lake, the active fault is located in the center of the lake rather than the east side of the lake, where Rolfe and Strong (1918) recorded the cracking.

From the observations of the 1899 and 1918 earthquakes, I suggest a similar rupture pattern to that of the Imperial Valley earthquakes of 1940 and 1979 in which Sieh (1996) proposes a “patch” model for the observed slip. During the 1940 *M7.1* earthquake, slip was measured up to 6 m near the central section of the fault after nucleating with less than a meter of slip along the northern third of the fault. The *M6.6* earthquake of 1979 ruptured only the northern 30 km of the fault with nearly identical slip distribution for that segment as in the earthquake of 1940 (Figure 34a). From this observation, Sieh (1996) inferred that smaller earthquakes nucleate in segments adjacent to stronger sections of the fault, where larger displacements are recorded (Figure 34b). Combining the idea of a “patch” model with the observations of the 1899 and 1918 earthquakes, I can infer a couple of possibilities for rupture behavior north of Anza, based on the slip distribution of the MRE that I infer to the south.

Using the Imperial Valley and the patch model as an analog for the 1899 and 1918 earthquakes, I assume that these are “smaller” earthquakes releasing strain adjacent to the stronger portion of the fault - the Anza seismicity gap. From which, two scenarios are assumed for rupture behavior north of Anza. In the first scenario, scenario A, the slip

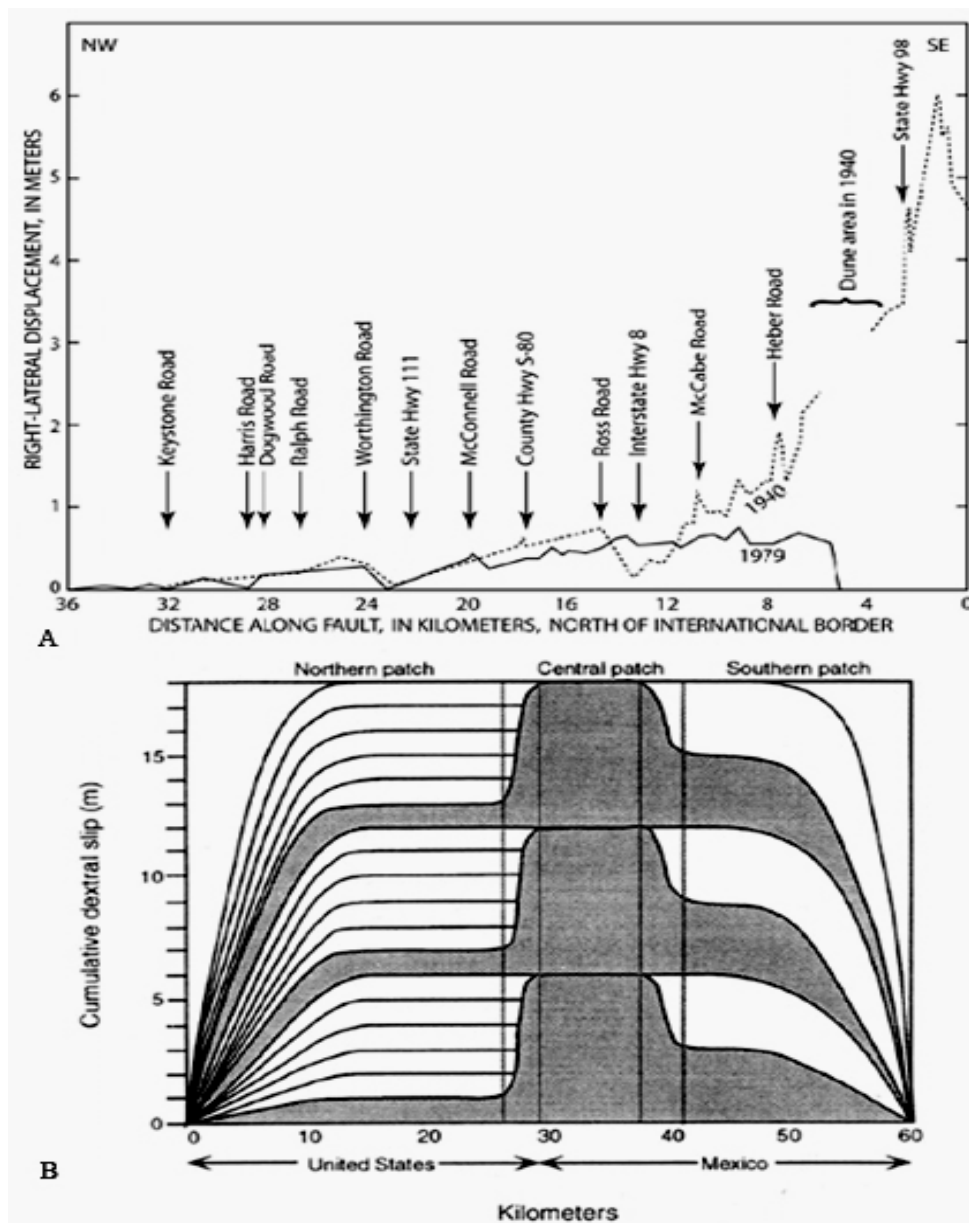


Figure 34. (a) Slip distribution graph for the Imperial Valley earthquakes of 1940 and 1979. The earthquake of 1979 ruptured only the northern 30 km with similar displacement to the earthquake of 1940. (b) Proposed ‘patch’ model for the Imperial Valley fault where slip accumulates from smaller earthquakes to equal the amount of displacement caused by one event in an adjacent stronger part of the fault (Sich, 1996).

distribution is asymmetrical with the rupture terminating just to the north of Anza. This scenario would require only the southern 75 km of the Clark fault to rupture with no surface rupture to the north of the Anza gap (Figure 35a). In the second scenario, scenario B, slip decreases dramatically, but still continues for the entire length of the fault similar to the Imperial Valley earthquake of 1940. This would require the entire 120 km of the Clark fault to rupture, but with lower slip along the northern 55 km (Figure 35b).

Previously it was believed that the 5-km step-over between the Casa Loma and Claremont faults was large enough to stop rupture propagation across it, as demonstrated by numerical modeling experiments (Harris and Day, 1993). More recently, Park et al. (1995) performed a seismic study 7-km to the north of the mapped northern termination of the Casa Loma fault. In that study, they were able to image both the Casa Loma fault and another strand to the east in the sub-surface, between the Casa Loma and Claremont faults. These smaller step-over's are only about 1 to 2 km apart, therefore suggesting a large rupture may be able to propagate across from the Casa Loma to the Claremont or vice versa (although the overall step-over width is still about 5 km). With this new observation, I hypothesize that it is possible to by-pass the Hemet step, thereby rupturing the entire length of the Clark, Casa Loma, and Claremont faults in a single event. An earthquake of this size would rupture more than 150 km of fault at the surface (Scenario C, Figure 35c).

Another possibility is that the fault ruptures in a symmetrical fashion in which slip decreases in the north at the same rate it does to the south, with maximum slip along the Anza seismicity gap. This type of fault behavior would produce a trend similar to a bell curve for the slip distribution, similar to the Superstition Hills earthquake of 1987 (Hudnut et al., 1989; Lindvall et al., 1989; Sharp et al., 1989) and the 1999 Hector Mine earthquake

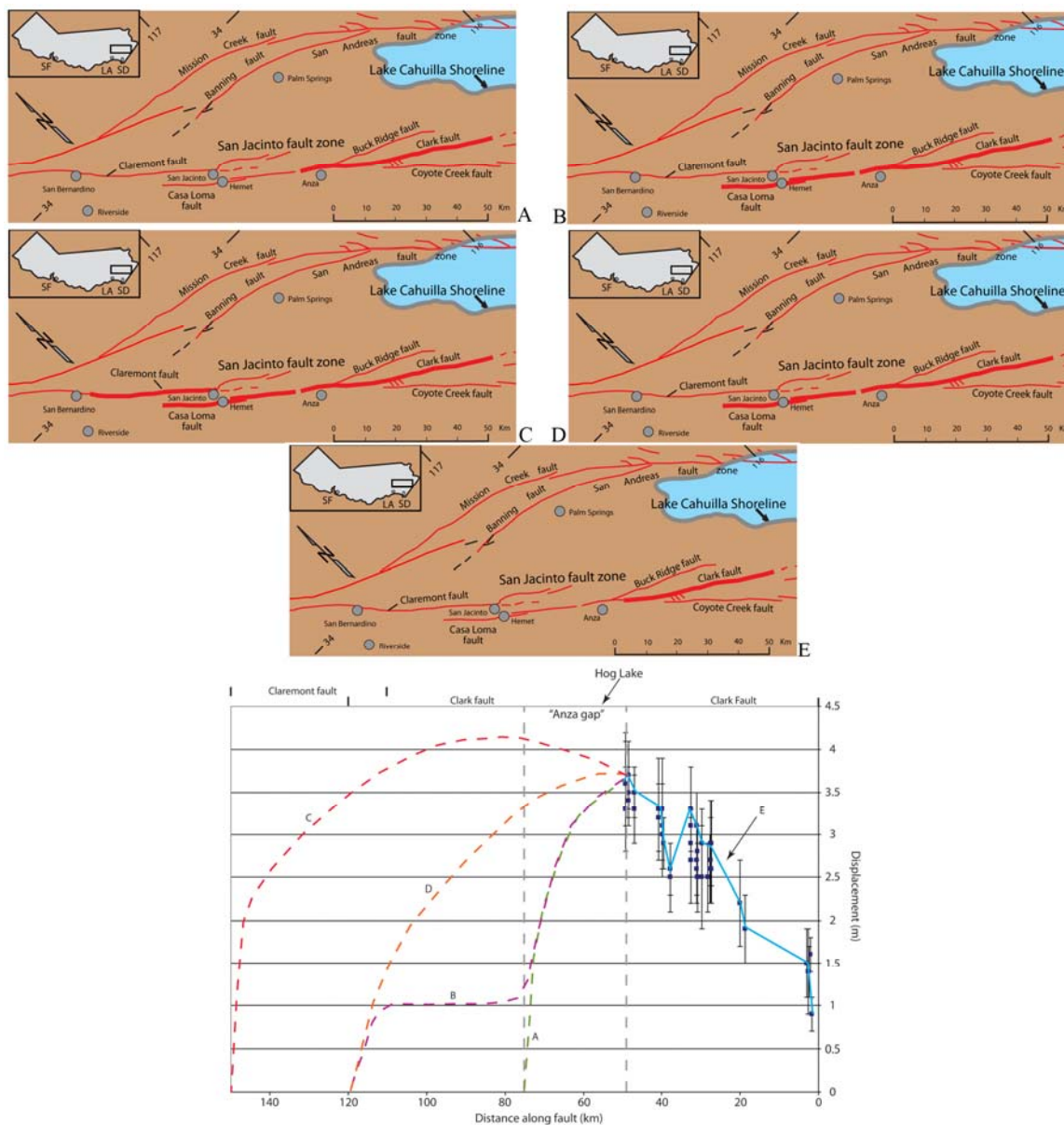


Figure 35. Surface rupture scenarios for the Clark fault. (a) Surface rupture only extends to the northern extent of the Anza gap. (b) Surface rupture extends the entire length of the Clark and Casa Loma fault, but with offsets about a meter for the northern 40 km of the Clark fault. (c) Surface rupture propagates through the Hemet step-over breaking the Claremont, Casa Loma, and Clark fault. (d) Similar to scenario C, surface rupture extends the entire Casa Loma and Clark fault, however slip distribution is symmetrical with maximum slip occurring in the Anza gap. E.) Surface rupture only extends for the 55 km of the Clark fault in which I have recorded slip for the MRE. This is used as an absolute minimum.

(Treiman et al., 2002). Assuming that slip was limited to the Clark fault and its northern extension, the Casa Loma fault, an event of this type would result in a surface rupture of the entire length of the Clark fault, about 120 km, with an average slip estimate similar to that derived for the southern half of the fault (Scenario D, Figure. 35d).

Finally, scenario E was developed as a control model to estimate the minimum magnitude of the most recent event, in which it is assumed that the surface rupture only extended as far north as the last measured offset in Anza Valley. This amount is used as an absolute minimum for the rupture length since the observed slip from the MRE extends the entire 55 km of the southern Clark fault and the 4 m of slip in Anza must require some distance to die off to the north (Figure 35e).

SIZE OF EARTHQUAKE

Using the rupture lengths outlined in the above section, the probable moment magnitude of the MRE along the Clark fault can be estimated from using $M_o = \mu As$ (Brune, 1968) along with $M_w = 0.667 \log M_o - 10.7$ (Hanks and Kanamori, 1979), where M_o is the seismic moment, μ is 3×10^{11} dyn cm⁻² is the rigidity, A is the area of the rupture, and s is the average displacement for a single event. Magnitude estimates for the MRE to range from $M_w = 7.2$ to $M_w = 7.5$, considering each of the various scenarios.

However, specific uncertainties arise while making these estimates, not only for the previously mentioned rupture length, but also due to the depth of the seismogenic zone and slip estimates for the northern section.

When calculating seismic moment and magnitude, it is assumed that most large earthquakes rupture to the base of the maximum depth of microseismicity on the fault

(Sibson, 1984). So to estimate the rupture area used to calculate the seismic moment, I must understand the variations in the depth of microseismicity. The depth of seismicity along strike of the entire San Jacinto fault system varies from fault to fault and even for different sections along a single strand. This is especially the case for the Clark fault where I separate the fault into four different sections based on the depth of seismicity.

For the Claremont fault segment and the Clark-Casa Loma fault southward into the Anza gap, the seismogenic zone is estimated the depth to be around 17 km. Within the 20 km stretch deemed the Anza seismicity gap there is little to no microseismicity; however, from the scattered data, it is estimated to be around 20 km thick. South of the Anza gap and into southern Clark Valley, seismicity shallows again to an average of 17 km depth. From Clark Valley to the southern termination of the fault just south of the Santa Rosa Mountains, is another decrease in the depth of microseismicity to about 14 km (consistent with Sanders, 1989).

The estimated magnitudes listed in Table 7 assume an average of 2.7 m for the entire rupture, except for scenarios B and D. As previously mentioned, slip distribution was recorded for the southern 55 km with no available slip information for the northern 60- 65 km of the Clark fault. Therefore several scenarios were developed to account for the likely distributions of slip in the north in order to calculate a magnitude for the MRE.

In scenario A, I hypothesize slip to terminate just north of the Anza gap, which would result in very little change of the overall estimated slip average; if anything there would be a small increase. In contrast, for scenario B I assume a decrease in slip before achieving a lower value of slip for the rest of the fault. In-turn, this would bias the estimates with a large area of lower slip, decreasing the average slip displacement. Average slip is estimated to

Table 7. Possible Rupture Patterns and Associated Earthquake Magnitudes

Rupture Pattern	Rupture segment	Rupture Length, km	Depth, km	Area, km ²	Slip, m	Mo , 10 ²⁵ dyn cm	M_w
A.) From southern termination to Blackburn Canyon	Claremont fault	0	17	0			
	Casa Loma to Anza (did not rupture)	0	17	0			
	Anza Gap	15	20	300			
	Anza to Clark Valley	35	17	595			
	Clark Valley to Santa Rosa	25	14	350			
Total Rupture		75		1245	2.7	101	7.3
B.) Entire Clark fault with minimal slip north of the Anza gap	Claremont fault	0	17	0			
	Casa Loma to Anza (did not rupture)	35	17	595			
	Anza Gap	20	20	400			
	Anza to Clark Valley	35	17	595			
	Clark Valley to Santa Rosa	25	14	350			
Total Rupture		115		1940	1.5	87	7.3
C.) Entire Clark fault and Claremont fault	Claremont fault	35	17	595			
	Casa Loma to Anza (did not rupture)	35	17	595			
	Anza Gap	20	20	400			
	Anza to Middle of Clark Valley	35	17	595			
	Middle of Clark Valley to Santa Rosa	25	14	350			
Total Rupture		150		2535	3	228	7.5
D.) Entire Clark fault with symmetrical rupture pattern	Claremont fault	0	17	0			
	Casa Loma to Anza (did not rupture)	35	17	595			
	Anza Gap	20	20	400			
	Anza to Middle of Clark Valley	35	17	595			
	Middle of Clark Valley to Santa Rosa	25	14	350			
Total Rupture		115		1940	2.7	157	7.4
E.) Minimum; From the southern termination to Anza	Claremont fault	0	17	0			
	Casa Loma to Anza (did not rupture)	0	17	0			
	Anza Gap	5	20	100			
	Anza to Clark Valley	30	17	510			
	Clark Valley to Santa Rosa	20	14	280			
Total Rupture		55		890	2.7	72	7.2

decrease to about 1.5 m; however, it is possible that slip could in fact be lower if estimates are less than a meter for the northern 40 km. In scenario D, the entire Clark, Casa Loma, and Claremont faults rupture together, producing higher displacements than observed for the southern 55 km of the Clark fault. In this scenario it is inferred that slip was higher during the MRE for the majority of the Clark fault increasing the average slip to ~ 3.0 , assuming the maximum displacement is greater than in Anza Valley. Again, similar to scenario B, this is only a rough estimate since no offsets were recorded farther north than Anza making it possible for slip values to be higher than estimated.

MAGNITUDE CALCULATIONS

From the observed slip distribution, the minimum magnitude calculated for the MRE is about $M7.2$, using scenario E. Since 1899 four major earthquakes have had their epicenters located on or near the Clark fault (1899, 1918, 1937, and 1954), with two other pre-1898 earthquakes also tentatively placed along the San Jacinto fault (1890 and 1892). Herein, the argument is made to place a third pre-1898 earthquake on the Clark fault, the November 22nd, 1800 earthquake. Exactly which, if any, produced the offset geomorphology observed is un-resolved.

Of the four well documented post-1898 earthquakes, the 1899 and 1918 are located north of Anza, on the bounding faults of a 5 km wide releasing step-over near the towns of San Jacinto and Hemet. The exact magnitudes for each have generated much debate in the past due to the lack of seismic stations within close proximity to the epicenters. Far-field intensity maps have previously suggested that the earthquake of 1899 was larger than the 1918. However, surface-waves on Milne seismographs of the 1918 earthquake average three

times larger than the 1899 earthquake, corresponding to a M_s of half a unit higher (Ellsworth, 1990). Although potentially large enough to produce surface rupture, and both did produce “cracking” within the San Jacinto Valley, no primary surface rupture was located for either event (Claypole, 1900, Townley, 1918). From intensities recorded for both earthquakes, damage was less in Anza (MMI VI-VII) than near San Jacinto (MMI VIII-IX) (Figures 3a and b), also confirming that neither produced surface ruptures into the Anza gap (Sanders and Kanamori, 1984). Therefore it is concluded that neither event could have produced the slip I observe on the southern portion of the Clark fault.

The three pre-1898 earthquakes (1800, 1890 and 1892) are very poorly located due to the lack of observations throughout southern California. However, it is possible to estimate the magnitude of the earthquakes from these limited observations, but with very large uncertainties. The isoseismal maps generated for the 1890 and 1892 earthquakes show that intensity MMI V damage extended from San Diego to Yuma (Figures 36a and b). When the isoseismal maps of the 1890 and 1892 earthquakes are compared to those for the earthquakes of 1899 and 1918, the area of intensity V damage is considerably less for the pre-1898 earthquakes. From this, the 1890 and 1892 events are inferred to be smaller than the 1899 and 1918 earthquakes, consistent with being listed as $M6.3$ (Toppozada et al., 1981). Therefore, the 1890 and 1892 earthquakes were not large enough to have produced the amount of displacement observed on the southern Clark fault for the MRE, no matter where they were located.

The final possibility for a historic earthquake large enough to have produced the tectonic geomorphology observed along the Clark fault occurred on November 22, 1800. The location, as well as the size of the event, is very poorly understood due to the limited

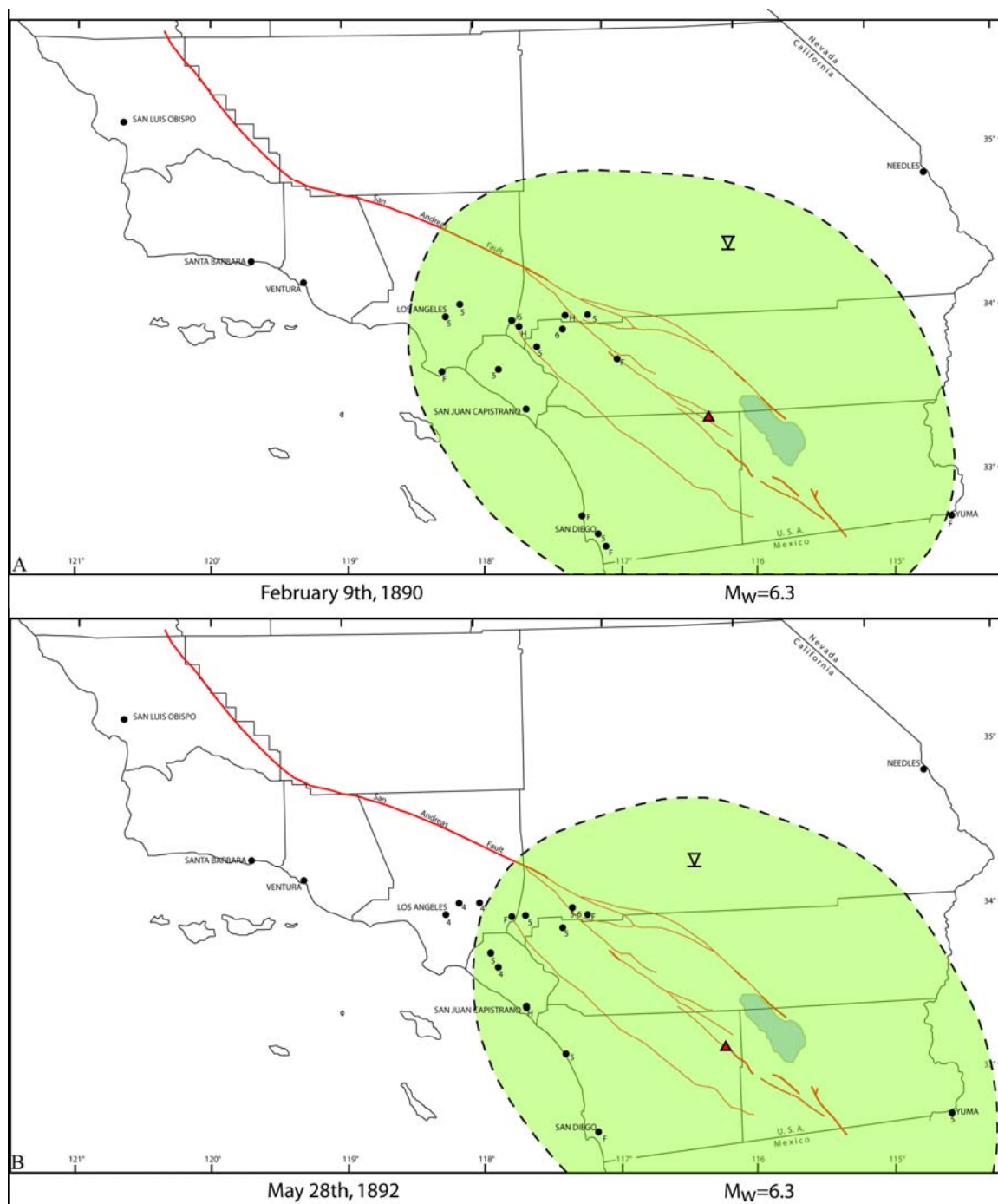


Figure 36. Isoseismal maps of (a) the earthquake of February 9th, 1890 and (b) the earthquake of May 28th, 1892. Both earthquakes are assessed to be $M_W=6.3$ or less. Modified from Topozada et al. (1981).

observations for this earthquake (only two, one from San Diego and another from San Juan Capistrano). These two reports indicate cracked adobe walls for both the San Diego and the San Juan Capistrano missions, which is commonly associated with MMI VII. With the two missions sustaining the same strong damage, while being more than 90 km apart requires that the associated earthquake be $M_{6.5}$ or greater (Topozada et al., 1981). The timing of this earthquake coincides fairly well with the estimated date of the last surface rupturing event at Hog Lake (ca. 1790) and possibly the offset geomorphology on the southern Clark fault.

To better estimate the magnitude for the 1800 earthquake, the relationships between the area enclosed by various MMI value contours and earthquake magnitude are used (Topozada, 1975). For the case at hand, I estimate the area of an ellipse relatively centered along the Clark fault near Anza with both the San Diego and San Juan Capistrano Mission's located on or near the fringe of the MMI VII contour (Figure 37a). From this, a magnitude of $\sim M_{7.8}$ is estimated, substantially higher than any of the calculated scenarios. This magnitude was estimated based on a few major assumptions that, when looked at in greater detail, can produce drastically different results.

First, the reported intensities from the missions are assumed to be correctly assigned a MMI VII for the cracked adobe walls. However, there is not much difference between Topozada's (1981) explanation of a MMI VI and VII for cracked walls. It is not unreasonable to assume that the construction quality of the adobe walls were poor compared to today's standards, resulting in less stability and more damage from earthquakes. If I assume a MMI VI-VI+ instead of MMI VII for the two missions, the resulting magnitude estimates would be $M_{VII}=7.5$ for the area inside the VII contour and about $M_{VI}=7.2$ for the VI contour, similar to the magnitudes assessed from the above rupture scenarios (Figure 37b).

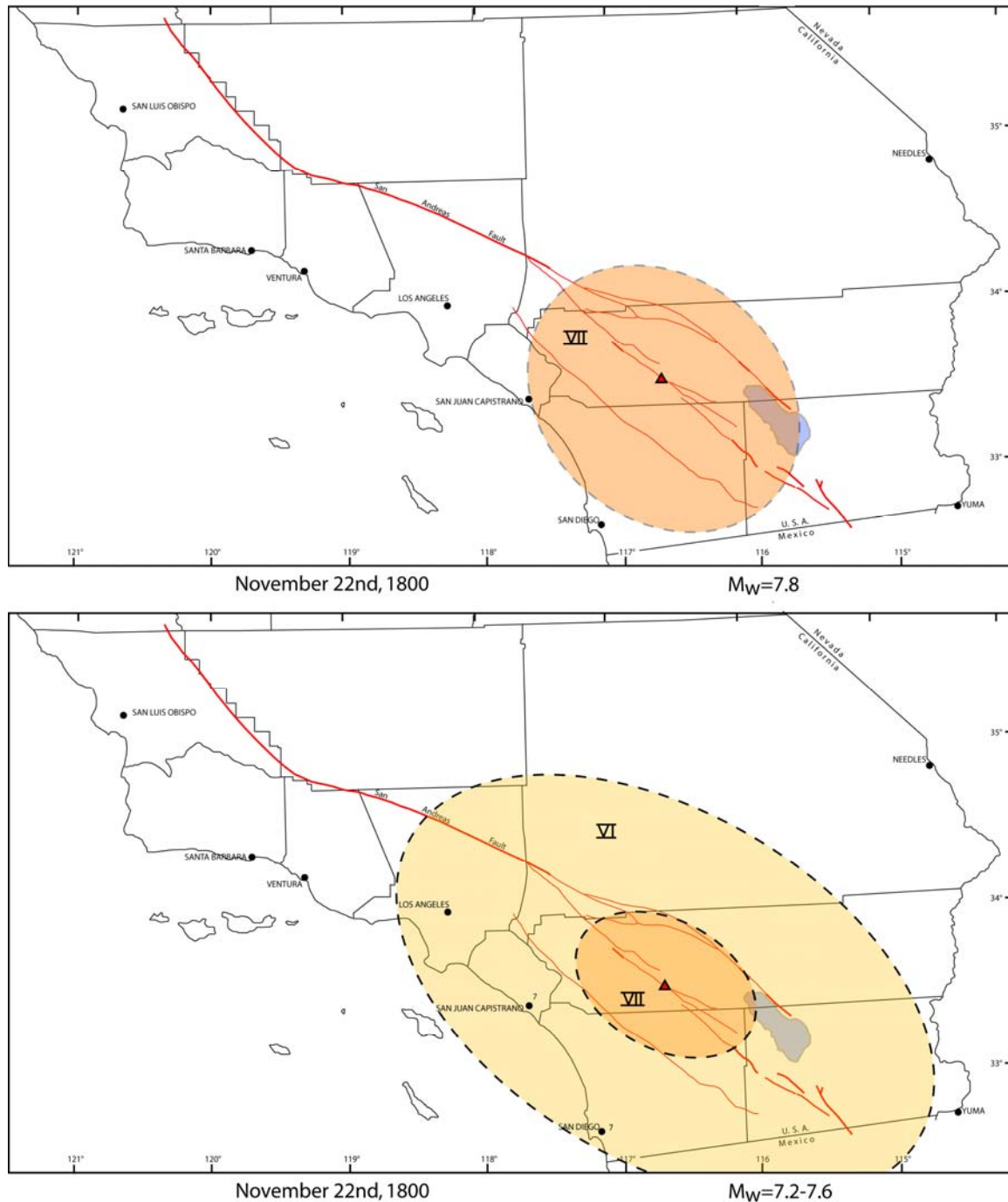


Figure 37. Isoseismal maps of the November 22nd, 1800 earthquake interpreted from two observations at San Diego and San Juan Capistrano missions. (a) First estimates suggest MMI VII damage at both missions. If the epicenter is placed on the Clark fault this would result in a $M_w=7.8$. (b) Reinterpreting the intensity damage for the missions I suggest a lesser MMI value for the missions. Placing them in the MMI VI range rather than VII I estimate $M_w=7.2$ to $M_w=7.6$, consistent with estimates assessed from the slip distribution.

Another assumption made was that the 1800 earthquake was located near Anza on the Clark fault. An alternate possibility is that the earthquake of 1800 is not actually on the Clark fault, but possibly on the Elsinore fault or even on one of the borderland faults offshore as previously inferred. However, the only segments of the Elsinore that have ruptured in the past 300 years, based on paleoseismic observations, are the Wildomar segment (Vaughan et al., 1999) and the Coyote Mountain segment (Rockwell et al., 1990). Rupture of either one of these could not account for both observations at San Diego and San Juan Capistrano, so unless one suggests that they ruptured together with a 100 km slip gap between, it is unlikely that the 1800 event occurred on the Elsinore fault.

The youthful appearance of the offsets observed in the field supports the idea that the MRE on the Clark fault is recent, within the last 250 years or so. However, I can conclude that beyond a reasonable doubt, none of the post-1890 earthquakes could have produced the offsets observed for the southern Clark fault. Alternatively, from this information it is suggested that the earthquake of November 22, 1800 was large enough to produce the observed offset surface geomorphology on the southern Clark fault.

SLIP RATE

From the new slip distribution data, a slip rate can estimate for the Clark fault when combined with recent paleoseismic work from Hog Lake. Taking the observation of 16 events at Hog Lake in the past 4 Ka, and assuming every event had a similar amount of slip near Anza as did the MRE, about 3.5 m, suggests a rate of about 14 mm/yr, very similar to the published rates suggested by Rockwell et al. (1990). If slip continues to increase to the northwest to Hog Lake and reaches about 4 m, the inferred rate increases to about 16 mm/yr.

However, among the Hog Lake events is a cluster of four events in the 13th and 14th centuries AD (Rockwell et al., 2006). If each event sustained similarly large displacement, then the short term rate in that period was very high. Alternatively, some of the dated events in this cluster may have sustained lower slip. If so, and the assumption that this cluster of events is to represent one “regular” Hog Lake event, then only 13 large events are inferred for the past 4 ka, eleven of which are in the past 3 ka. This yields a return period for the larger events of about 280 years, and a rate of 12.5-14 mm/yr, assuming 3.5-4 m of slip per such events.

I was also able to estimate a slip rate for the southern Clark fault from an offset alluvial fan that makes up Lute Ridge from its primary source drainage. The exact reconstruction of Lute Ridge is not well constrained, as any one of the three prominent drainages could be the source for the alluvial fan (Figure 33). Offsets range from 400 m up to 2000 m, although the largest offset is unlikely, but still not out of the question. The age of deposition for Lute Ridge is also poorly constrained, ranging from 100 ka to 200+ ka based on the presence of a stage IV calcic horizon in the soil profile (personal comm. Rockwell, 2006). Using the minimum amount of offset from the fan apex to its closest derivative source of 400 m, a slip rate to between 2 and 4 mm/yr is estimated (Table 8). The highest rate is calculated from the 2 km maximum offset to be 10-20 mm/yr, which is considered an extreme upper limit for the rate in this area.

Table 8. Estimated Slip Rate Based on Displaced Alluvial Fan Apex of Lute Ridge

Lute Ridge Slip Rates	Offset, m	Age, ka	Slip Rate, mm/yr
Reconstruction to drainage A	400	100	4
		200	2
Reconstruction to drainage B	980	100	9.8
		200	4.9
Reconstruction to drainage C	2000	100	20
		200	10

CHAPTER 5

CONCLUSION

Estimated offset geomorphic features along the southern 55 km of the Clark fault suggest that the most recent earthquake produced an average of 2.7 m of right-lateral slip. The estimates range from less than a meter near the mapped southern termination of the fault to close to 4 m in the north, near Anza. Double event offsets were also resolved for the same 55 km section, averaging ~4.9 m of right-lateral offset, indicating that the penultimate event was roughly 75 % the size of the MRE. Some degradation of the fault scarps produced from the last two events has likely occurred and may have decreased the observed displacement. Therefore, the estimated size of the penultimate event is presented as a minimum.

A number of rupture scenarios for the Clark fault are viable, ranging from rupture of the entire Clark, Casa Loma, and Claremont faults in a single M_w 7.5 earthquake (scenario C) down to an absolute minimum M_w 7.2 event rupturing only the southern 55 km section of the Clark fault (scenario E). As previous models have demonstrated that the propagation of an earthquake across the 5 km dilatational step-over at Hemet is doubtful, the most likely rupture scenario is a M_w 7.4 event that ruptures only the Clark and Casa Loma faults (scenario D). However, the lack of slip information for the northern Clark fault allows for any these scenarios to be possible and only future field work can truly resolve this issue.

Of the seven historic earthquakes tentatively placed on the Clark strand of the San Jacinto fault system, four are historically documented and did not produce any primary surface rupture (1899, 1918, 1937, and 1954). Therefore, it is inferred that the displacements

observed on the southern Clark were not caused by any of these four earthquakes. The pre-1898 earthquakes, 1800, 1890, and 1892, are poorly documented, with the magnitudes and locations calculated using minimal intensity observations. The area of intensity V damage estimated from the isoseismal maps for the earthquakes 1890 and 1892 is considerably less than for the earthquake of April 21st, 1918, suggesting a lower magnitude and confirming that neither the earthquake of 1890 or 1892 was large enough to produce the offset geomorphology observed for the southern 55 km of the Clark fault.

The location and magnitude of the November 22nd, 1800 earthquake is poorly known. Nevertheless, I believe it is conceivably large enough to have produced the average displacement documented for the southern Clark fault. Furthermore, the timing of this earthquake coincides with the most recent surface rupturing event recorded at Hog Lake (ca. 1790). From the limited intensity damage reports, a magnitude loosely estimated between $M_w=7.2$ and $M_w=7.5$, given that the epicenter was on the Clark fault. These estimates are similar to the magnitudes calculated from the slip distribution data for the southern Clark fault and the various scenarios of rupture behavior.

As no slip information was collected to the north of the Anza Valley, I can only assume the rupture behavior and therefore, present these magnitudes with some uncertainty. To fully resolve the timing, rupture length, and magnitude of the MRE, more detailed geomorphic and paleoseismic studies to the north of the Anza seismicity gap are required.

REFERENCES

- Abe, K., 1988, Magnitude and origin times from Milne seismograph data: Earthquakes in China and California, 1989-1912, *in* Lee, W.H.K. et al., eds., *Historical Seismograms and Earthquakes of the World*: Academic Press, San Diego, California, p. 37-50.
- Becker, T.W., Hardebeck, J.L., and Anderson, G., 2003, Constraints on fault slip rates of the Southern California plate boundary from GPS velocity and stress inversions: *Geophysical Journal International*, v. 160, no. 2, p. 634-650.
- Bennett, R.A., Friedrich, A.M., and Furlong, K.P., 2005, Codependent histories of the San Andreas and San Jacinto fault zone from inversion of fault displacement rates: *Geology*, v. 32, no. 11, 961-964.
- Bennett, R.A., Rodi, W., Reilinger, R.E., 1996, Global Positioning System constrains on fault slip rates in Southern California and northern Baja, Mexico: *Journal of Geophysical Research*, v. 101, p. 21943-21960.
- Brune, J.N., 1968, Seismic moment, seismicity, and rate of slip along major fault zones: *Journal of Geophysical Research*, v. 73, p. 777-784.
- Claypole, E.W., 1900, The earthquake at San Jacinto, December 25, 1899: *American Geologist*, v. 25, p. 106-108.
- DeMets, C., 1995, Reappraisal of seafloor spreading lineations in the Gulf of California: Implications for the transfer of Baja California to the Pacific plate and estimates of Pacific-North American motion: *Geophysical Research Letters*, v. 22, p. 3545-3548.
- Dorsey, R.J., 2002, Stratigraphic record of Pleistocene initiation and slip on the Coyote Creek fault, lower Coyote Creek, southern California, *in* Barth, A., ed., *Contributions to crustal evolution of the southwestern United States*: Geological Society of America Special Paper 365, Boulder, Colorado, Geological Society of America, p. 251-269.
- Doser, D.I., 1990, Source Characteristics of earthquakes along the southern San Jacinto and Imperial fault zones (1937 to 1954): *Bulletin of the Seismological Society of America*, v. 80, no. 5, 1099-1117.
- Doser, D.I., 1992, Historic earthquakes (1918 to 1923) and an assessment of source parameters along the San Jacinto fault system: *Bulletin of the Seismological Society of America*, v. 70, p. 185-201.

- Ellsworth, W.L., 1990, Earthquake history, 1769-1989, *in* Wallace, R.E., ed. The San Andreas Fault System, California: U.S. Geological Survey Professional Paper, 1515, p. 153-187.
- Fialko, Y., 2006, Interseismic strain accumulation and the earthquake potential on the southern San Andreas fault system: *Nature*, v. 441, no. 7096, p. 968-971.
- Hanks, T.C., and Kanamori, H., 1979, A moment-magnitude scale: *Journal of Geophysical Research*, v. 84, p. 2348-2350.
- Hanks, T.C., Hileman, J.A., and Thatcher, W., 1975, Seismic moments of the larger earthquakes of the Southern California region: *Geological Society of America Bulletin*, v. 86, p. 1131-1139.
- Harris, R., and Day, S., 1993, Dynamics of fault interaction: Parallel strike-slip faults: *Journal of Geophysical Research*, v. 98, p. 4461-4472.
- Hudnut, K., Seeber, L., Rockwell, T., Goodmacher, J., Klinger, R., Lindvall, S., and McElwain, R., 1989, Surface ruptures on cross-faults in the 24 November 1987 Superstition Hills, California, earthquake sequence: *Bulletin of the Seismological Society of America*, v. 79, p. 304-329.
- Janecke, S.U., Kirby, S.M., Langenhiem, V.E., Housen, B.A., Dorsey, R.J., Crippen, R.E., and Blom, R.G., 2004, Kinematic and evolution of the San Jacinto fault zone in the Salton Trough: progress report from the San Felipe Hills area: *Geological Society of America Abstracts and Programs*, v. 36, no. 5, p. 317.
- Kendrick, K.J., Morton, D.M., Wells, S.G., and Simpson, R. W., 2002, Spatial and temporal deformation along the northern San Jacinto fault, Southern California: Implications for slip rates: *Bulletin of the Seismological Society of America*, v. 92, no. 7, p. 2782-2802.
- Kondo, H., Awata, Y., Emre, O., Doğan, A., Özalp, S., Tokay, F., Yildirim, C., Yoshioka, T., Okumura, K., 2005, Slip distribution, fault geometry and fault segmentation of the 1944 Bolu-Gerede earthquake rupture, North Anatolian fault, Turkey: *Bulletin of the Seismological Society of America*, v. 95, no. 4, p. 1234-1249.
- Lindvall, S.C., Rockwell, T.K., and Hudnut, K.W., 1989, Evidence for prehistoric earthquakes on the Superstition Hills fault from offset geomorphic features: *Bulletin of the Seismological Society of America*, v. 79, no. 2, p. 342-361.
- Magistrale, H., 2002, The relation of the southern San Jacinto fault zone to the Imperial and Cerro Prieto faults, *in* Barth, A., ed., Contributions to crustal evolution of the southwestern United States: *Geological Society of America Special Paper 365*, Boulder, Colorado, Geological Society of America, p. 271-278.

- Matti, J.C., Morton, D.M., and Cox, B.F., 1992, The San Andreas fault system in the vicinity of the central Transverse Ranges province, Southern California: U.S. Geological Survey Open-File Report OF 92-0354.
- Merifield, P.M., Rockwell, T.K., and Loughman, C.C., 1991, A slip rate based on trenching studies, San Jacinto fault zone near Anza, California: *in* McCalpin, J. P., ed., Engineering Geology and Geotechnical Engineering, p. 1-12.
- McGill, S.F., and Rubin, C.M., 1999, Surficial slip distribution on the central Emerson fault during the June 28, 1992, Landers earthquake, California: *Journal of Geophysical Research*, v. 104, no. B3, p. 4811-4833.
- McGill, S.F., and Sieh, K., 1991, Surficial offsets on the central and eastern Garlock fault associated with prehistoric earthquakes: *Journal of Geophysical Research*, v. 96, no. B13, p. 21,597-21,621.
- Morton, D.M., and Matti, J.C., 1993, Extension and contraction within an evolving divergent strike-slip fault complex: The San Andreas and San Jacinto fault zones at their convergence in Southern California: *in* Powell, R.E. et al., eds., The San Andreas fault system: Displacement, palinspastic reconstruction, and geologic evolution: Boulder, Colorado, Geological Society of America Memoir 178, p. 217-230.
- Park, S.K., Pendergraft, D., Stephenson, W.J., Shedlock, K.M., and Lee, T.C., 1995, Delineation of intrabasin structure in a dilatational jog of the San Jacinto fault zone, Southern California: *Journal of Geophysical Research*, v. 100, p. 691-702.
- Powell, R.E., 1993, Balanced palinspastic reconstruction of pre-late Cenozoic paleogeology, Southern California: Geologic and kinematic constrains on evolution of the San Andreas fault system: *in* Powell, R.E. et al., eds., The San Andreas fault system: Displacement, palinspastic reconstruction, and geologic evolution: Boulder, Colorado, Geological Society of America Memoir 178, p. 1-106.
- Rasmussen, G.S., 1981, Nature of surface rupture and recurrence interval, Casa Loma fault: *in* *Geology of the San Jacinto Mountains*, South Coast Geological Society Annual Field Trip Guidebook 9: South Coast Geological Society, Santa Ana, California, p. 48-54.
- Rasmussen, G.S., 1982, Historic earthquakes along the San Jacinto fault zone, San Jacinto, California: *in* Cooper, J.D., ed., Neotectonics in Southern California, Geological Society of America Cordilleran Section Meeting. Fieldtrip Guidebook, 78th Annual Meeting: Boulder, Colorado, Geological Society of America, p. 115-121.
- Rockwell, T.K., 1990, Holocene activity of the Elsinore fault in the Coyote Mountains, Southern California: *in* F.O.P. Guidebook and Volume on Western Salton Trough-Soils and Neotectonics: p. 30-42.

- Rockwell, T.K., and Pinault, C.T., 1986, Holocene slip events on the southern Elsinore fault, Coyote Mountains, Southern California: *in* Ehlig, P., ed., Guidebook and Volume on Neotectonics and Faulting in Southern California, Cordilleran Section, Geological Society of America, p. 193-196.
- Rockwell, T.K., Loughman, C., Merifield, P., 1990, Late Quaternary rate of slip along the San Jacinto fault zone near Anza, Southern California: *Journal of Geophysical Research*, v. 95, no. B6, p. 8593-8605.
- Rockwell, T.K., Lindvall, S.C., Dawson, T.E., Langridge, R.M., Lettis, W.R., and Klinger, Y., 2002, Lateral offsets on surveyed cultural features resulting from the 1999 Izmit and Duzce earthquakes, Turkey: *Bulletin of the Seismological Society of America*, v. 92, no. 1, p. 79-94.
- Rockwell, T.K., Seitz, G., Dawson, T., Young, J., 2006, The long record of San Jacinto fault paleoearthquakes at Hog Lake: Implications for regional patterns of strain release in the southern San Andreas fault system: *Seismological Research Letters*, v. 77, no. 2, p. 270.
- Rolfe, F., and Strong A.M., 1918, The earthquake of April 21, 1918, in the San Jacinto Mountains: *Bulletin of the Seismological Society of America*, v. 8, p. 63-67.
- Sanders, C.O., 1989, Fault segmentation and earthquake occurrence in the strike-slip San Jacinto fault zone, California: *in* Schwartz, D.P. and Sibson, R.H., eds., Proceedings of Conference XLV, Workshop on fault segmentation and controls of rupture initiation and termination: U.S. Geological Survey Open-File Report, OF 89-0315, p. 324-349.
- Sanders, C.O., and Kanamori, H., 1984, A seismotectonic analysis of the Anza Seismic Gap, San Jacinto fault zone, Southern California: *Journal of Geophysical Research*, v. 89, no. B7, p. 5873-5890.
- Sanders, C., Magistrale, H., 1997, Segmentation of the northern San Jacinto fault zone, Southern California: *Journal of Geophysical Research*, v. 102, no. B12, p. 27,453-27,467.
- Sanders, C.O., Magistrale, H., and Kanamori, H., 1986, Rupture patterns and preshocks of large earthquakes in the southern San Jacinto fault zone: *Bulletin of the Seismological Society of America*, v. 76, no. 5, p. 1187-1206.
- Savage, J.C., and Prescott, W.H., 1976, Strain accumulation on the San Jacinto fault near Riverside, California: *Bulletin of the Seismological Society of America*, v. 66, no. 5, p. 1749-1754.
- Savage, J.C., Prescott, W.H., Lisowski, M., and King, N.E., 1981, Strain accumulation in Southern California, 1973-1980: *Journal of Geophysical Research*, v. 86, no. B8, p. 6991-7001.

- Sharp, R.V., 1967, San Jacinto fault zone in the Peninsular Ranges of Southern California: Geological Society of America Bulletin, v. 78, p. 705-730.
- Sharp, R.V., 1972, Map showing recently active breaks along the San Jacinto fault zone between the San Bernardino area and Borrego Valley, California: scale 1:24,000, U.S. Geological Survey Miscellaneous Geologic Investigations Map, I-675.
- Sharp, R.V., 1981, Variable rates of Late Quaternary strike slip on the San Jacinto fault zone, Southern California: Journal of Geophysical Research, v. 86, no. B3, p. 1754-1762.
- Sharp, R.V., Budding, K.E., Boatwright J., Ader, M.J., Ader, M.G., Bonilla, M.G., Clark, M.M., Fumal, T.E., Harms, K.K., Lienkaemper, J.J., Horton, D.M., O'Neill, B.J., Ostergren, C.L., Ponti, D.J., Rymer, M.J., Saxton, J.L., Sims, J.D., 1989, Surface faulting along the Superstition Hills fault zone and nearby faults associated with the earthquakes of 24 November 1987: Bulletin of the Seismological Society of America, v. 79, p. 252-281.
- Sibson, R.H., 1984, Roughness at the base of the seismogenic zone: Contributing factors, Journal of Geophysical Research, v. 89, p. 5791-5799.
- Sieh, K.E., 1978, Slip along the San Andreas fault associated with the great 1857 earthquake: Bulletin of the Seismological Society of America, v. 68, no. 5, p. 1421-1448.
- Sieh, K., 1996, The repetition of large-earthquake ruptures: Proceedings of the National Academy of Sciences of the United States of America, v. 93, p. 3764-3771.
- Thatcher, W., Hileman, J.A., and Hanks, T.C., 1975, Seismic slip distribution along the San Jacinto fault zone, Southern California, and its implications: Geological Society of America Bulletin, v. 86, p. 1140-1146.
- Topozada, T.R., 1975, Earthquake magnitude as a function of intensity data in California and western Nevada: Bulletin of the Seismological Society of America, v. 65, no. 5, p. 1222-1238.
- Topozada, T.R., Real, C.B., and Parke, D.L., 1981, Preparation of isoseismal maps and summaries of reported effects for pre-1900 California earthquakes: Open File Report 81-11 SAC, California Division of Mines and Geology, Sacramento.
- Townley, S.D., 1918, The San Jacinto earthquake of 1918: Bulletin of the Seismological Society of America, v. 8, p. 45-63.
- Treiman, J.A., Kendrick, K.A., Bryant, W.A., Rockwell, T.K., and McGill, S.F., 2002, Primary surface rupture associated with the Mw7.1 16 October, 1999 Hector Mine earthquake, San Bernardino County, California: Bulletin of the Seismological Society of America, v. 92, no. 4, p. 1171-1191.

Vaughan, P.R., Thorup, K.M., Rockwell, T.K., 1999, Paleoseismology of the Elsinore Fault at Agua Tibia Mountain, Southern California: *Bulletin of the Seismological Society of America*, v. 89, no. 6, p.1447-1457.